GULF RADIATION TECHNOLOGY

Gulf-RT-A12210

MEASUREMENTS OF THE $^{10}B(n,\alpha_1\gamma)$ AND $^{10}B(n,\alpha)$ CROSS SECTIONS

FINAL REPORT

Work done by:

S. J. Friesenhahn
A. D. Carlson
V. J. Orphan
M. P. Fricke

NOTICE

This report was prepared as an account of work sponsored by the United States Government. Neither the United States nor the United States Atomic Energy Commission, nor any of their employees, nor any of their contractors, subcontractors, or their employees, makes any warranty, express or implied, or assumes any legal liability or responsibility for the accuracy, completeness or usefulness of any information, apparatus, product or process disclosed, or represents that its use would not infringe privately owned rights.

Report written by:

S. J. Friesenhahn
A. D. Carlson
V. J. Orphan
M. P. Fricke

Date Published - October 16, 1972

PREPARED FOR THE U.S. ATOMIC ENERGY COMMISSION
DIVISION OF REACTOR DEVELOPMENT AND TECHNOLOGY
UNDER CONTRACT NO. AT(04-3)-167
PROJECT AGREEMENT NO. 45

Gulf Radiation Technology Project 4027

GULF RADIATION TECHNOLOGY
A DIVISION OF GULF ENERGY & ENVIRONMENTAL SYSTEMS COMPANY
P.O. BOX 608, SAN DIEGO, CALIFORNIA 92112

MASTER

DISTRIBUTION OF THIS DOCUMENT IS UNLIMITED

GG

DISCLAIMER

This report was prepared as an account of work sponsored by an agency of the United States Government. Neither the United States Government nor any agency thereof, nor any of their employees, makes any warranty, express or implied, or assumes any legal liability or responsibility for the accuracy, completeness, or usefulness of any information, apparatus, product, or process disclosed, or represents that its use would not infringe privately owned rights. Reference herein to any specific commercial product, process, or service by trade name, trademark, manufacturer, or otherwise does not necessarily constitute or imply its endorsement, recommendation, or favoring by the United States Government or any agency thereof. The views and opinions of authors expressed herein do not necessarily state or reflect those of the United States Government or any agency thereof.

DISCLAIMER

Portions of this document may be illegible in electronic image products. Images are produced from the best available original document.

CONTENTS

This page left blank intentionally.

ILLUSTRATIONS

ILLUSTRATIONS (Continued)

ILLUSTRATIONS (Continued)

This page left blank intentionally.

LIST OF TABLES

This page left blank intentionally.

1. INTRODUCTION

This report describes measurements of the $^{10}B(n,\alpha)$ and $^{10}B(n,\alpha_1\gamma)$ cross sections relative to the hydrogen scattering cross section. The $^{10}B(n,\alpha)$ cross section was determined from 4- to 750-keV neutron energy, with an overall systematic uncertainty of ∿2 to 3% over most of the energy region. The $^{10}B(n,\alpha_1\gamma)$ cross section was determined from 4 to 1000 keV with an overall systematic uncertainty of ∿1 to 2% at most energies. Using fine neutron energy groups of $\Delta E/E = 5\%$, the total statistical uncertainties in both cross sections are ∿2 to 3% at all energies. Extension of the present results for both cross sections to energies below 4 keV and a confirmation of the present $^{10}B(n,\alpha)$ results above 100 keV will be made in the course of the continuing standard cross-section program at Gulf Rad Tech.

The energetically allowed interactions between the ^{10}B nucleus and neutrons of <1-MeV energy include the following:

$$^{10}B(n,n)^{10}B$$
$$^{10}B(n,t)^{8}Be + 0.230\ MeV$$
$$^{10}B(n,\gamma)^{11}B + 11.456\ MeV$$
$$^{10}B(n,p)^{10}Be + 0.227\ MeV$$
$$^{10}B(n,2\alpha)T + 0.328\ MeV$$
$$^{10}B(n,\alpha_0)^{7}Li + 2.79\ MeV$$
$$^{10}B(n,\alpha_1)^{7}Li^{*} + 2.31\ MeV \quad .$$

In the last reaction, the $^{7}Li^{*}$ nucleus decays promptly to the ground state by emission of a 478-keV gamma ray. With the exception of elastic scattering, the last two reactions constitute the major portion of the total cross section in this energy region. In the present work, the experimental techniques eliminate contributions to the observed events from all but the last two reactions. The protons, tritons, and the alphas from the $^{10}B(n,2\alpha)T$ reaction are eliminated by the thresholds imposed on the pulse-height

distributions. Capture gamma rays are eliminated in the Ge(Li) measurements via energy discrimination; they are unimportant in the proportional counter measurements due to the counter's low gamma-ray detection efficiency and low value of the capture cross section. Elastic scattering effects are treated explicitly in the data analysis. Contributions from neutron-induced reactions in ^{11}B, which is present with an abundance of ∿5% in the detector materials, are eliminated in similar ways.

The $^{10}B(n,\alpha_1\gamma)$ and $^{10}B(n,\alpha)$ reactions are frequently used to determine neutron fluxes because their cross sections are large, have a relatively smooth energy dependence, and are simple to implement with standard neutron detectors. In spite of their importance in the energy region above 1 keV, very few measurements of these cross sections have been made recently in this region.

In the older measurements, several different techniques have been employed to determine these cross sections. Mooring[1] and Diment[2] have determined the ^{10}B absorption cross section up to ∿500 keV from the difference between the total and scattering cross sections. For the energy region below 1 MeV the absorption cross section is almost identical to the (n,α) cross section. Cox[3] has also obtained the absorption cross section from an analysis of spherical shell transmission measurements for neutron energies up to 250 keV. Macklin and Gibbons[4] determined the (n,α_0) cross section from measurements of the $^{7}Li(\alpha,n)^{10}B$ cross section using reciprocity. The $(n,\alpha_1\gamma)$ cross section was then deduced from branching ratio measurements. These measurements extend to ∿500 keV.

Sowerby[5] has obtained the $^{10}B(n,\alpha)$ cross section up to 80 keV from measurements of the ratio of $^{6}Li(n,\alpha)$ to $^{10}B(n,\alpha)$ cross sections combined with determinations of the $^{6}Li(n,\alpha)$ cross section. BF_3 counters, combined with long counters for flux measurements, have been employed by Davis,[6] Bichsel[7] and Bogart[8] to determine the (n,α) cross section. Davis resolved the two alpha groups, and consequently he also obtained the $(n,\alpha_1\gamma)$ cross section. From NaI measurements of the 478-keV gamma ray from the $(n,\alpha_1\gamma)$ reaction, Nellis[9] has obtained the $(n,\alpha_1\gamma)$ cross section up to ∿5 MeV.

These older measurements each have weaknesses which were considered in the design of the new experiment reported here. The difference between the total and scattering cross sections at high neutron energies is difficult to determine because the scattering cross section is large and not well known. Spherical shell transmission measurements are complicated by the need for very accurate transmission data as well as a very elaborate analysis. Measurements based on reciprocity combined with branching ratio data must consider the possibility of undetermined structure in the branching ratio. Determinations based on $^{6}Li(n,\alpha)$ to $^{10}B(n,\alpha)$ cross-section ratios are presently hampered by uncertainties in the $^{6}Li(n,\alpha)$ cross section. Measurements involving long counters for flux determination may have uncertainties due to the long counter efficiency uncertainty. Measurements of the $(n,\alpha_1\gamma)$ cross section using NaI detectors may have background problems due to gamma rays that cannot be resolved with these detectors.

At the 1970 EANDC Conference on Neutron Standards and Flux Normalization, it was concluded that new direct measurements of the $^{10}B(n,\alpha)$ and $^{10}B(n,\alpha_1\gamma)$ cross sections were needed, particularly for neutron energies above 100 keV. It was also concluded that these measurements should be made relative to the hydrogen scattering cross section and that the measurements should also be continuous in neutron energy from low energies, where the cross section is well known, to $\sim$1 MeV where the hydrogen scattering cross section can be easily implemented as a neutron flux monitor.

The present measurements were undertaken in order to satisfy all these requirements. The data were obtained with neutrons from an electron Linac target by employing time-of-flight techniques. Hydrogen and methane gas proportional counters were used to determine the neutron flux from $\approx$1 keV to 1 MeV. In order to allow consistency checks to be made, the $^{10}B(n,\alpha)$ cross section was measured with both BF_3 gas proportional counters and with a parallel plate ionization chamber containing ^{10}B-loaded self supporting films. The $^{10}B(n,\alpha_1\gamma)$ cross section was measured with a lithium-drifted germanium gamma-ray spectrometer.

The present measurements of the $^{10}B(n,\alpha)$ cross section below 60 keV agree with the more recent data and, when they are combined with the older

measurements, reduce the uncertainties in the cross section in this energy region. Above 60 keV, the present $^{10}B(n,\alpha)$ cross-section measurements are in best agreement with the recent measurements of Bogart,[8] and they deviate significantly from the ENDF/B Version III evaluation. The most pronounced difference occurs at $\approx$450 keV where the present measurements indicate that the magnitude of the structure in the $^{10}B(n,\alpha)$ cross section is larger than has been previously observed.

The present $^{10}B(n,\alpha_1\gamma)$ data are in good agreement with the preliminary measurements of Coates[10] from 10 keV to greater than 100 keV. At higher neutron energies the present data generally fall between the measurements of Nellis[9] and those of Macklin.[4]

2. NEUTRON SOURCE AND FLIGHT PATH

The target and moderator assembly shown in Fig. 1 was designed to produce a neutron spectrum free of undesirable structure and a minimum of neutron slowing-down-time uncertainty. The electron beam strikes a water-cooled steel target at the center of a six-inch-diameter cylinder of depleted uranium. Bremsstrahlung is produced as the electrons slow down, and neutrons are produced by gamma-ray reactions with the target materials. The uranium serves to strongly attenuate the bremsstrahlung burst and to provide some neutron energy moderation via inelastic scattering. Additional moderation takes place in the 1-inch-thick polyethylene material. The polyethylene thus smooths out any structure in the neutron spectrum introduced by the uranium.

The dispersion in the slowing-down time to a given neutron energy is a function of the integrated macroscopic scattering cross section and the neutron velocity. This dispersion can be expressed in terms of an equivalent flight-path length uncertainty. At low neutron energies, where polyethylene moderation predominates, this equivalent distance uncertainty is 0.013 meters; and at very high energy, where polyethylene moderation is less appreciable, this distance uncertainty is still only 9.095 meters (neglecting moderating effects of the uranium and polyethylene).

After emerging from the polyethylene moderator, the neutrons pass through a 0.007-inch Mylar window and enter a 12-inch-diameter flight tube which is collimated to 11 inches approximately 10 meters from the source. The beam then passes through a pair of windows with a 12-inch air gap at the 45-meter flight-path station where the mechanism used to insert aluminum and polyethylene filters is located. The beam then enters a 24-inch-diameter flight tube which terminates with a 0.012-inch Mylar window. Both flight tubes were maintained at a pressure of <100 microns Hg throughout the experiment.

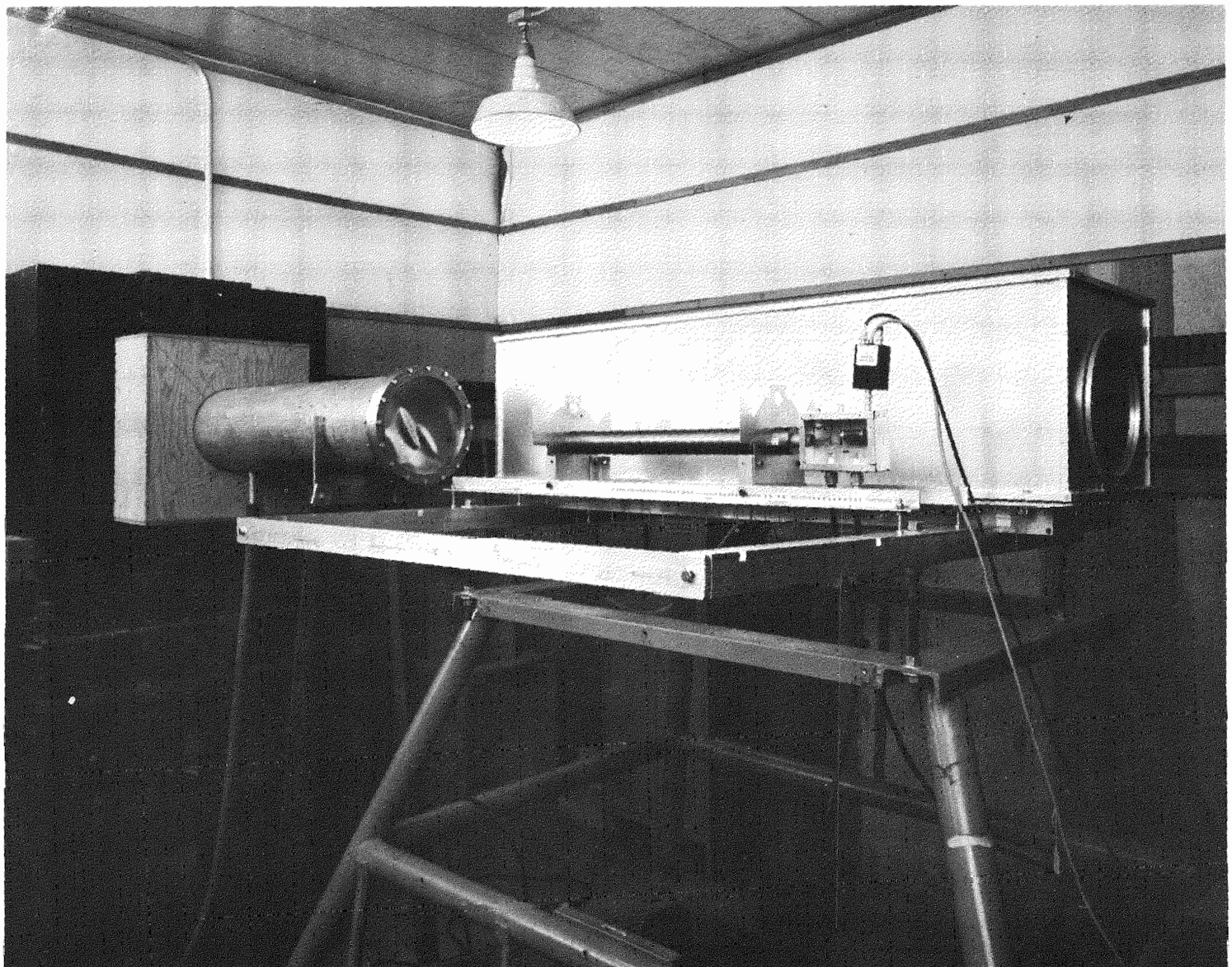

X-90152

Fig. 2. Background ion chamber and proportional counter in position on rolling table.

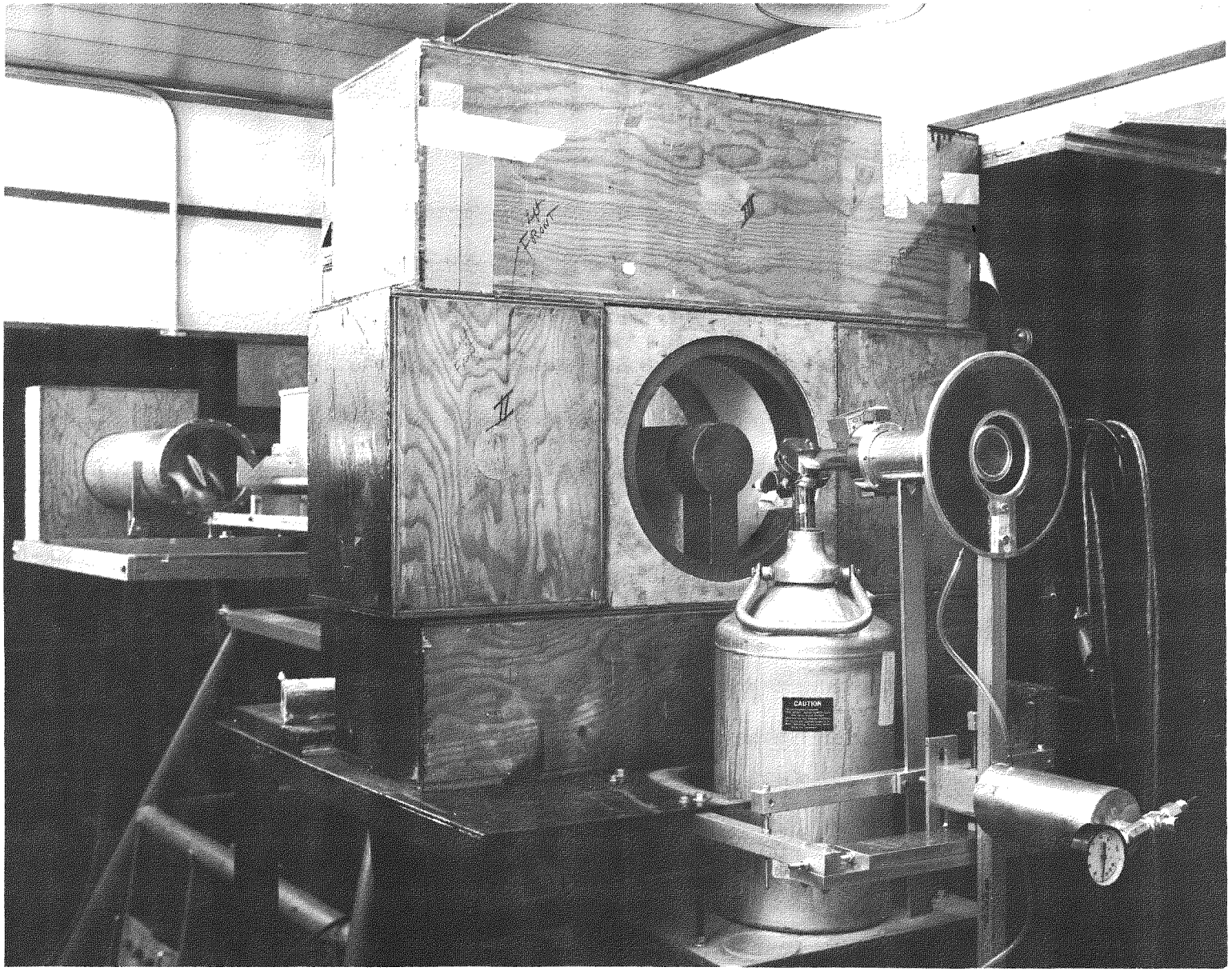

X-90153

Fig. 3. Ge(Li) detector in position near ^{10}B sample.

the beam center line just upstream from an assembly which allowed either a 0.0198 nuclei/barn ^{10}B sample or a 0.0182 nuclei/barn graphite sample to be placed in position. Both of these samples were constructed in the same manner as the ^{10}B filter just described.

The Ge(Li) detector was shielded from the beam by a 5-inch-diameter cylinder supported on a 2-inch wide support. Both shield elements consisted of lead and lithium carbonate. After passing the Ge(Li) detector, the beam enters a large cavity shielded with four inches of lead and 12 inches of boric acid.

The flight-path length has been measured to a precision of 0.04 meters using a geodimeter.

3. DATA ACQUISITION SYSTEM

3.1 EQUIPMENT

The major portion of the data was acquired with a CDC 1700 computer having 20,000 words of core memory and a 1.5-million-word removable disk. The computer was also equipped with a magnetic tape unit to which the data were transferred for subsequent analysis on a Univac 1108 computer. The electronic configuration employed at the computer interface for all types of data accumulation is shown in Fig. 4.

A simplified illustration of the time sequence for each accelerator burst is shown in Fig. 5. The sequence was initiated by a signal from the accelerator indicating that the klystrons had been triggered and the accelerator was ready to be pulsed. This READY pulse started a Rutherford three-channel crystal-controlled delay generator. This delay generator provides three independent delayed pulses which can be set in increments of 0.1 μsec. The first pulse output started the Eldorado crystal-controlled time-interval digitizer which was operated with a 0.08-μsec channel width for all of the measurements. The timing signals were passed through an on-gate which was turned on by the first output pulse. The time signals were delayed in 50-μsec passive delay lines and then passed through a specially constructed unit which introduced a fixed, well-defined deadtime that was insensitive to counting rate. This deadtime was set to be larger than the longest deadtime in the computer, and for the present work a deadtime of 162.5 μsec was used. The output of the deadtime unit provided the stop pulses for the time-interval digitizer.

The second output from the Rutherford delay generator was set at ≈150 μsec and used to pulse the Linac. Thus, about 100 μsec of data were accumulated before the Linac pulse. The Linac electron beam produces an intense burst of gamma rays which are detected by a photomultiplier located near the

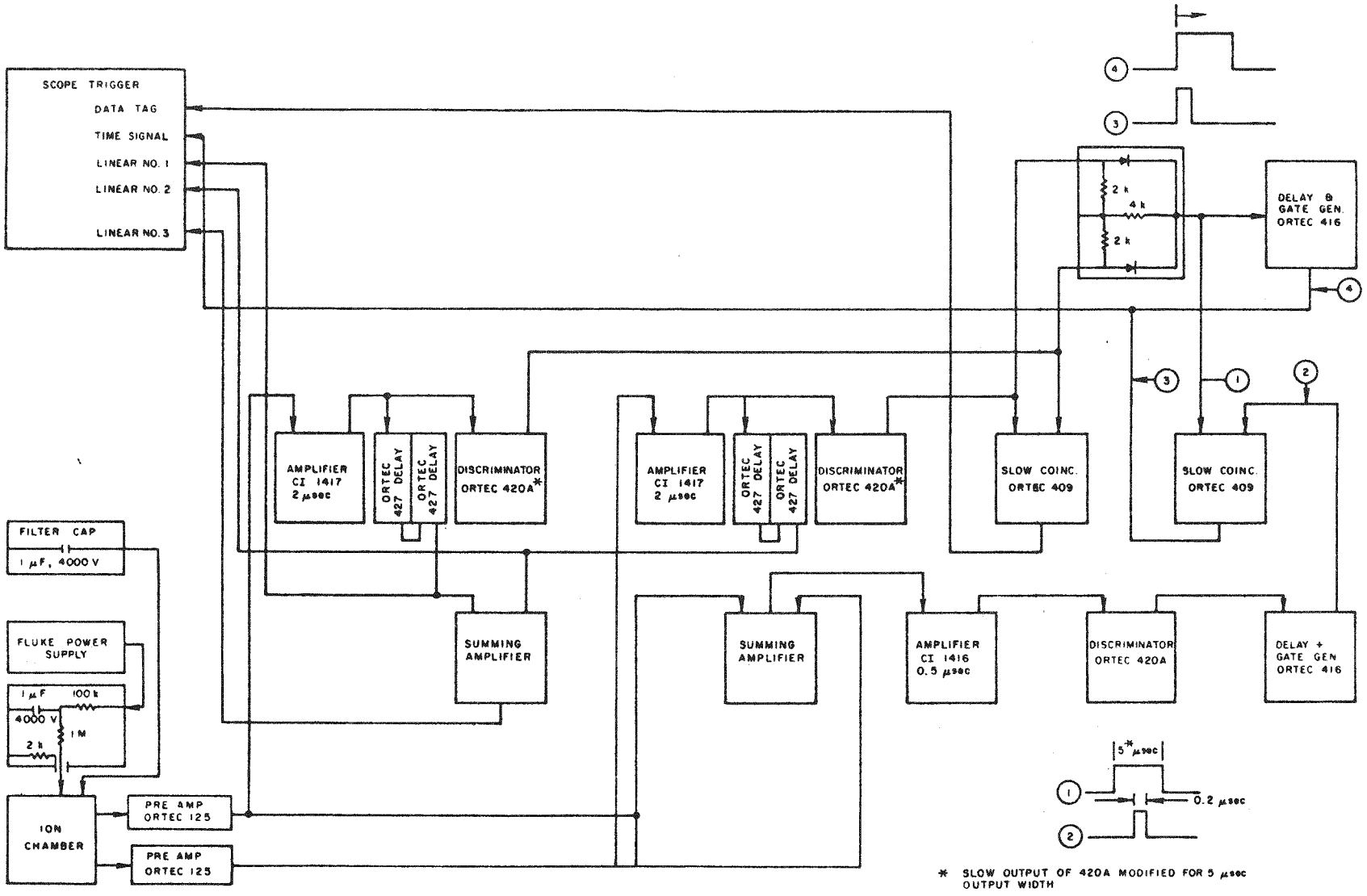

Fig. 4. Data acquisition system interface.

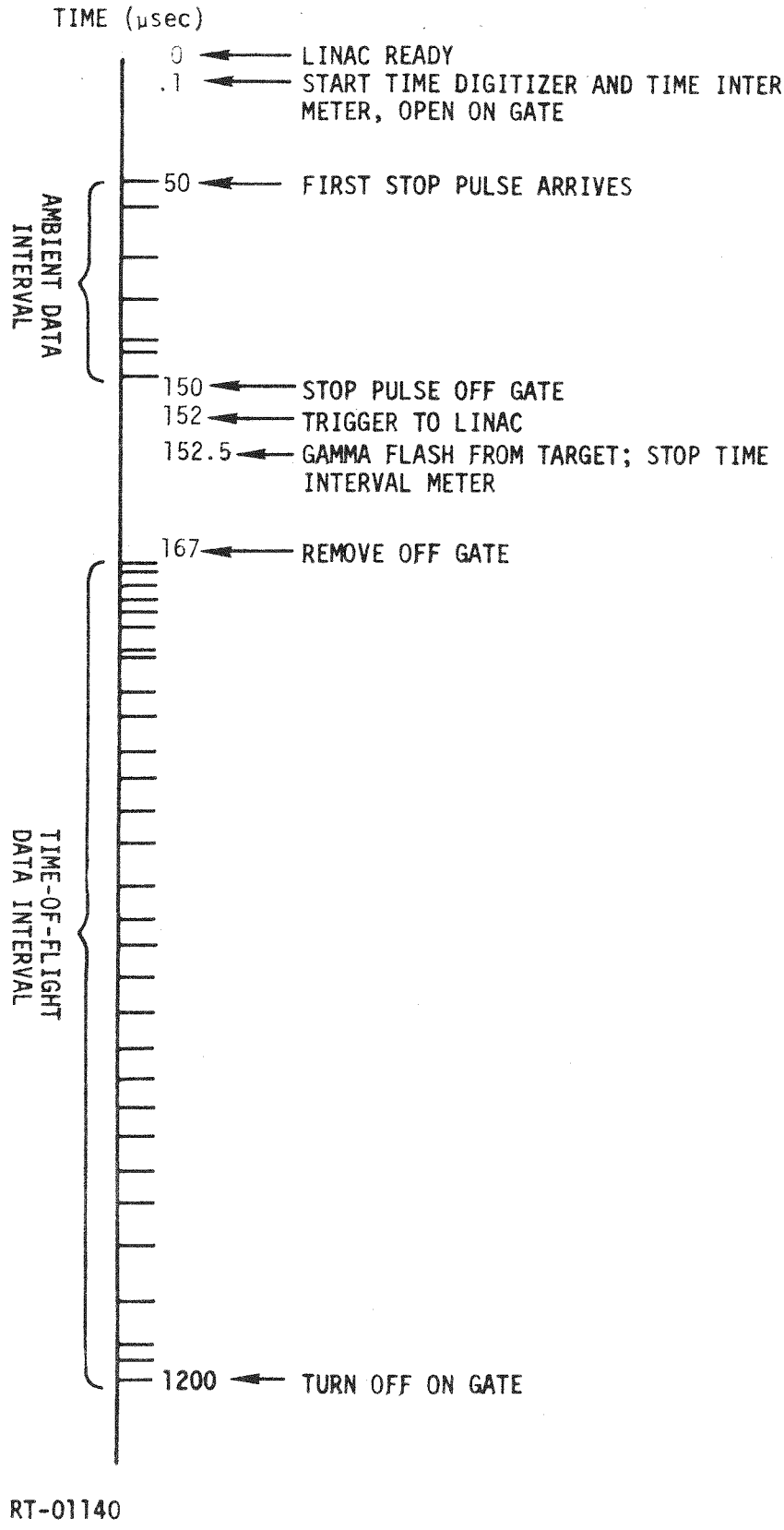

Fig. 5. Time sequence for recording the multiparameter data of each accelerator burst.

Linac target. The anode signal from this photomultiplier was used as a stop pulse for a time-interval meter with a resolving time of 0.01 μsec. The start pulse for this time-interval meter was the same pulse that started the time digitizer. The time-interval meter was monitored by the accelerator operator to prevent any time drifts between the two signals.

Since the counting rate is very high immediately after the accelerator burst, the time signals are gated off for ≈15 μsec to avoid excessive deadtime. The time-of-flight data were then accumulated for ≈1000 μsec before the on-gate was turned off.

Scalers were used to count the pulses into and out of the deadtime unit, as well as the reply pulses from the computer interface which signaled storage of an event. The accuracy of the deadtime corrections, which may be as large as 30% in some cases, was checked subsequently by comparing the deadtime-corrected number of events with the number of events into the deadtime unit as described in the data analysis section.

In order to detect any time-of-flight dependent gain shifts in the electronic system due to the effects of the accelerator-associated gamma flash, a gain shift determination was made for each detector configuration. This was accomplished by superimposing a fixed amplitude test pulse on the detector signal at the input of the preamplifier. The test pulse was not time correlated with the pulsing of the Linac, and hence provided a continuous sampling of the system gain for all flight times. The gain shifts determined in this fashion were insignificant for all the detectors, with the exception of the ion chamber data where a small correction for this effect was applied.

The overall linearity of the electronic system was measured at 10-15 points distributed across the usable pulse-height range of the system with a precision mercury pulser connected at the test input to the preamplifier. The pulser has a nominal linearity of 0.1% which exceeds the linearity of the overall electronic system by an order of magnitude.

The detailed block diagrams of the electronic configuration for the ion chamber data and the BF_3 data are shown in Figs. 6 and 7, respectively. The rationale for each configuration is discussed in the sections dealing with each type of data.

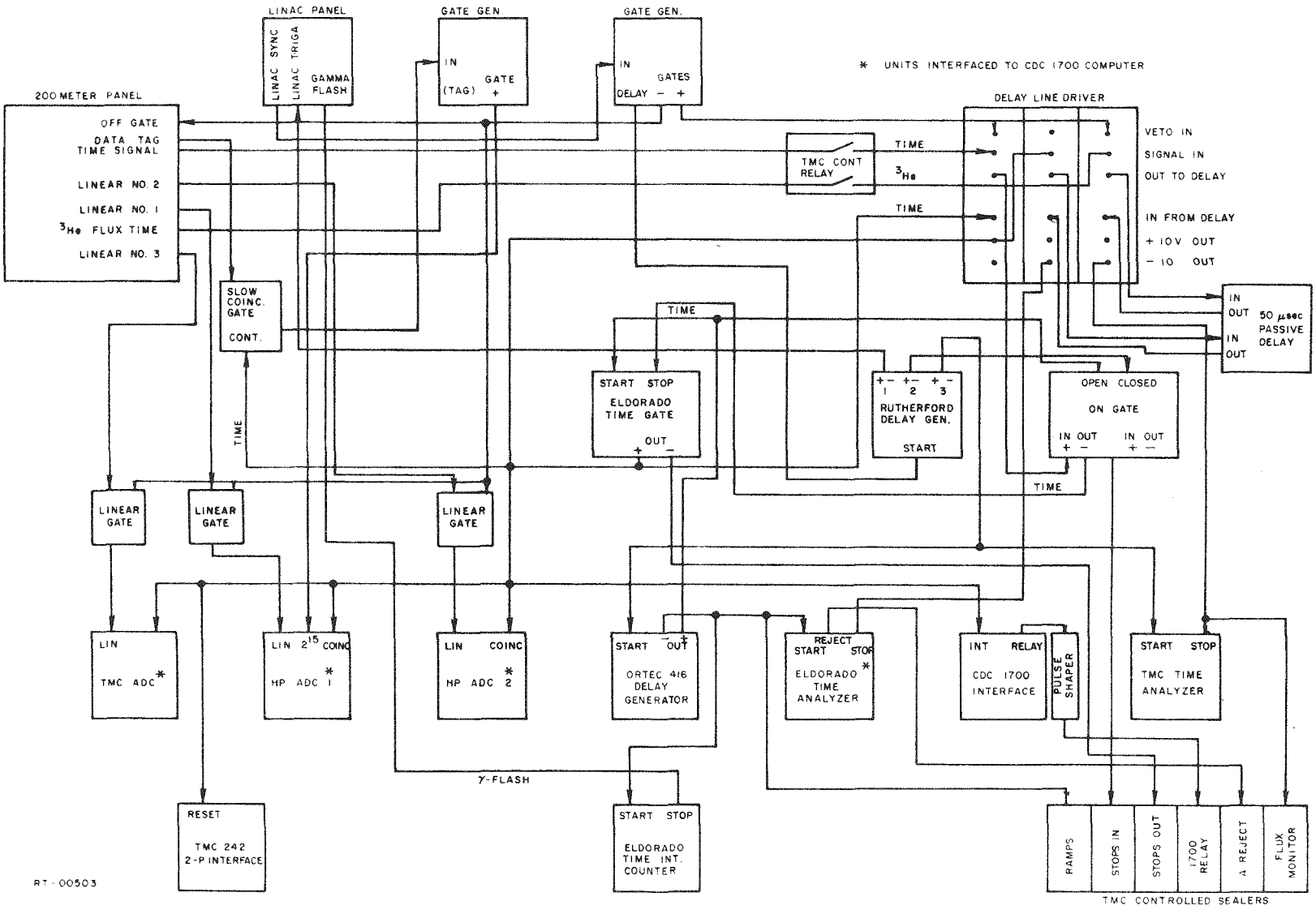

Fig. 6. Block diagram of the electronic circuits employed in obtaining the ion chamber data.

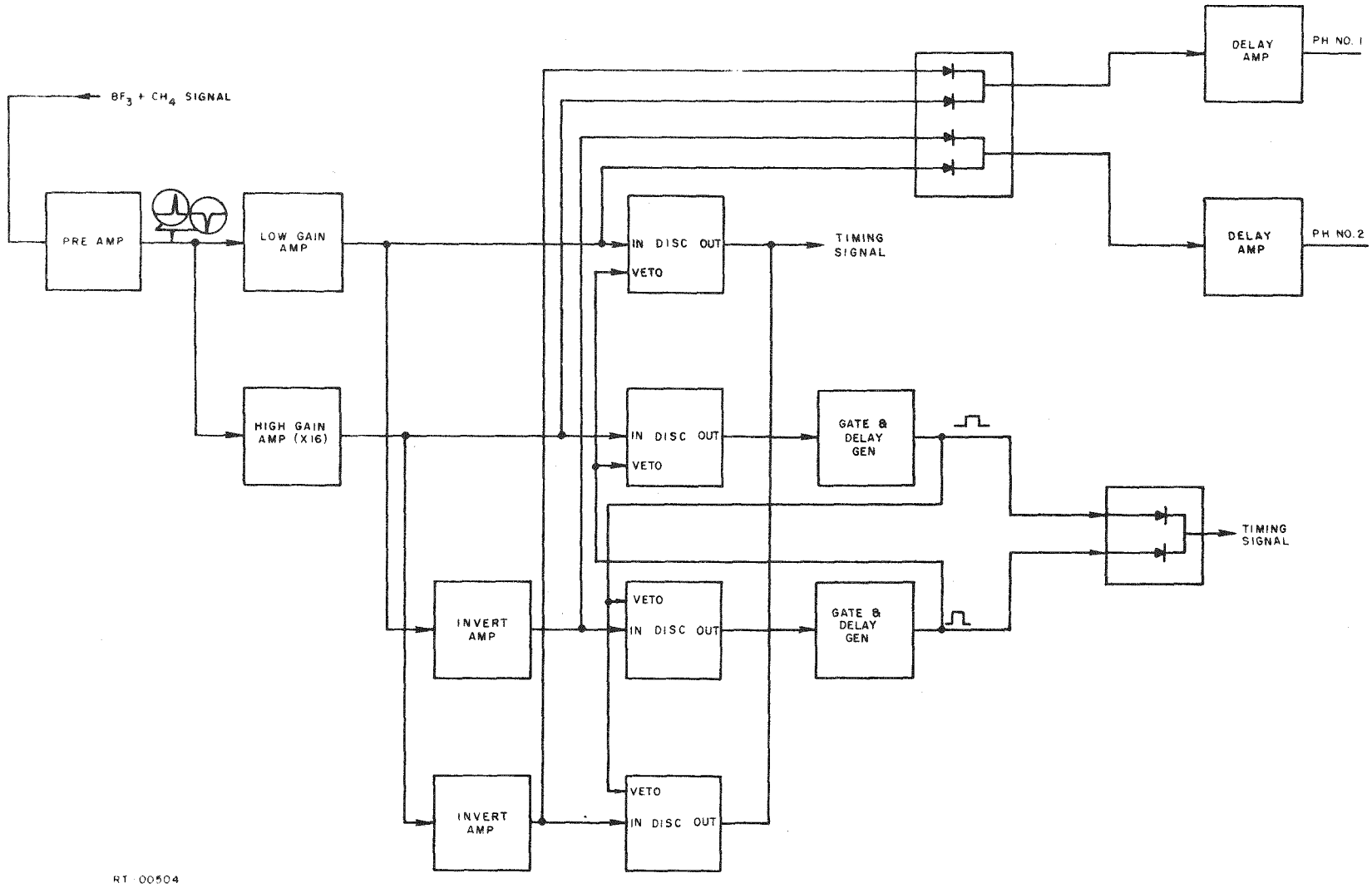

Fig. 7. Block diagram of the circuits used in collecting data from the BF_3 proportional counter.

3.2 COMPUTER PROGRAM

The main features of a CDC 1700 data-acquisition program, which was written specifically for these measurements, are described here briefly.

An undelayed pulse derived from the time pulse used to stop the time digitizer is used to interrupt the computer. This causes the computer to form an orderly termination of the main program and to initiate an interrupt processing routine. This interrupt routine reads and stores the contents of the three analog-to-digital converters, as well as the time digitizer, and stores them in one of two core buffer arrays. The buffer address is incremented, and then control is returned to the main program.

The main program sorts the data contained in the buffers to form time-of-flight and pulse-height displays on an interfaced oscilloscope. One time-of-flight display and three pulse-height displays corresponding to each of two arbitrary neutron energy bounds can be formed. Another set of such displays with the same energy bounds can be formed which corresponds to the ON condition of Bit 15 on one of the ADCs. In this way twelve pulse-height and two time-of-flight data displays can be formed. An additional time-of-flight display can be formed corresponding to the status of Bit 14 of the same ADC. Both of these bits are out of the pulse-height range and are set by an external pulse as indicated in the circuit schematics to indicate a coincidence or other condition.

The display of the sorted data is performed on a time-available basis. The array to be displayed is selected via a thumbwheel switch matrix. When a buffer array is full, the contents are written on disk even if the sorting of that array is not complete. The data storage is then switched to the other buffer.

This page left blank intentionally.

4. NEUTRON FLUX DETERMINATION

The H(n,n) cross section below 1 MeV is almost completely s-wave. This implies that the angular distribution of the reaction is isotropic in the center-of-mass system and, since the proton mass is almost equal to the neutron mass, the energy distribution of the recoiling protons is rectangular with an upper energy limit approximately equal to the incident neutron energy.

Such recoil protons can be observed above ~ 200 keV using liquid or solid hydrogenous scintillators. However, the very nonlinear response and the relatively large gamma-ray sensitivity of the scintillators rule out these detectors in the energy region of interest here.

4.1 PROPORTIONAL COUNTER COMPOSITION AND PULSE-HEIGHT RESOLUTION

In the present measurements the flux determinations are based exclusively on events observed in gas proportional counters. Two such counters with essentially identical construction features were used. The counters consist of a thin stainless steel cathode which is positioned parallel to the neutron beam. The cathode is terminated at the neutron entrance end by a thin $A\ell_2O_3$ ceramic window which also supports the anode wire. The mechanical specifications of the counters are listed in Table 1.

Table 1

MECHANICAL SPECIFICATIONS OF PROPORTIONAL COUNTERS

Cathode:	2.00 ± 0.01 in. diameter 3.04 stainless steel 0.036 in. wall
Anode:	0.002 in. diameter tungsten
End Window:	$A\ell_2O_3$ ceramic
Connector:	HN magnesium with $A\ell_2O_3$ insulator
Active Length:	61.8 ± 0.6 cm

One of these counters has been filled with methane (CH_4) and a small admixture of nitrogen, which allows a determination of the response to monoenergetic 615-keV protons from the $^{14}N(n,p)^{14}C$ reaction. The relative half width (the half width divided by the peak energy) of the $^{14}N(n,p)^{14}C$ peak is 0.12 at the 4000-V operating voltage of the counter when a 1-μsec shaping time constant is used in the linear amplifier. The major contribution to the observed half width is the nonuniformity of the electron multiplication in the counter. This nonuniformity is the result of slight imperfections in the anode wire and field fringing at the ends of the counter. An improved relative half width can be obtained at lower operating voltages (e.g., 0.08 at 3600 V) at the expense of a reduced signal/amplifier noise ratio. However, this resolution effect does not constitute an important factor in the neutron detector efficiency, and the higher operating voltage was chosen in order to improve the signal/amplifier noise ratio.

The second proportional counter was filled with hydrogen plus a small admixture of methane to shorten the electron collection time. This counter also has a small nitrogen admixture, but it was not possible to observe the $^{14}N(n,p)^{14}C$ peak. This is because the range of the protons is an appreciable fraction of the counter radius, and thus the response peak is severely broadened by proton-wall interactions.

The gas compositions of both counters were determined by mass spectrometry at the time of manufacture. These compositions are listed in Table 2.

Table 2

GAS FILLING COMPOSITION OF FLUX PROPORTIONAL COUNTERS

	Volume %	
Constituent	CH_4 Counter	H_2 Counter
Nitrogen	5.0	3.04
Methane	94.0	5.41
Oxygen	0.0012	0.042
Carbon dioxide	0.0010	0.0006
Argon	0.0032	0.0017
Hydrogen	---	91.5

4.2 TIME RESOLUTION

The electron mobility and electron multiplication characteristics of methane and hydrogen plus methane are quite different under similar operating conditions. Methane exhibits a very high electron mobility combined with a moderate gas amplification, whereas hydrogen exhibits a rather low electron mobility and high gas amplification. For these reasons the methane filled counter was used at the upper end of the neutron energy region investigated, and the hydrogen-filled counter at the lower end.

The time at which a given event is observed will depend upon the radial location of the event in the cylindrical counter due to the finite charge collection time. The half width of the time distribution of the observed events is a measure of the timing characteristics of the counter. Information on the time characteristics was obtained in three ways:

1. The counter was exposed to a Pu(Be) neutron source and the gamma ray resulting from the neutron decay of the excited ^{13}C nucleus was observed with a fast plastic scintillator. The dispersion of the charge collection due to coincident proton recoils was observed using a time-to-amplitude converter.

2. The width of the current pulse out of a fast current-mode preamplifier[11] was observed with an oscilloscope when the counter was illuminated by a very short and intense gamma burst from the linear accelerator.

3. The time distribution for the detection of prompt gamma rays from the linear accelerator was observed when the accelerator intensity was reduced to the point at which, on the average, less than one gamma ray per accelerator burst struck the counter.

The results of all three of these determinations are listed in Table 3. Since the time resolution of the counters yields a neutron energy resolution width which tends to be small compared to the energy dependence of the neutron spectrum being measured, the time resolution is a relatively unimportant effect in the neutron flux determination.

Table 3

PROPORTIONAL COUNTER TIME RESOLUTION

Gas	Method[a]	Time Distribution (μsec) 50% Width	10% Width
Methane	1	0.66	
	3		0.7
Hydrogen	- -	1.28	3.8
BF_3 + 10% CH_4	1	2.78	4.35
	3		3.0
	2	2.88	5.7
BF_3	- -	3.16	4.59

[a] 1. Time difference between detection of gamma ray in fast plastic scintillator and proton recoil in counter.

2. Time dispersion of very low level gamma flash.

3. Width of current pulse out of fast current mode preamplifier.

4.3 GAMMA-RAY DISCRIMINATION

Gamma rays produce ionization in the proportional counters primarily via Compton recoil electrons ejected from the counter walls. The gamma rays originate from both natural radioactivity in the vicinity of the counters and activity associated with the linear accelerator burst. Thus the gamma-ray events can be expected to have both steady-state and time-dependent components. The steady-state component can be easily subtracted by measuring the counting rate before the Linac burst, but the correction for the time-dependent component of the background is not so straightforward. The magnitude of the time-dependent component was reduced approximately a factor of two by placing an annular collimator in the neutron beam to shield the counter walls from the neutron-producing target. The collimator consisted of three inches of lead and three inches of polyethylene and was placed about one meter ahead of the proportional counter. The dimensions of the collimator, 1.875 in. i.d. x 2.125 in. o.d., were chosen to shield the counter walls completely after allowing for the 1:700 divergence of the

neutron beam. The collimator was accurately aligned by using a gas laser at the neutron-producing target to cast a shadow of the collimator on the counter. The collimator also has the advantage of reducing the number of protons which lose part of their energy in the counter walls by eliminating the neutron beam in the vicinity of the walls. The calculated response at 1 MeV, with and without the 1.75-inch collimator in place, is shown in Fig. 8.

Since the Compton electron range in the counter gas is usually much larger than the proton range, the length of the ionization track can be used as a basis for partial gamma-ray discrimination. The discrimination relies upon the fact that the majority of the electron events will produce ionization tracks with appreciably greater radial extension than proton events. This radial extension results in a charge pulse whose rise time at the anode wire is a function of both the electron mobility in the counter gas and the radial extensions of the track.

Two different methods were used to discriminate between fast-rise-time (mostly proton) and slow rising (electron) events. In both of these schemes, the signal from the preamplifier was paralleled into both a linear amplifier with a time constant longer than the charge collection time, and a linear amplifier with a time constant short compared to the collection time. The choice of the short-time constant is dictated by signal/amplifier noise considerations. The shorter time constants tend to produce better discrimination at the expense of a higher amplifier noise level and hence a higher minimum energy bias in the gamma discrimination data channel. The electronic conditions and the energy ranges spanned are listed in Table 4.

Table 4

OPERATING CONDITIONS AND ENERGY RANGE OF FLUX PROPORTIONAL COUNTER

Proportional Counter	High Voltage	Time Constant		Useful Energy Range (keV)	
		Slow	Fast	Slow	Fast (dV/dt Mode)[a]
Methane	4000	1.0	0.05	13-1200	30-1200
Hydrogen	3200	3.2	0.2	0.1-60	0.4-12

[a]The values shown for the useful energy range of the fast amplifier apply to the dV/dt gamma discrimination. The crossover discrimination allows an order of magnitude increase in the upper energy limit.

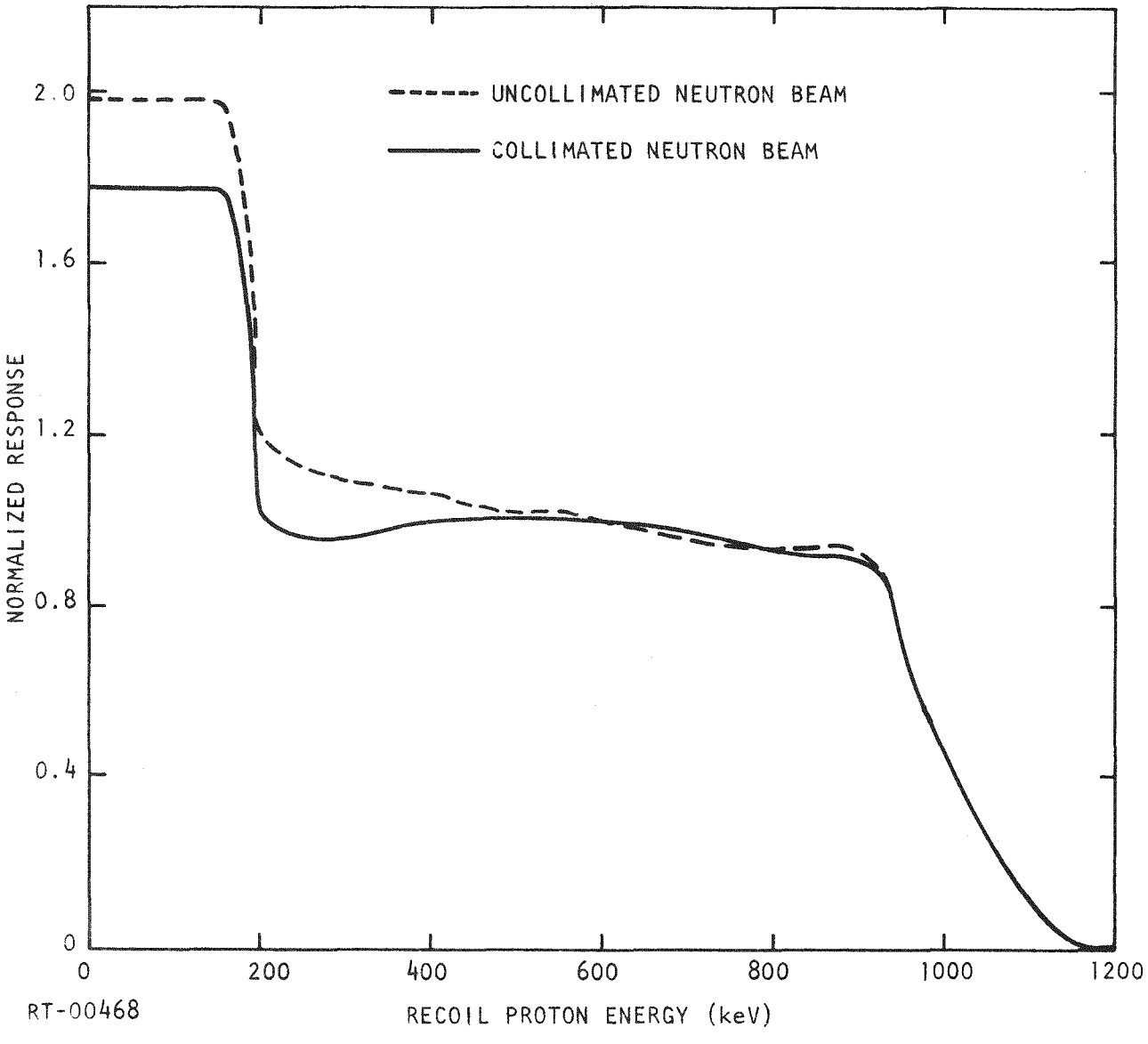

Fig. 8. Calculated response functions for the 2-inch-diameter methane counter at 1 MeV with and without collimator.

The difference between the two gamma-ray discrimination schemes consists in the analysis of the signals from the short- and long-time-constant amplifiers. In the cross-over technique both of the linear amplifier signals are fed to zero cross-over timing discriminators. The output from the long-time-constant discriminator provides the start pulse for a TAC, and the short-time-constant discriminator is delayed and used as the TAC stop pulse. The output of the TAC is then digitized in the data recording system to provide a basis for gamma discrimination. Figure 9 illustrates the discrimination achieved between proton events in the methane counter and ^{60}Co gamma rays. In this example, the fast amplifier shaping time constant was 0.02 μsec and the slow amplifier shaping time constant was 1.0 μsec. The pulse-height distribution out of the TAC is shown. The time channel width was 0.0031 μsec. Since the location of the proton peak is very insensitive to the amplitude of the pulse, the cross-over scheme enjoys a very wide dynamic range. The maximum time difference between the two discriminator outputs is approximately one-half the charge collection time in the counter, since the fast-discriminator output is related to the leading edge of the pulse and the slow discriminator to the mean charge collection time. At very low pulse amplitudes the dispersion in the cross-over time due to the amplifier noise tends to limit the effectiveness of the discrimination. The disadvantage of this technique is the reduced gamma/neutron discrimination capability due largely to the tendency of the fast-amplifier cross-over time to depend slightly on the pulse rise time.

The second gamma/neutron discrimination scheme requires that the amplitude of the short-time-constant amplifier be divided by the amplitude of the long-time-constant amplifier to obtain a measure of the rate of rise of the pulse (dV/dt). In principle, this can be achieved electronically; but usually, as was done here, both pulses are digitized in order to allow the division to be performed as part of the subsequent data analysis.

Figure 10 illustrates the dV/dt gamma discrimination parameter derived from the methane data, and Fig. 11 shows the discrimination achieved for the hydrogen data. The dynamic range of the discrimination is limited by the range of the data channel used to record the short-time-constant pulse

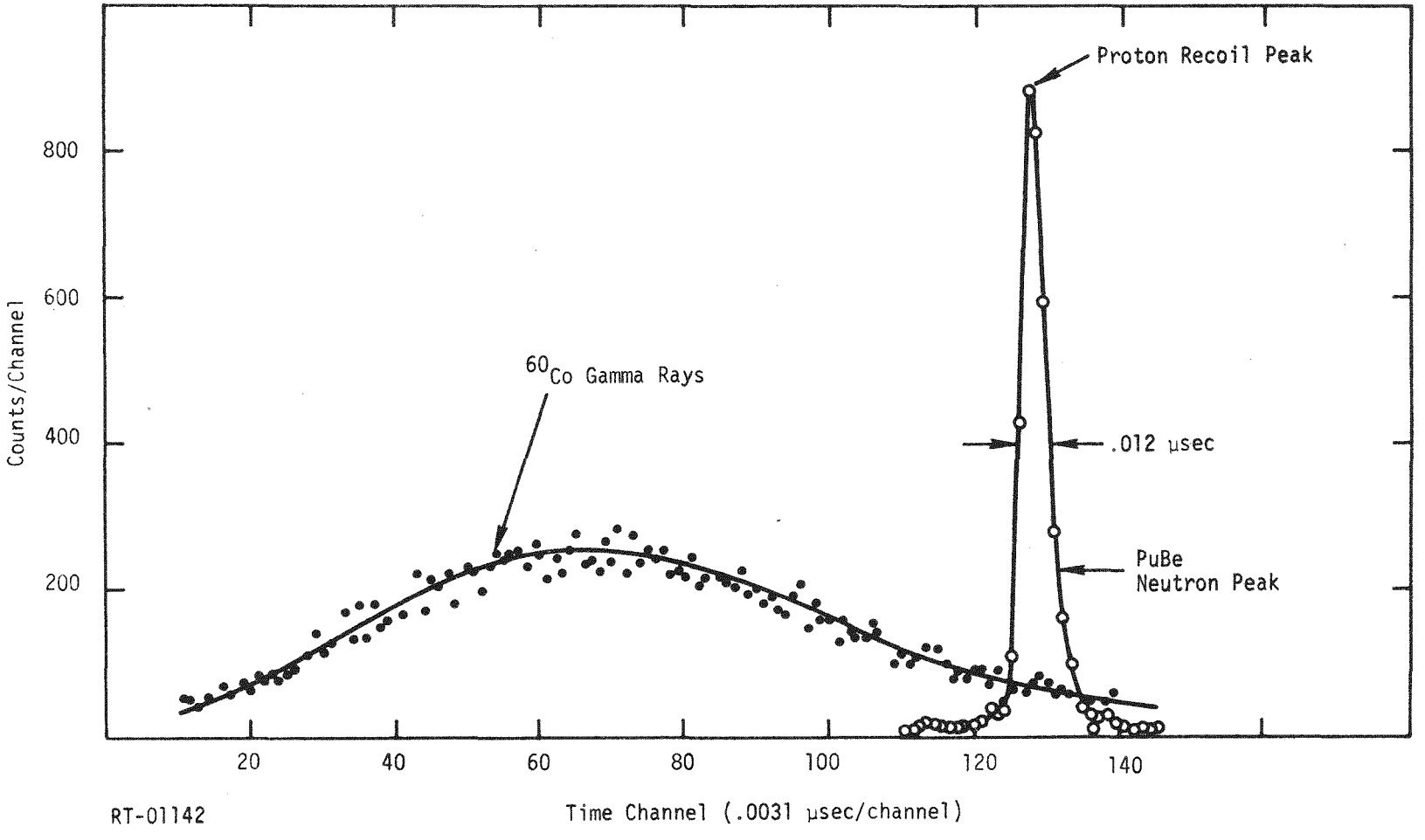

Fig. 9. Neutron/gamma discrimination for the methane-filled proportional counter using the crossover discrimination technique.

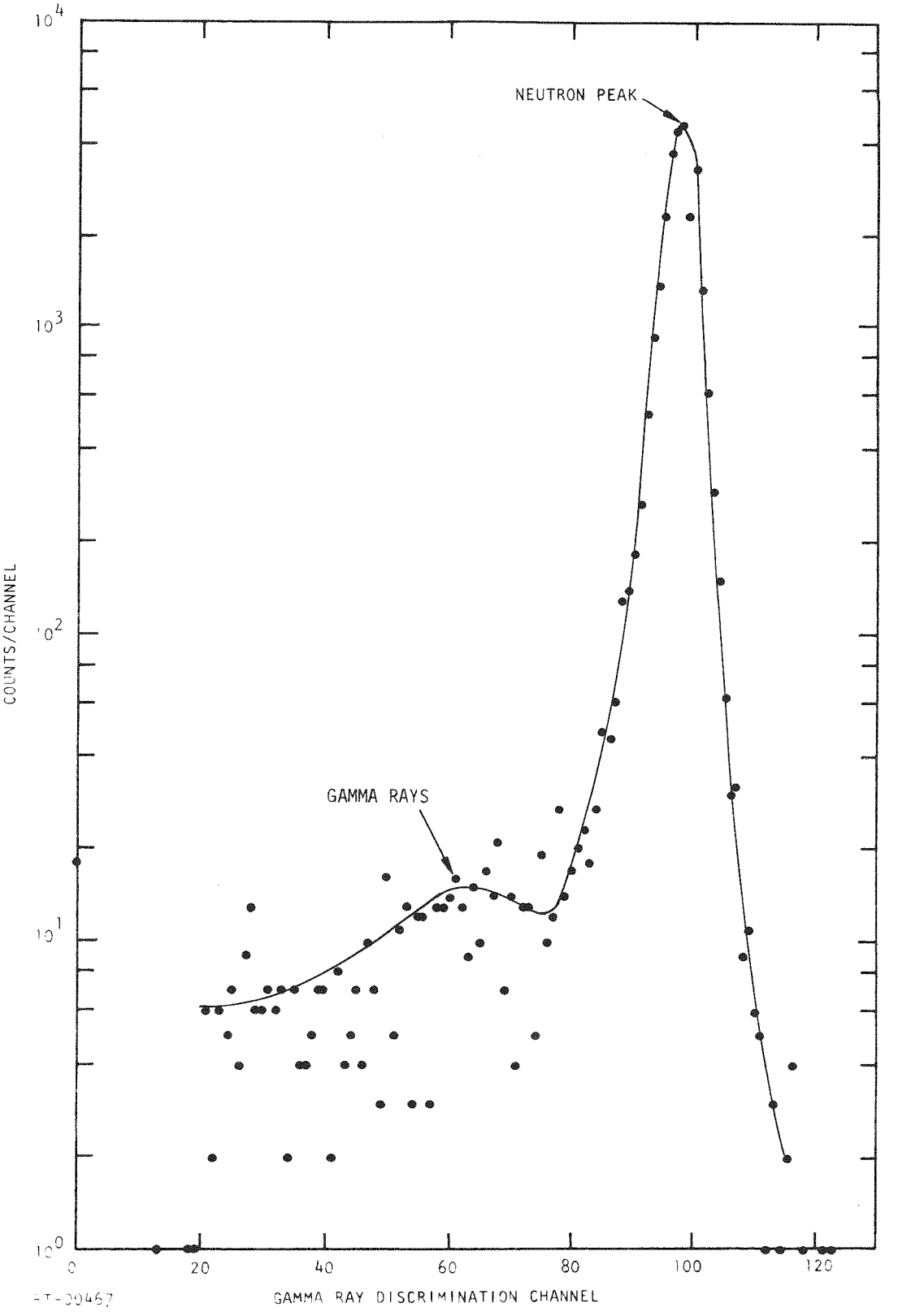

Fig. 10. Neutron/gamma discrimination for methane-filled proportional counter using dV/dT technique (neutron energy interval = 270 to 370 keV; time constants = 0.05 and 1.0 μsec).

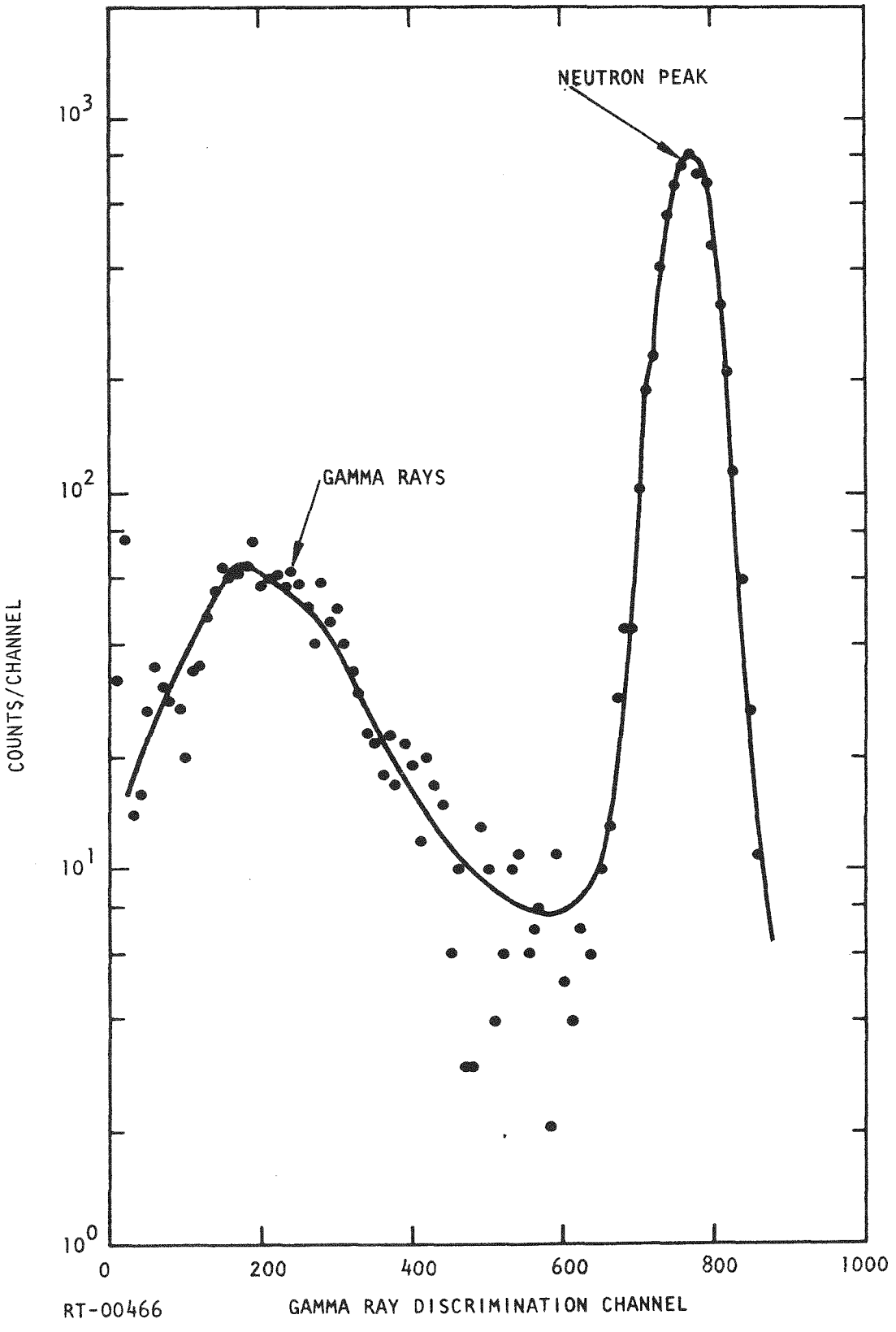

Fig. 11. Neutron/gamma discrimination for the hydrogen-filled proportional counter (neutron energy interval = 2.7 to 3.7 keV; time constants = 0.05 and 3.2 μsec).

amplitude. Since the gamma-ray background tends to be much more severe at low pulse heights, the dV/dt gamma discrimination threshold was set as low as possible. This allowed dV/dt discrimination from 30-1000 keV in methane and 0.4 to 12 keV in hydrogen. Since the accelerator associated gamma rays are largely the result of neutron capture and inelastic scattering in the vicinity of the neutron-producing target, this background decreases at a rate dependent upon the neutron dieaway in the target assembly. On a neutron energy scale as observed at the 230-meter flight path, the time-dependent gamma component becomes insignificant below 100 keV. Thus, the energy regions not contained in the gamma discrimination intervals listed in Table 4 are adequately corrected by subtracting the time-independent (ambient) background.

At the upper end of the energy region spanned by the methane counter, i.e., near 1000 keV, the radial extension of the proton recoil tracks is sufficient to cause some of the neutron events to be confused with gamma-ray events. The effect is illustrated in Fig. 12 for 300- and 1000-keV events. To avoid this difficulty the time-dependent gamma component was determined by measuring the time history of events from the counter with a 2-inch-thick slab of polyethylene in the neutron beam. After correction for the finite neutron transmission of the filter, the net time history was normalized to the open beam data using the gamma discrimination data recorded in both cases. The open beam time history recorded for the methane counter is illustrated in Fig. 13. Also shown is the time-dependent gamma-ray background subtraction. As can be seen from the figure, the time-dependent background is a maximum of $\approx 3\%$ at 1000 keV and diminishes at lower energies.

4.4 DUAL-GAIN DATA RECORDING SYSTEM

The fact that the maximum pulse amplitude of the observed events is closely proportional to the neutron energy, combined with the very large energy span of these measurements, requires that the data-acquisition system record a very large dynamic range with good pulse-height resolution. For this reason two long-time-constant linear amplifiers were used to amplify the preamplifier signal. The gains of these two amplifiers differed by

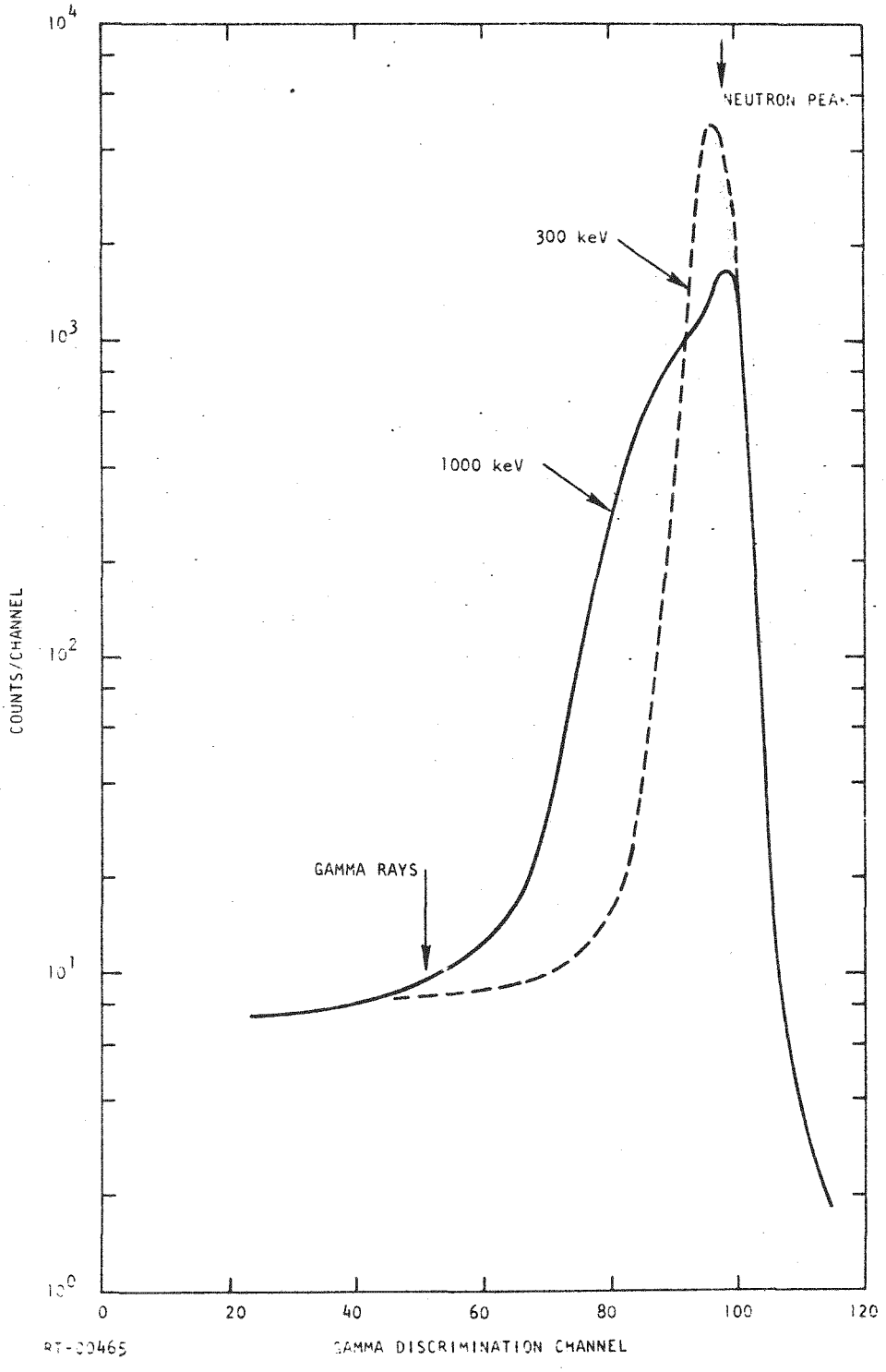

Fig. 12. Broadening of the neutron/gamma-ray discrimination peak in the methane counter at 1 MeV due to the finite radial extension of the recoil proton tracks. The 300 keV discrimination peak is shown for comparison.

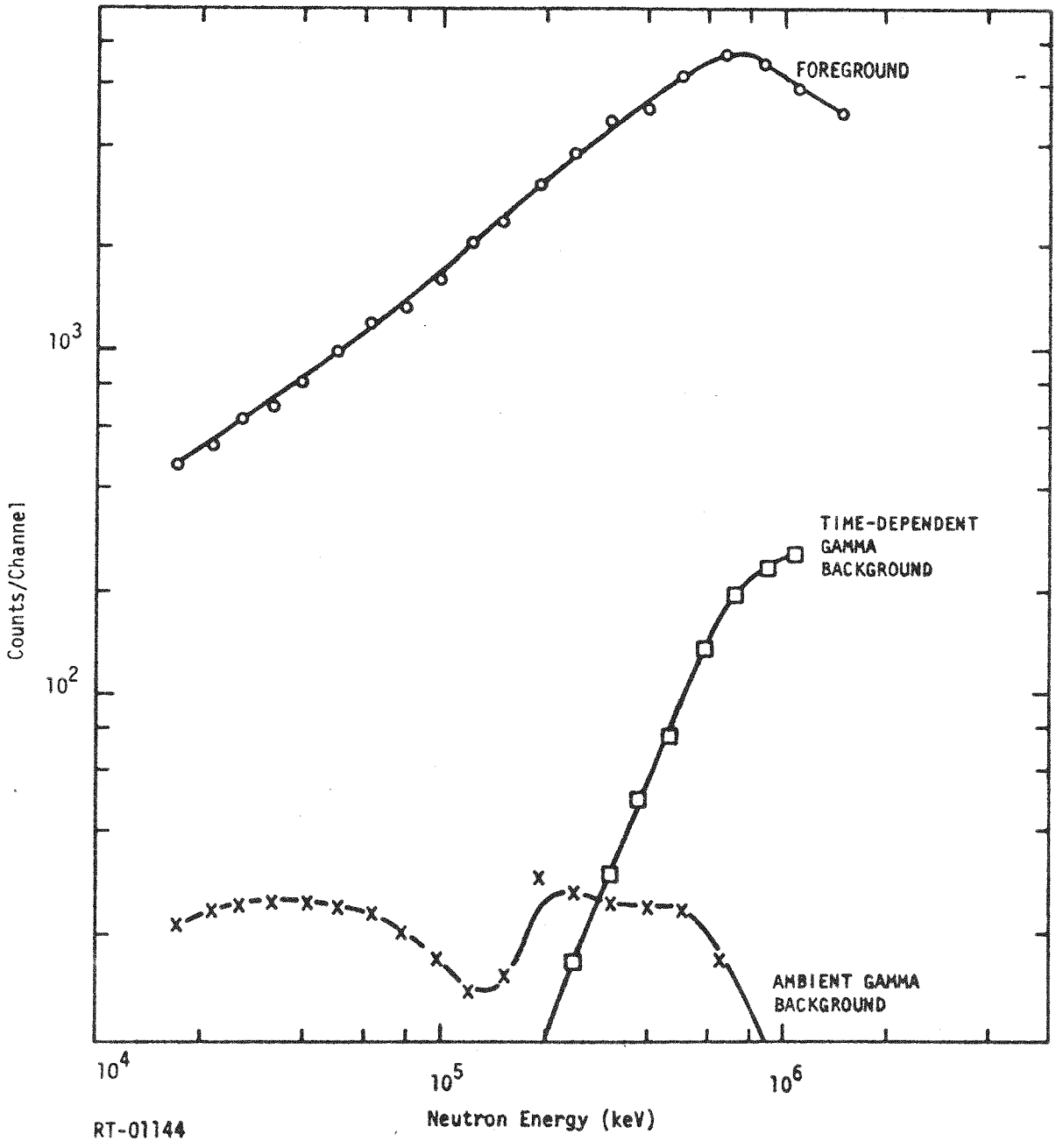

Fig. 13. Foreground vs background in the methane time-of-flight data.

approximately a factor of 16, and the outputs were individually digitized in 1024-channel analog-to-digital converters (ADC). The simultaneous recording of the events allowed the ratio of the amplifier gains to be determined very accurately by sorting the data in overlapping pulse-height regions and noting the average ratio of the channel numbers for each event from the two ADCs. This technique also allows the determination of recording system errors. Such errors can arise from small linearity errors in the amplifying/recording system, and in gain anomalies due to the accelerator gamma burst. An example of the gain ratio vs. the low gain ADC channel number for the methane counter is shown in Fig. 14. The data shown in the figure have been corrected for electronic nonlinearities by use of precision pulser data accumulated during the measurements. The pulser has a quoted nonlinearity of <0.1%, and hence the locations of the pulser peaks were used as reference points for the linearity correction. The interpolation between the measured points was achieved using polynomial fits to the pulser data. The flatness of the gain ratio curve shown in the figure is largely due to the linearity corrections thus obtained.

The gain ratio curve for hydrogen is shown in Fig. 15. The ratio can be seen to deviate significantly from a constant value below channel 30. This effect arises from overload pulses in the current-mode preamplifier due to very high energy neutron events in the counter which produce low level, but very wide, output pulses from the preamplifier. These anamolous pulses have a significant effect on the measured neutron spectrum when the neutron-energy-dependent pulse-height bias falls below channel 30, which occurs at approximately 4 keV.

The approximate magnitude of the error caused by these anamolous pulses can be obtained by forming the time history of "abnormal" to "normal" gain ratios. This ratio is illustrated in Fig. 16. As can be seen in the figure the abnormal pulses become significant below 4 keV, and hence the flux data can be expected to be unreliable below this energy. Since the overloading of the preamplifier is primarily due to excessive preamplifier gain, the problem just described can be easily eliminated in future measurements by reduction of the preamplifier gain with a corresponding increase in the gain of the linear amplifier.

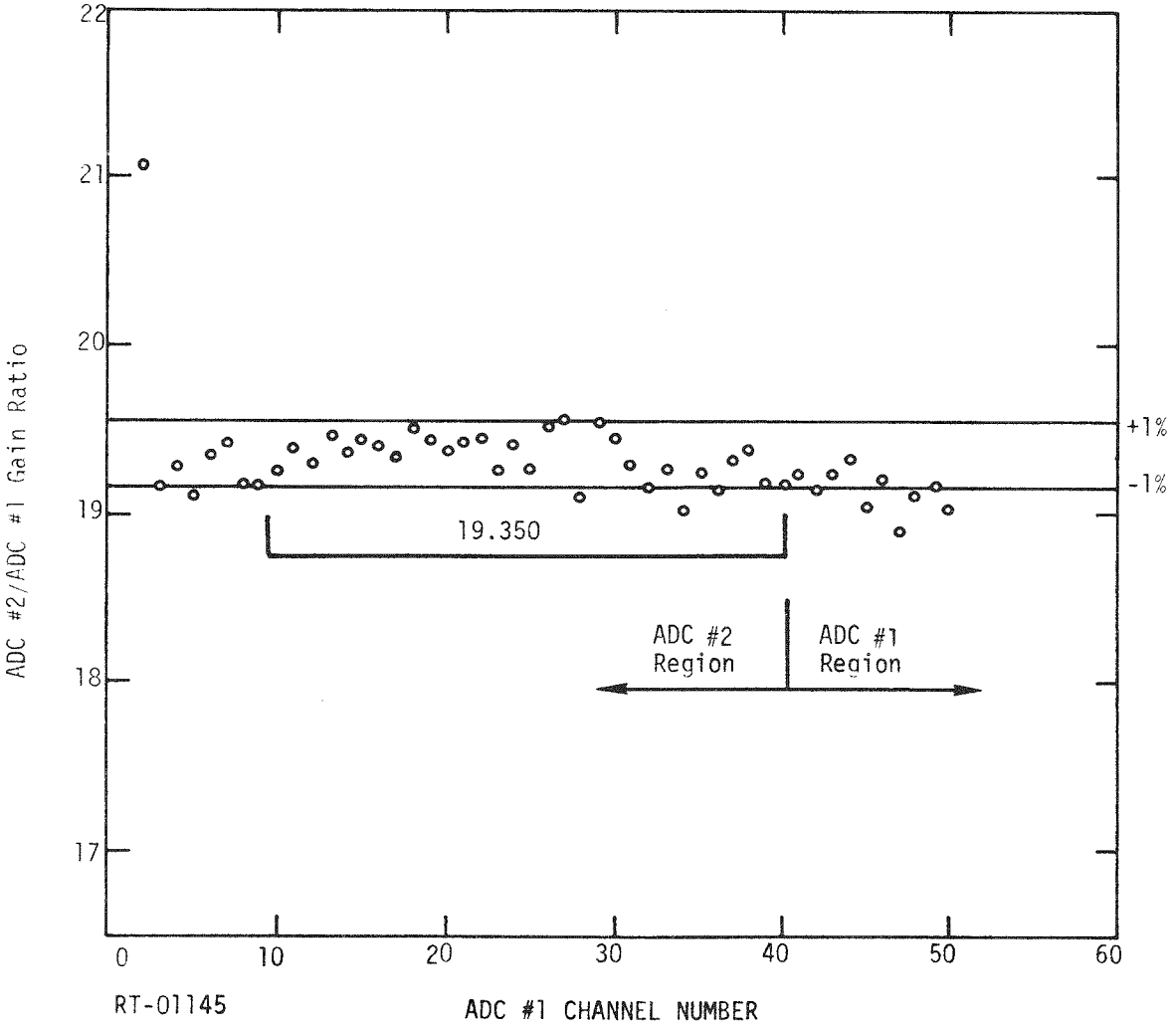

Fig. 14. Average ratio of high gain to low gain ADC pulse amplitude vs the low gain ADC channel number for the methane data. Corrections for electronic nonlinearities have been applied.

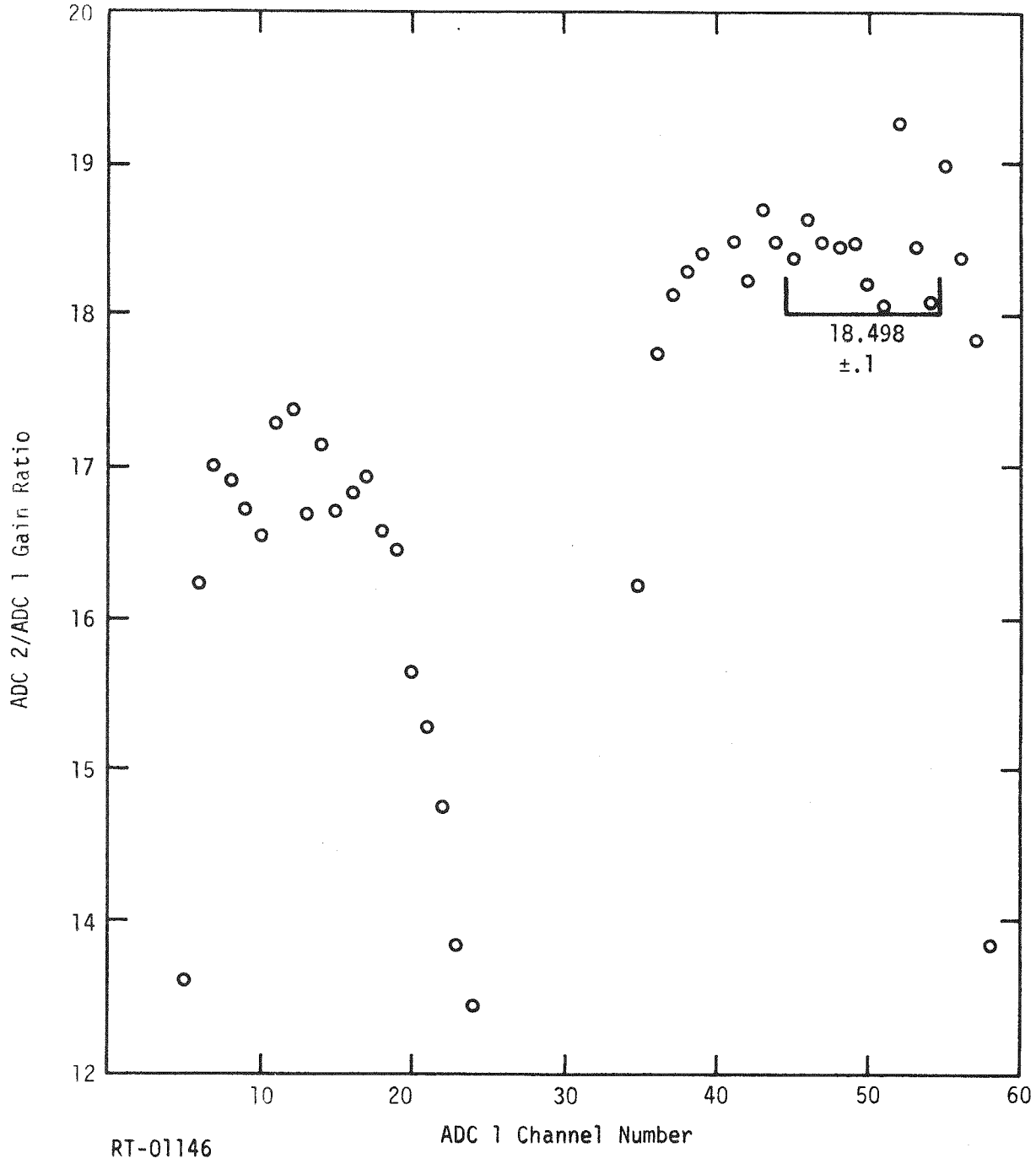

Fig. 15. Ratio of high gain to low gain ADC pulse amplitude for hydrogen data. Note strong deviation from constant value near channel 30 due to overload pulses.

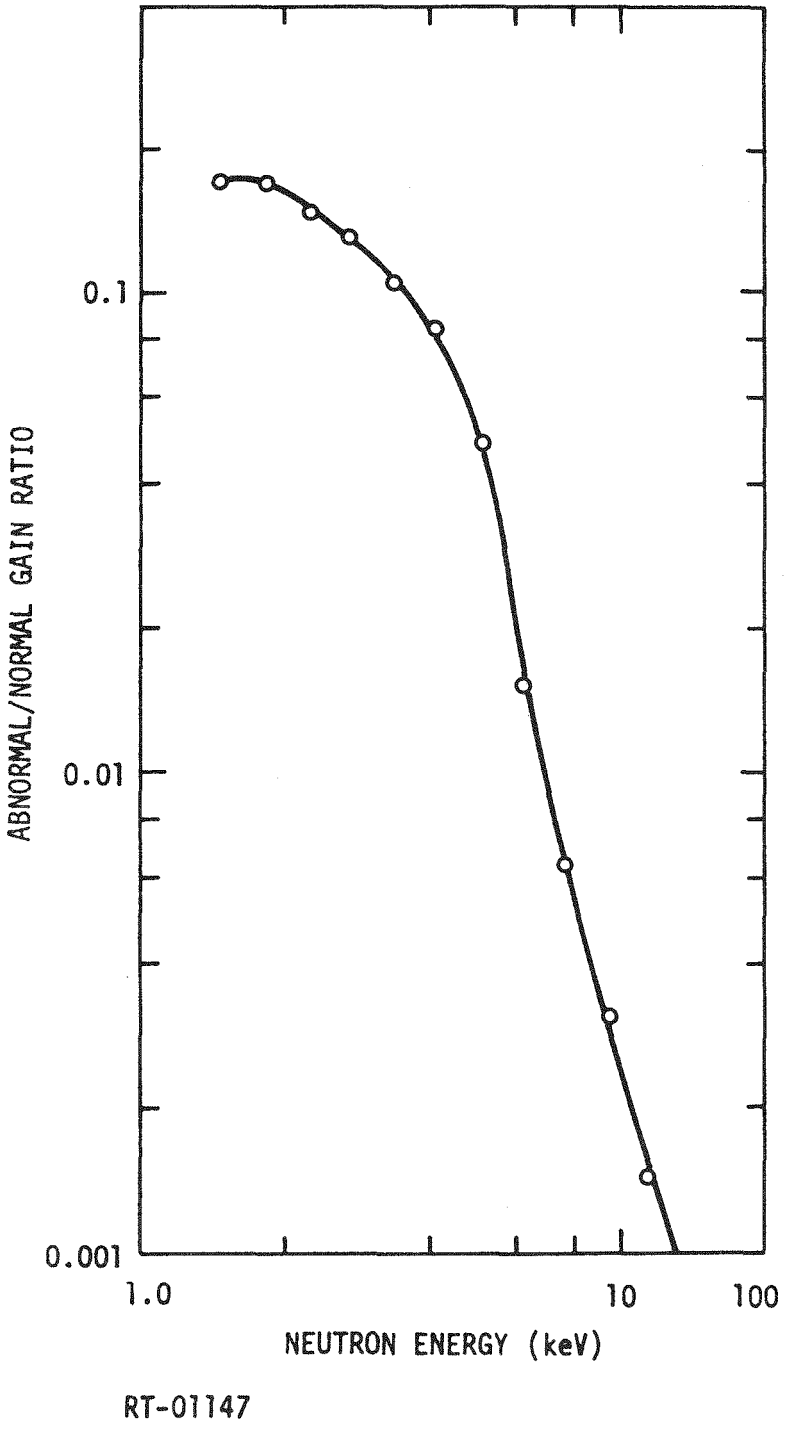

Fig. 16. Ratio of abnormal to normal gain ratio events included in time-of-flight distribution (cf. Fig. 14).

4.5 EFFICIENCY CALCULATIONS

The time-of-flight histograms are formed by sorting the multiparameter data into time bins with pulse-height bounds which are a fixed fraction of the neutron energy (as calculated from the time parameter). The methane data were sorted with bounds of 0.35- and 1.5-times the neutron energy, and for the hydrogen data these bounds were 0.3 and 1.5. The lower bound (or "bias") eliminates carbon and nitrogen recoils from the time history, and the upper bound tends to reduce background errors. This procedure would result in a constant biasing efficiency if the counter response were ideally rectangular, but several effects tend to cause the actual response to deviate significantly from the ideal. We will discuss briefly each of these effects and describe their representation in the computer code WEND.[3]

4.5.1 Wall Effect

In the first phase of the calculation, Monte Carlo techniques are used to generate events in the active regions of the counter from which a recoil proton might escape by passing into the inactive region or the wall. The energy expended in the active region is recorded as the pulse amplitude. The region shielded by the wall collimator is excluded from the allowed interaction region. This "wall effect" produces an appreciable change in the pulse-height distribution only in the high-energy end of the methane data.

4.5.2 Amplifier Noise

The electronic noise of the recording system is measured in terms of the half width of the peaks obtained by inserting a low-noise test pulse at the input of the preamplifier. The code folds a Gaussian function of this width into the response function. This contribution to the response function is small in all cases and introduces a negligible uncertainty into the biasing efficiency.

4.5.3 Multiplication Nonuniformity and Finite Neutron-Energy Bin Width

The counter multiplication nonuniformity discussed previously is folded into the distribution as a Gaussian, and the relative width of the neutron

energy interval used in sorting the pulse-height distribution is folded into the response function as a rectangular function. Since both of these effects are multiplicative, the function widths are linearly related to the pulse height. These two effects tend to be the predominate resolution effect on the response function except at the low-energy end of the hydrogen data. The uncertainty produced in the biasing efficiency is again negligible.

4.5.4 Ion-Pair Statistics

The energy expended per ion pair, W, is about 36 eV in hydrogen. At the lower neutron energies the finite number of ion pairs produced will cause a statistical fluctuation in the pulse amplitude. The standard deviation of this fluctuation is related to the inverse square root of the number of ion pairs via the Fano factor.[12] This effect is the predominant resolution contribution at neutron energies near 1 keV, where we find good agreement with the Fano factor quoted for proportional counters (F = 0.44). This effect is also multiplicative and is folded into the response function as a pulse-height-dependent Gaussian.

4.5.5 Proton Energy Dependence of W

The number of ion pairs produced per unit proton energy tends to decrease as the proton energy decreases, since non-ionizing processes such as elastic scattering tend to become an increasingly important energy loss mechanism. This decrease in the relative magnitude of 1/W, which we shall call the "ion-pair defect", is of prime importance in the present measurements since the biasing efficiency tends to be closely related to this quantity. Several measurements of this effect have been reported in the literature[12-16] and a calculation of the effect has been made by Dalgarno and Griffing.[16] Both the measurements and calculations are of insufficient accuracy to satisfy the present need, and hence the ion-pair defect was determined both directly and indirectly from the methane and hydrogen data.

The defect was determined directly from the position of the leading edge of the pulse-height distribution relative to the neutron energy for several neutron energies. The pulse-height energy scale was normalized at the highest measured energy, i.e., 1 MeV in methane and 50 keV in hydrogen. The lower

energy limits of the determinations made in this fashion were 15 keV in methane and 1 keV in hydrogen.

The results of these determinations are illustrated in Figs. 17 and 18. The methane results agree well with the measurements of Rogers[12] using the MTR filtered neutron beam facility, but the results for hydrogen do not. Rogers' results for hydrogen indicated that W was independent of neutron energy down to at least 2 keV. The apparent discrepancy between these and the present measurements suggests that there may be some subtle effect associated with either gas impurities or operating conditions. Our result for hydrogen is in much better agreement with those of Werle et al.,[13] who measured response functions in a slowing-down-time spectrometer. The results of Bennet[15] were based on assumptions about the neutron spectrum in a depleted uranium assembly and hence yield little explicit information about the proton energy dependence of W. The determinations of Bennet[14] for the 1.32-keV deuterons from the $p(n,\gamma)d$ reaction are in good agreement with our data.

Since it is necessary to include energy regions below the lowest experimentally determined ion-pair defect, use was made of the fact that the pulse-height distributions exhibit a constant slope at least above the lowest measured point, i.e., above 4 keV in methane and 0.4 keV in hydrogen. The slope was determined by fitting the measured response function with a first degree polynomial. This slope was then used to extrapolate the pulse-height distribution to zero pulse height.

This procedure leads to some error, since the ion-pair defect can be expected to exhibit a pathological behavior near zero energy. However, it appears to be the best procedure until any data become available which would better define the very low energy behavior of the defect.

The computer code treats the measured defect in the following way. The approximate defect is first calculated from the expression

$$D = 1 - 1/(CE+1) \quad , \tag{1}$$

where E is the proton energy and C is a constant. Equation (1) reproduces the observed defect with a precision of $\approx \pm 3\%$ throughout the measured region.

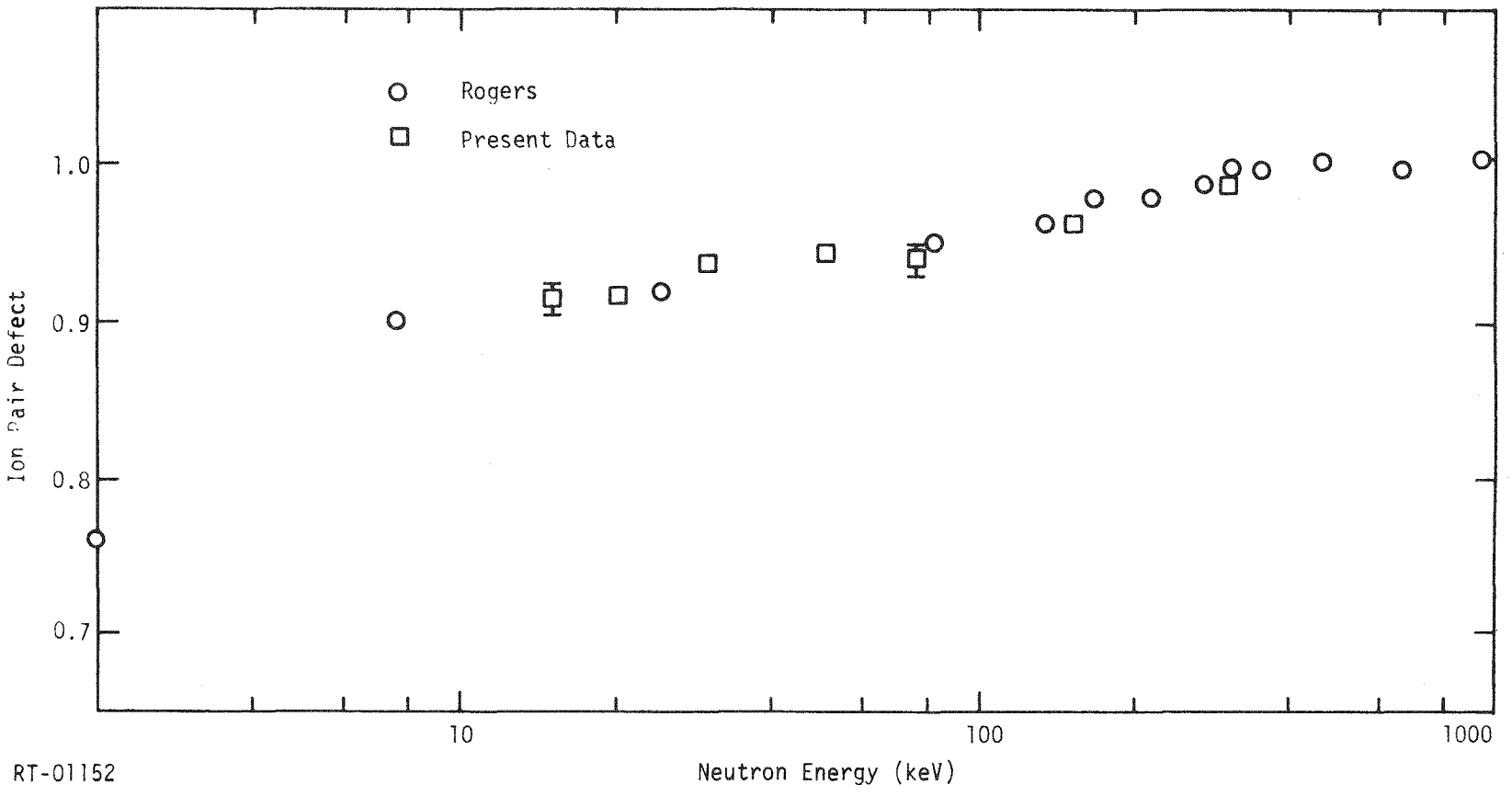

Fig. 17. Nuetron energy dependence of the ion pair defect (1/W) for the methane counter.

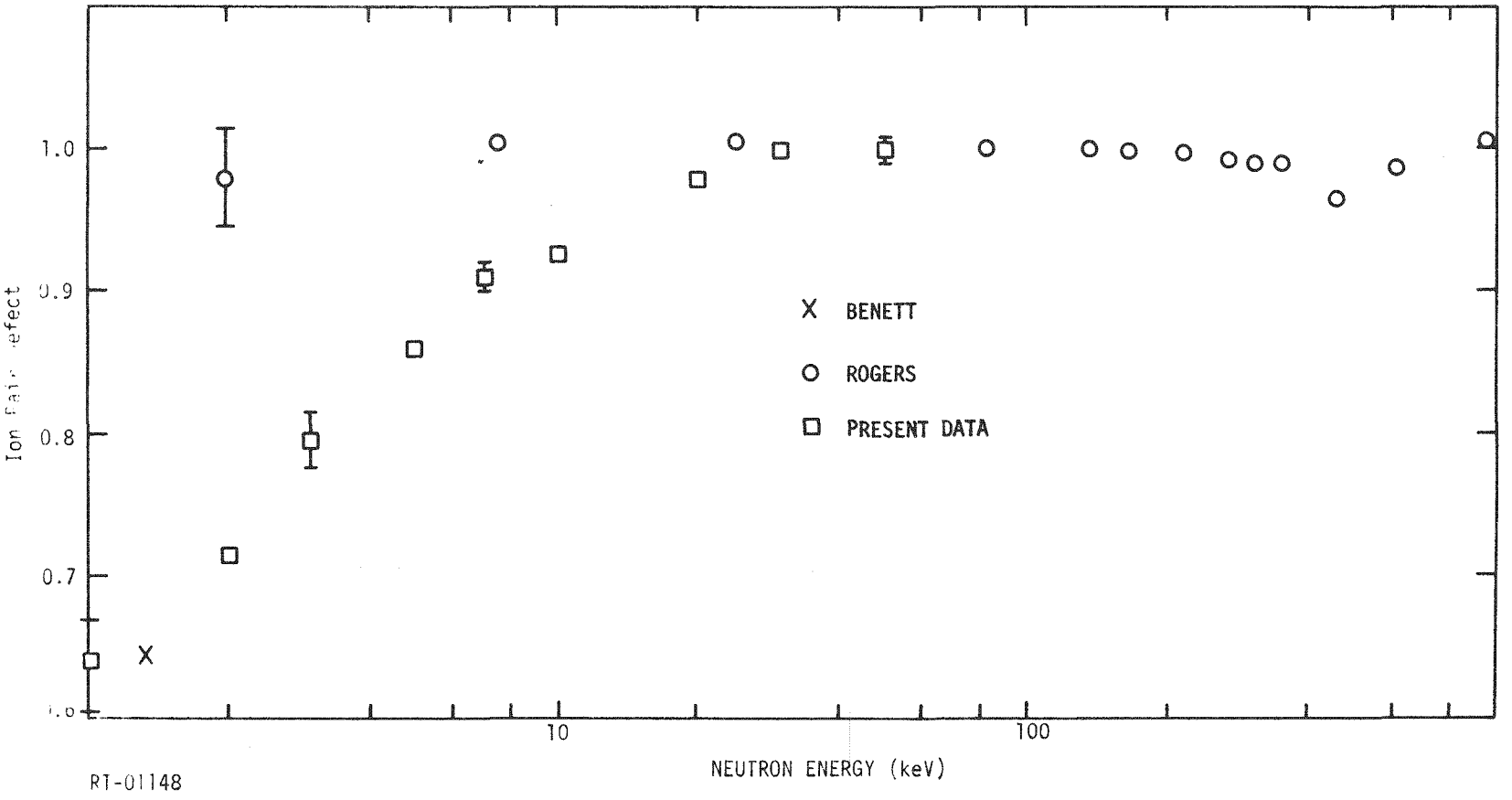

Fig. 18. Neutron energy dependence of the ion pair defect (1/W) for the hydrogen counter.

The difference between Eq. (1) and the measured defect is then determined by linear interpolation from tabular values and is added to the initial results. This procedure reduces discontinuities in the first derivative of the ion-pair defect which would cause structure in the calculated response. When the lower energy limit of the measured defect is reached, the defect is continued by generating energy bins such that each one is narrower than its higher energy neighbor by an amount sufficient to produce the observed slope.

4.5.6 Results

Examples of comparisons between experimental data and calculations are shown in Figs. 19 through 21 for methane and Figs. 22 through 24 for hydrogen. The calculated energy dependence of the bias efficiencies are shown in Figs. 25 and 26.

4.5.7 Beam Uniformity

The two-inch-diameter flux proportional counters sample a relatively small portion of the neutron beam viewed by the 9-inch-diameter useful area of the ion chamber and the ^{10}B slab used with the Ge(Li) detector. The configuration of the flight path ensures the spectral uniformity of the neutron beam, but to obtain an experimental confirmation, the methane flux data were accumulated at three different positions across the neutron beam. The three measurements were found to be in excellent agreement.

4.6 END-WINDOW TRANSMISSION AND SELF-PROTECTION CORRECTIONS

In addition to correcting the data for the energy dependence of the detection efficiency, it is also necessary to apply a correction for the energy dependence of the $A\ell_2O_3$ end-window transmission. The manufacturer's quoted end-window thickness was 0.08 in. ± 0.01 in. To confirm this value, the proportional counters were X-rayed and the film images measured with an optical comparator. The results of these measurements are shown in Table 5.

The theoretical density of $A\ell_2O_3$ is 3.9 g/cm^3, but since alumina ceramics can be made with densities much lower than this the theoretical density

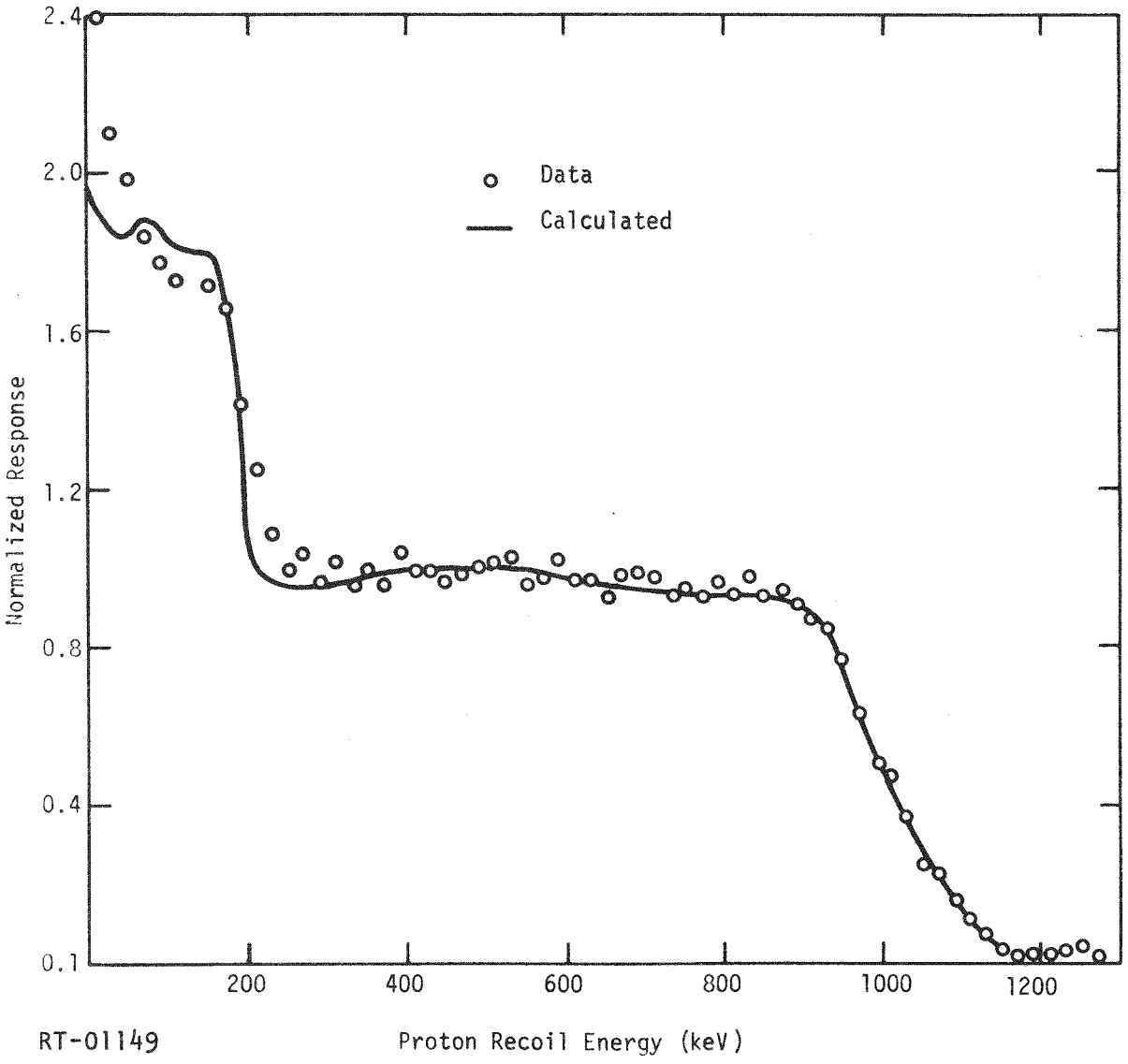

Fig. 19. Calculated vs measured response for the methane counter (neutron energy = 900 to 1100 keV).

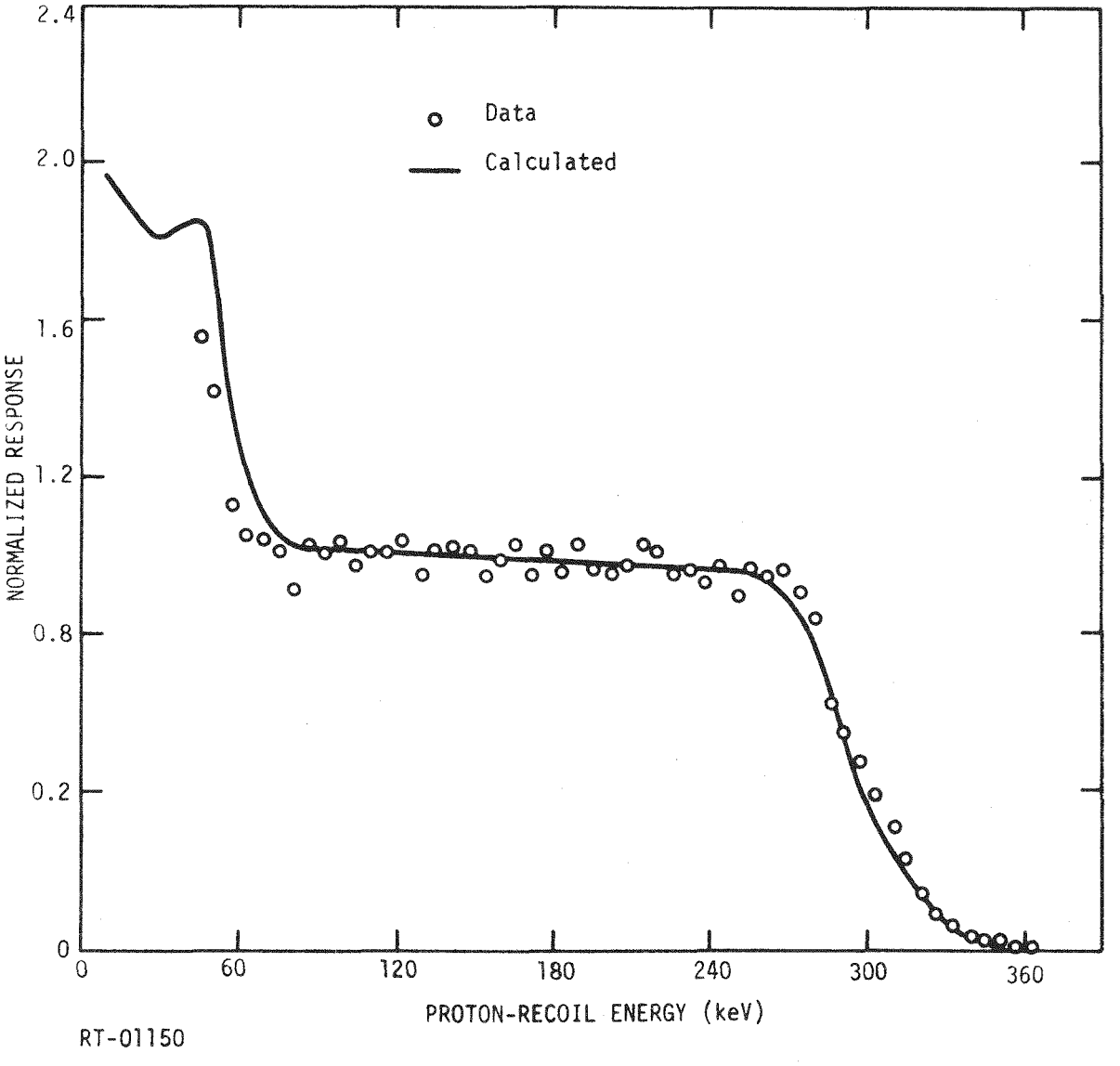

Fig. 20. Calculated vs measured response for the methane counter (neutron energy = 270 to 300 keV).

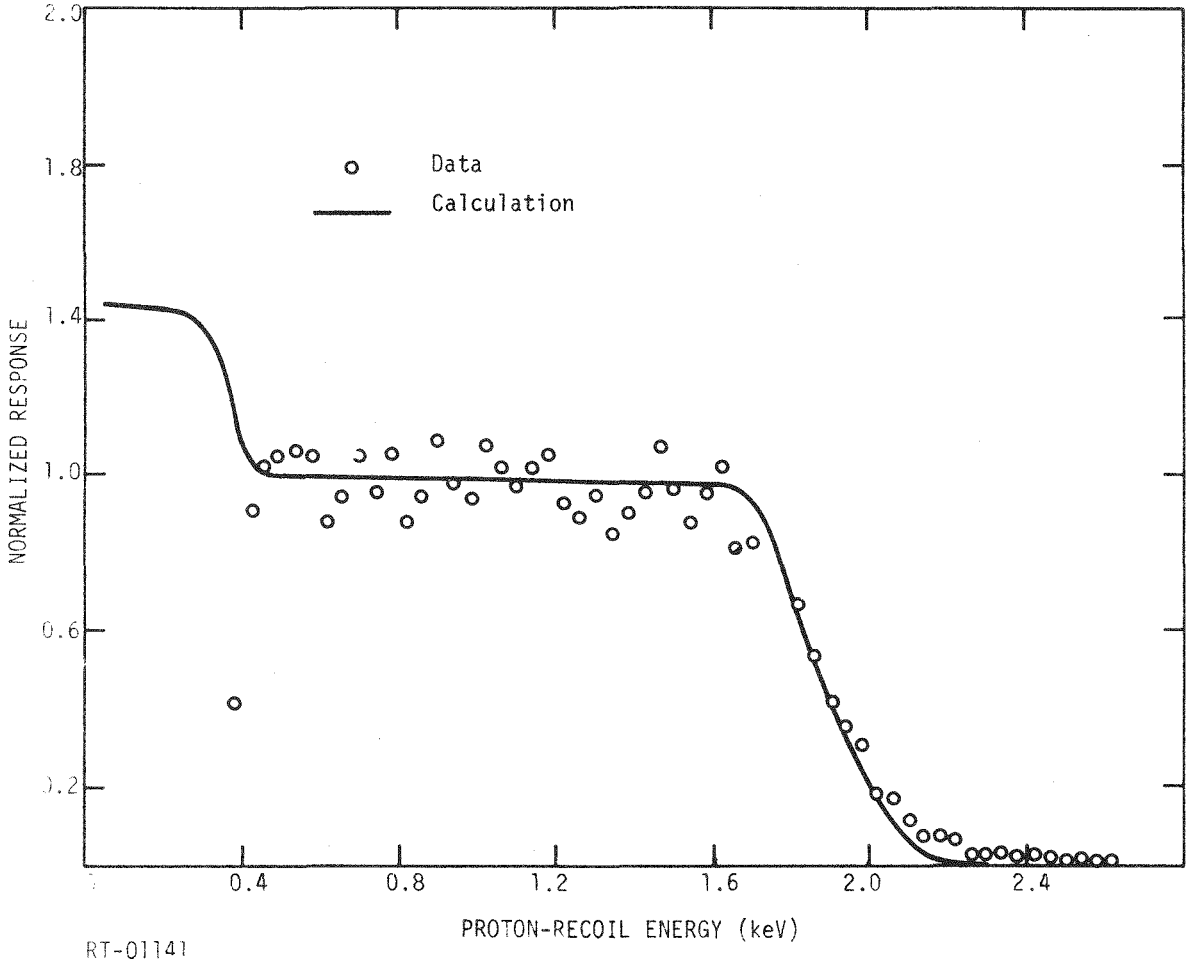

Fig. 21. Calculated vs measured response for the methane counter (neutron energy = 18 to 20 keV).

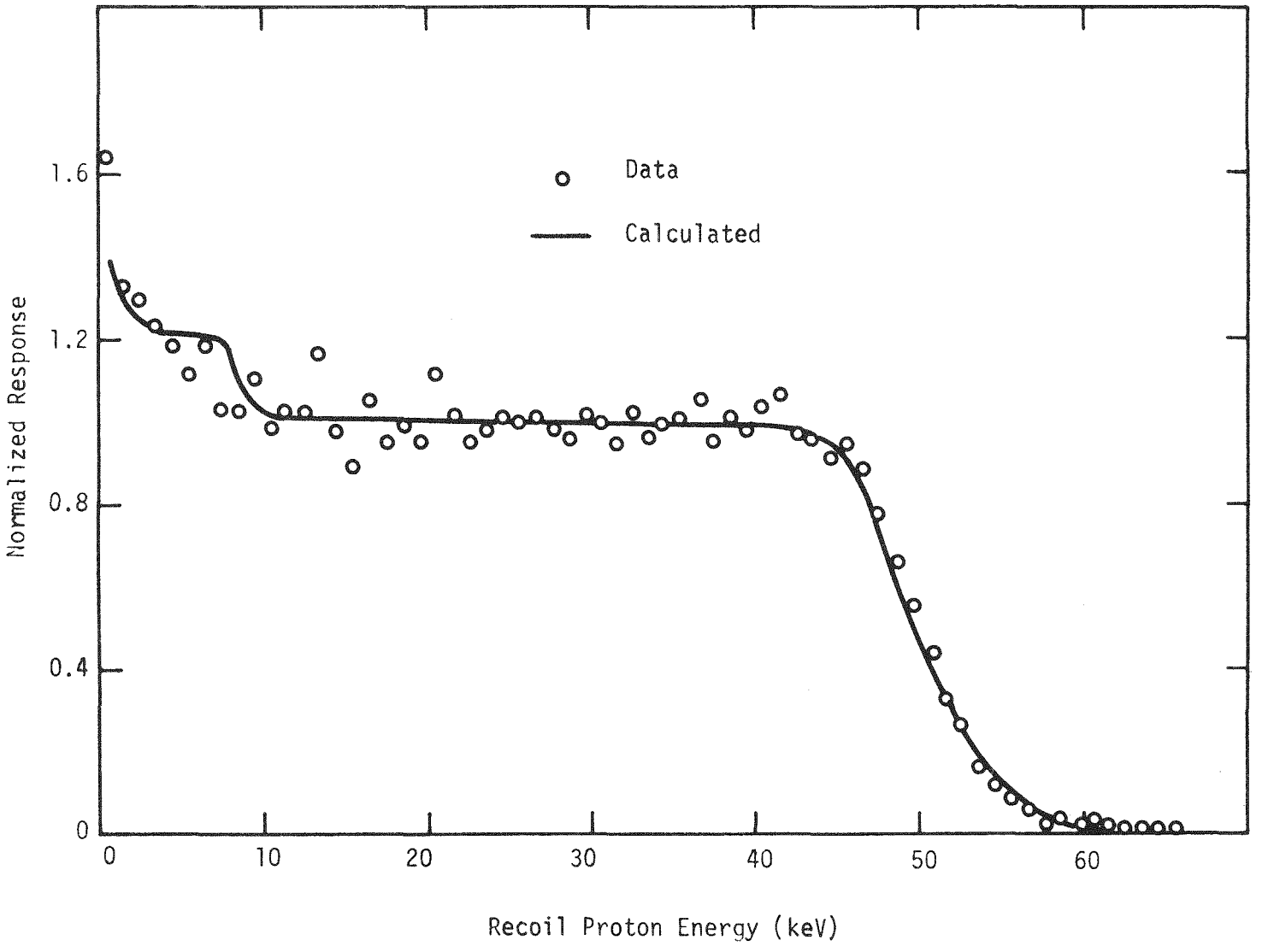

Fig. 22. Calculated vs measured response for the hydrogen counter (neutron energy = 45 to 55 keV).

can only be regarded as an upper limit. Previous measurements of the flux spectrum with stainless steel entrance-window proportional counters indicated a smooth energy dependence of the flux spectrum near the 35-keV aluminum resonance. Since this resonance produces the largest transmission correction, it provided the best point at which to determine the end-window thickness by demanding that the flux spectrum be smooth through this energy region. The density obtained in this fashion was 0.48 times the theoretical density.

Table 5

Al_2O_3 END WINDOW THICKNESS

(Values Determined by X-ray)

Counter Designation	Thickness (in.)
Methane	0.085 ± 0.005
Hydrogen	0.085 ± 0.010
BF_3 #4171	0.10 ± 0.01
BF_3 #4173	0.10 ± 0.01
BF_3 #1110	0.09 ± 0.01
BF_3 #4172	0.11 ± 0.01

The energy dependence of the end-window transmission is calculated with the computer code TAV using this adjusted density, and ENDF/B Version III cross sections for oxygen and aluminum. The calculated transmission is broadened using the overall time resolution of the measurement including the mean charge collection time, the Linac burst width, and the neutron flight-path uncertainty.

Since the end window is in close proximity to the counting gas, the transmission correction tends to be overestimated because of small-angle scattering, commonly called "inscattering" in transmission measurements. This effect and other small corrections associated with scattering effects are described in Appendix A.

Another correction included in the TAV code involves the self-shielding of the counter gas defined as

$$S = \frac{N\sigma}{1 - \exp(-N\sigma)} \quad ,$$

where N and σ are the areal density and total cross section of the gas, respectively. Since the parameters of the counter and the cross sections are well known, this correction can be calculated quite accurately. It reaches a maximum of about 13% at the low end of the methane flux energy region.

The final step in converting the time histories into neutron flux spectra is the division by the hydrogen scattering cross section, which is also accomplished in the code TAV.

The hydrogen and methane flux spectra were compared and normalized in the 13- to 50-keV overlap region of the two spectra. The ratio of the hydrogen to the methane flux shapes is shown in Fig. 27, and the composite flux spectrum from 1 keV to 1000 keV is shown in Fig. 28. In Table 6 the systematic uncertainties in the composite neutron flux spectrum are shown.

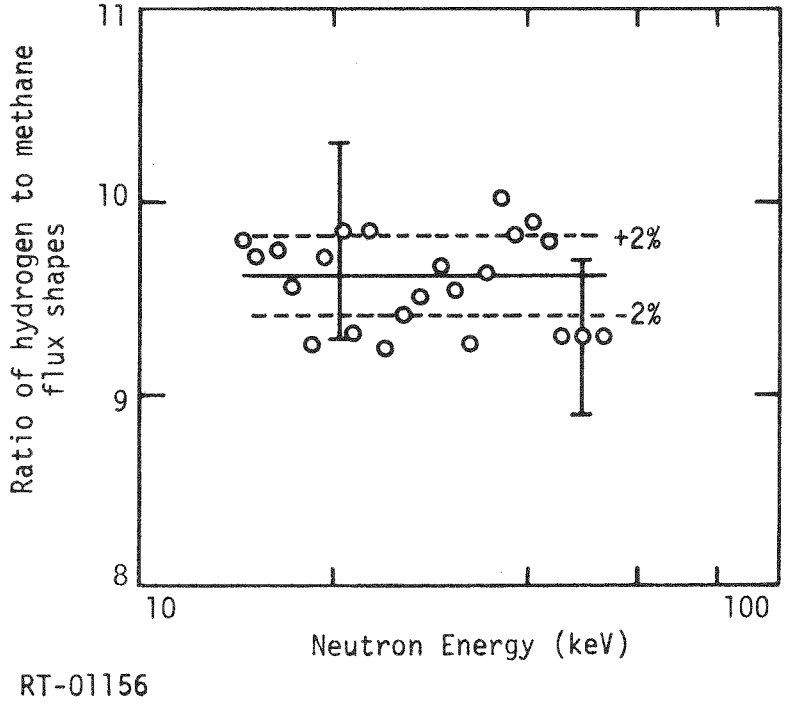

Fig. 27. Ratio of hydrogen to methane flux shapes in the neutron energy region of overlap.

largest self-supporting films reported have been less than one centimeter in area[18] and hence were much too small for the present application.

For these reasons a new method of ion chamber source plate fabrication has been developed. Here, we describe this fabrication process along with other significant construction features of the ion chamber.

The source plate fabrication process is essentially a technique for forming a colloidal dispersion of ^{10}B in a self-supporting plastic film. The colloidal film is formed on commercial plate glass using the apparatus illustrated in Fig. 29. The glass plate is first cleaned thoroughly using a solution of liquid soap in distilled water and, finally, pure acetone. The plate is then wetted with a few drops of liquid soap and polished dry with a paper tissue. This leaves a very thin coating of soap on the glass to serve as a release agent.

A solution consisting of one part Microfilm "A"* and 30 parts acetone is introduced behind the wiper blade and the motor is used to pull the glass slowly past the blade. The motor speed is controlled by a tacometer generator which supplies a voltage to an integrated circuit dc comparator. The comparator opens a relay which slows the motor when the tacometer voltage exceeds a reference voltage. In this way the glass velocity is kept constant with a precision of ±1%. The glass velocity required depends upon the viscosity of the solutions used. In the present case a velocity of approximately 2 cm/sec was used.

After the glass has been coated with a thin (≈ 5 $\mu g/cm^2$) plastic film, it is wiped with two-micron-flake graphite using a cotton swab. The excess graphite is then buffed off using a lambswool buffer. This step leaves the glass coated with a conductive graphite film of ≈ 5 $\mu g/cm^2$, which typically exhibits several MΩ resistance between point contacts.

The glass is now ready to receive the colloidal dispersion of ^{10}B in plastic. The colloidal ^{10}B was obtained in the form of a colloidal dispersion in mineral oil.** A quantity of cyclohexane was added to this mixture and then centrifuged for 24 hours. The supernatant liquid was poured off

*Available from Microdyne Models, Lucadia, California.

**Available from Isotope Sales Division, Oak Ridge National Laboratory.

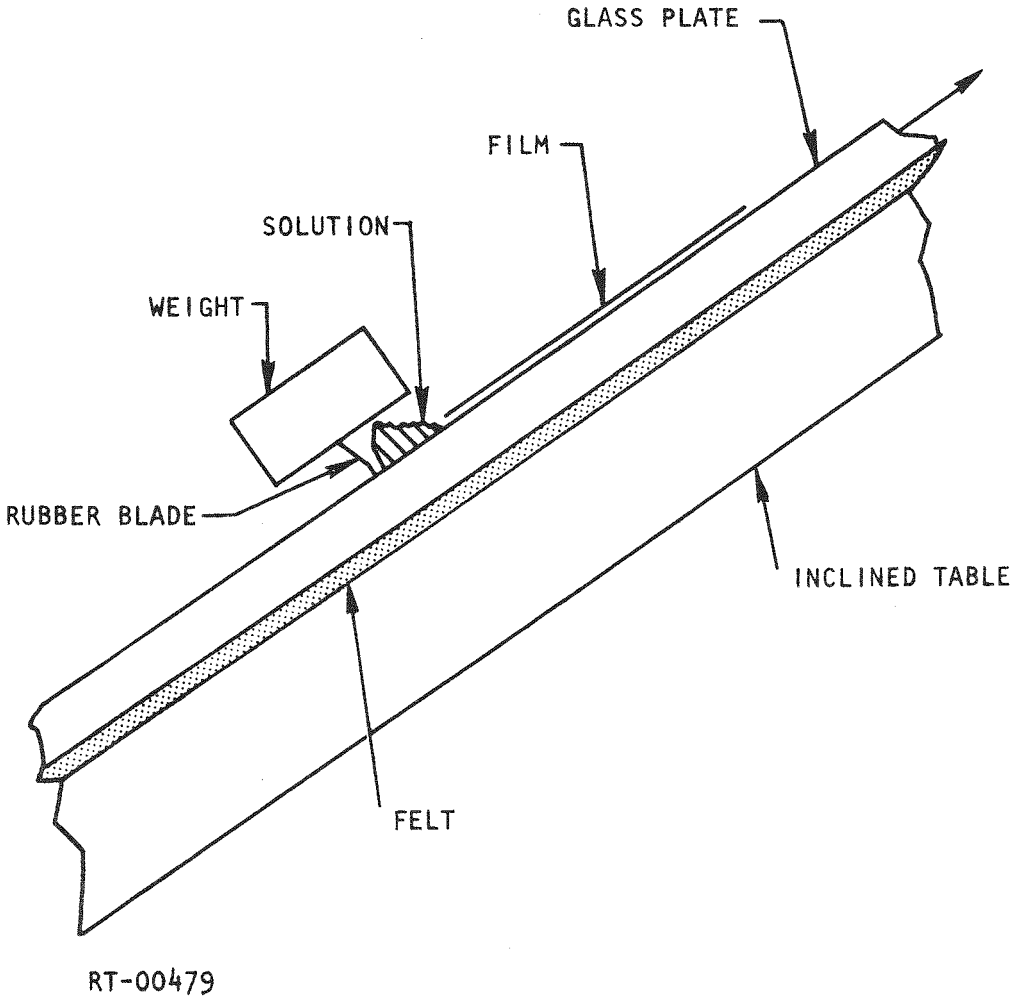

Fig. 29. Apparatus used to form a film on an inclined glass plate.

and the precipitate was dispersed in additional cyclohexane and the process repeated. The final step was a one-minute centrifuging to remove the undesirably large particles. The resultant dispersion of ^{10}B in cyclohexane was combined with sufficient Microdyne "A" plastic to form a solution containing 30% ^{10}B versus 70% plastic in the final film.

This colloidal dispersion is introduced behind the wiper blade after the glass has been returned to the bottom of the ramp. The motor is operated again leaving the boron containing film on top of the graphite.

One of the 10 in. x 10 in. brass frames constructed from 1/4 in. square brass bar is coated with Pliobond* and dried. The glue coating is then wetted with acetone and allowed to dry again until the film is no longer tacky to the touch. This glue-coated surface of the brass frame is pressed firmly on the dried film, and a sharp knife is used to cut the film around the outside edge of the frame.

The glass plate is then installed in the apparatus illustrated in Fig. 30. The motor drive screw slowly pulls one end of the frame from the submerged glass plate with the film attached. When the film is completely free of the glass plate, the motor disengages itself from the screw, and the frame is pulled from the water and the film is allowed to dry.

The viscosity of the solution was adjusted until the films were approximately 200 micrograms per square centimeter in thickness as determined by cutting a film from its frame to allow a direct weighting. The films for the background chamber were made in the same fashion with the exception that the boron was omitted.

A set of thicker films averaging ≈ 400 $\mu g/cm^2$ were made using a variation of the techniques just described. For these films the initial plastic film was much thicker (≈ 200 $\mu g/cm^2$). After the graphite application a dispersion of pure ^{10}B in cyclohexane was coated in the substrate thus formed. Since the boron particles are very small they form an adherent deposit without the use of a binder, and hence the thick films had a much higher boron/plastic ratio than the thin films. The structures of the two types of film are shown in Fig. 31.

*A contact cement available from Goodyear Rubber Company, Akron, Ohio.

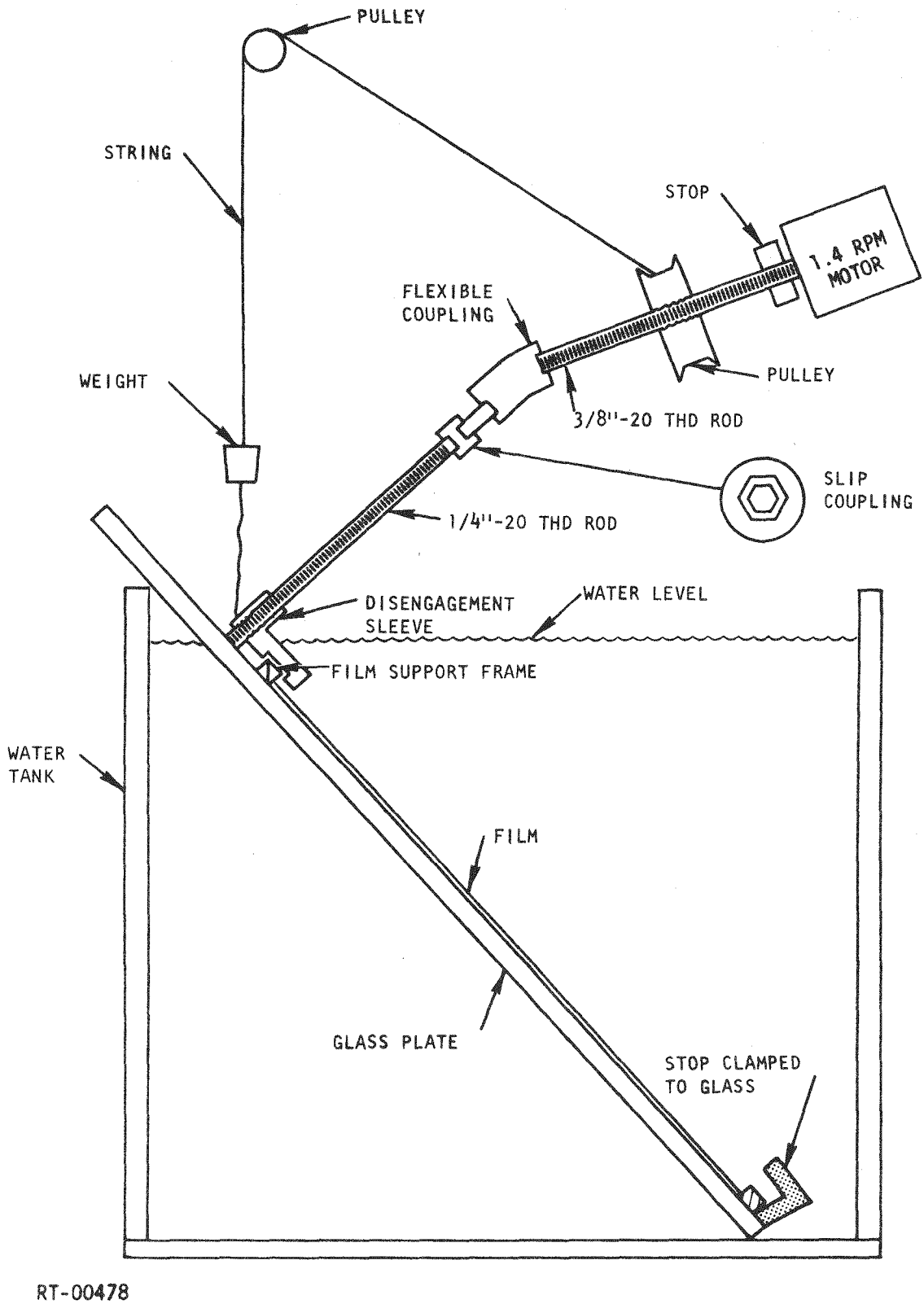

Fig. 30. Apparatus used to remove film from a glass plate under water.

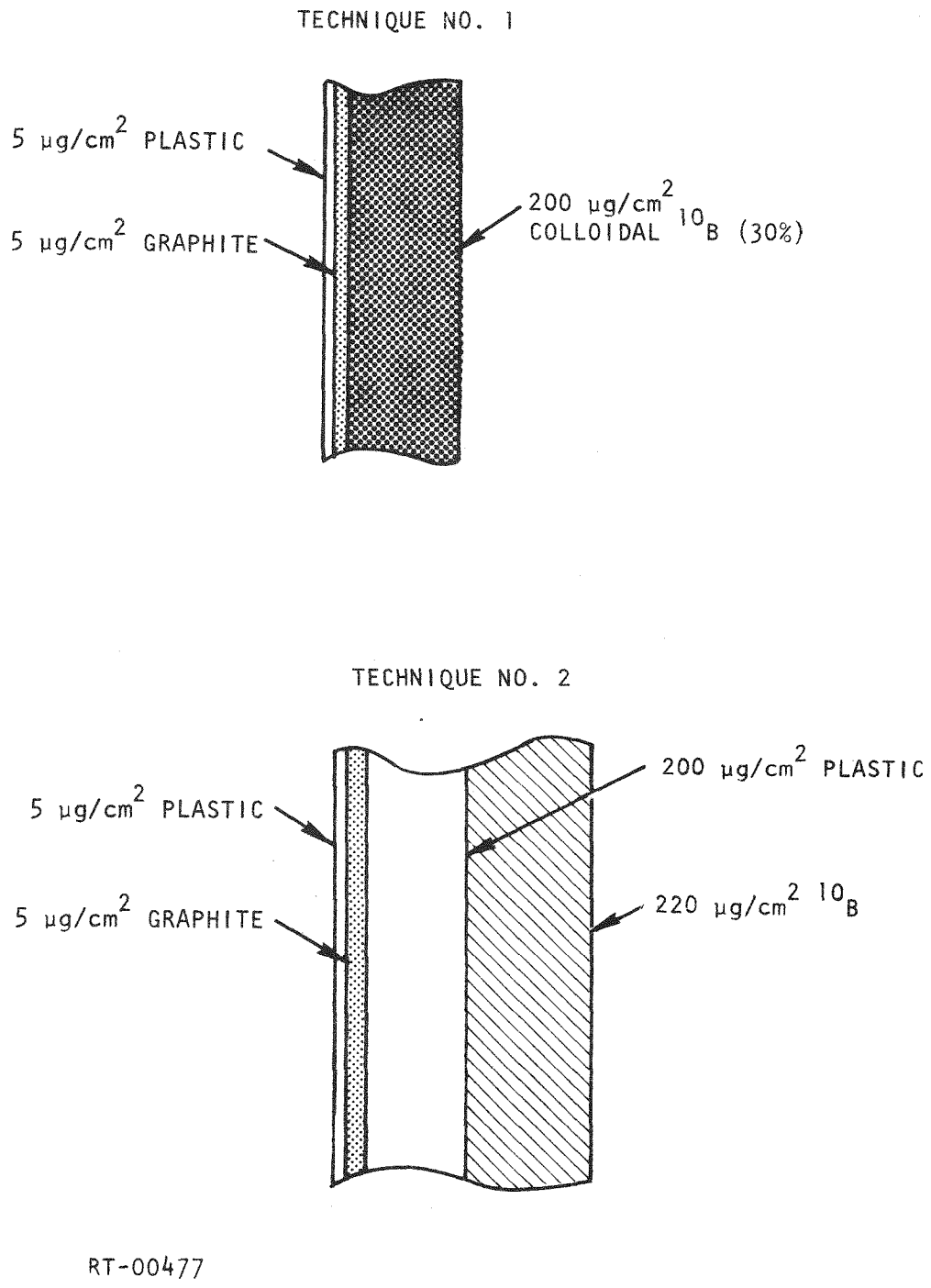

Fig. 31. Structure of two types of film.

The films appeared to be very uniform in thickness, but in order to verify this the alpha particle thickness gauge illustrated in Fig. 32 was constructed. The alpha source was a 200-microcurie ^{252}Cf deposit $\approx$1 cm in diameter evaporated on a platinum backing. The source was mounted on a micrometer screw which allowed the source to be positioned above the film under investigation with a reproducibility of $\approx$0.001 in. The film was positioned on a flat surface below the source and $\approx$1/8 in. above a silicon surface barrier detector. The air-path thickness was adjusted to degrade the 5-MeV ^{252}Cf alpha to $\approx$1 MeV in order to achieve high sensitivity to thickness differences. At this energy the energy loss in the films is equivalent to $\approx$0.050 inches of air, and hence the thickness could be measured with an accuracy of about 3% of the average value.

Very small changes in the air density between the film and the source could cause undesirable drift in the thickness calibration. Therefore, a mercury manometer in the room was used to correct for the small atmospheric pressure changes. The air density change due to temperature was eliminated by placing a thermistor inside the cylindrical light shield surrounding the alpha particle air path. The series voltage drop across the thermistor due to the current flowing through a low temperature coefficient resistor driven by a reference voltage was compared to a second reference voltage using a high-gain comparator. The comparator circuit operated a heat lamp via a relay to cancel small local temperature variations. Usually the temperature drift could be kept to $\approx$0.1°C, which is equivalent to $\approx$0.0007 in. of air under the measurement conditions. The thickness of each film used in both the background and foreground ion chambers was measured at the center and at four locations 3 inches from the center. The results of these measurements are presented in Table 7.

The films were installed in the ion chamber as shown in Fig. 33. Since the thresholds for charged particle-producing reactions are all greater than 1000 keV for aluminum, this material was chosen for the chamber grid wires. The low scattering cross section of aluminum also reduced the magnitude of the transmission correction applied to the Ge(Li) data taken with the ion chamber in the beam.

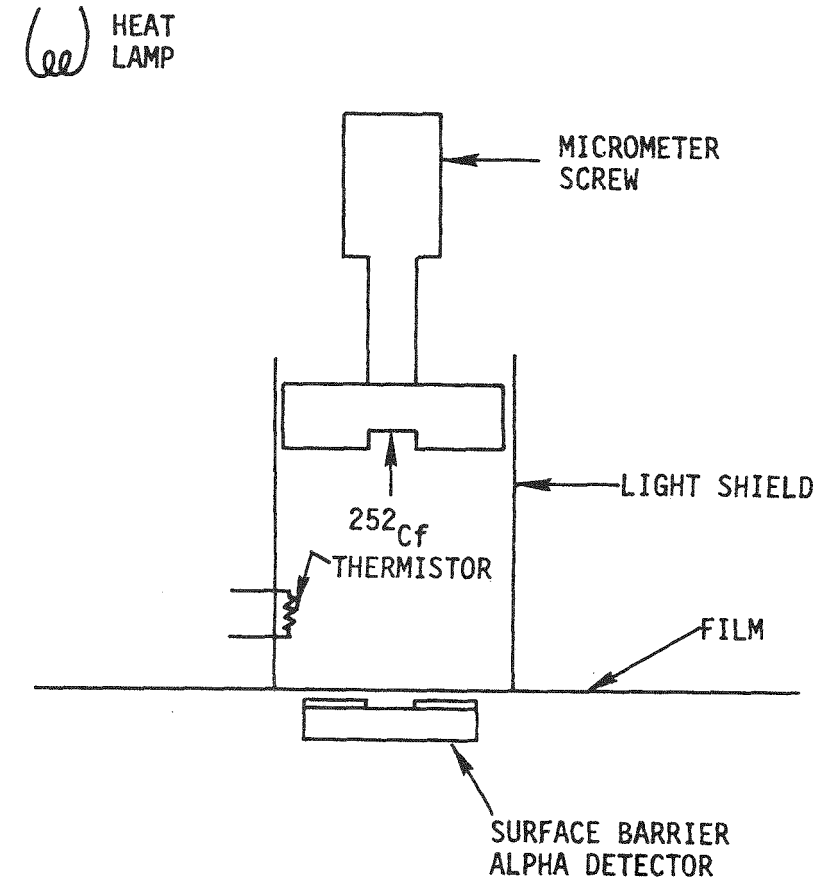

Fig. 32. Alpha particle film thickness gauge.

Table 7

ION CHAMBER FILM THICKNESS MEASURED WITH ALPHA PARTICLE GAUGE

Film Number	Average Thickness (μgram/cm^2 air)	Macroscopic Nonuniformity Mean Deviation (μgram/cm^2 air)	Type[a]	Chamber Location[b]
18	198	16	1	11F[c]
1	217	2	1	---
25	202	12	1	11B[c]
24	209	6	1	---
23	220	5	1	2B
7	204	10	1	3B
21	224	10	1	4B
20	204	10	1	5B
19	183	14	1	8B
22	213	2	1	9B
17	208	6	1	10B
26	15]	7	1	---
15	238	24	1	1B
9	143	60	2	---
10	211	8	2	---
2	229	26	2	---
3	179	25	2	1F
14	216	12	2	2F
13	211	7	2	3F
12	---	---	2	5F
11	206	3	2	4F
27	396	14	3	9F
5	400	10	3	8F
8	393	17	3	7F
4	427	17	3	6F
16	434	24	3	10F

(a) Type: 1 = pure plastic, 2 = thin, and 3 = thick.
(b) Relative location in the chamber counting from accelerator end; B = background ion chamber, and F = foreground ion chamber.
(c) These films have been coated with a ^{236}Pu alpha source.

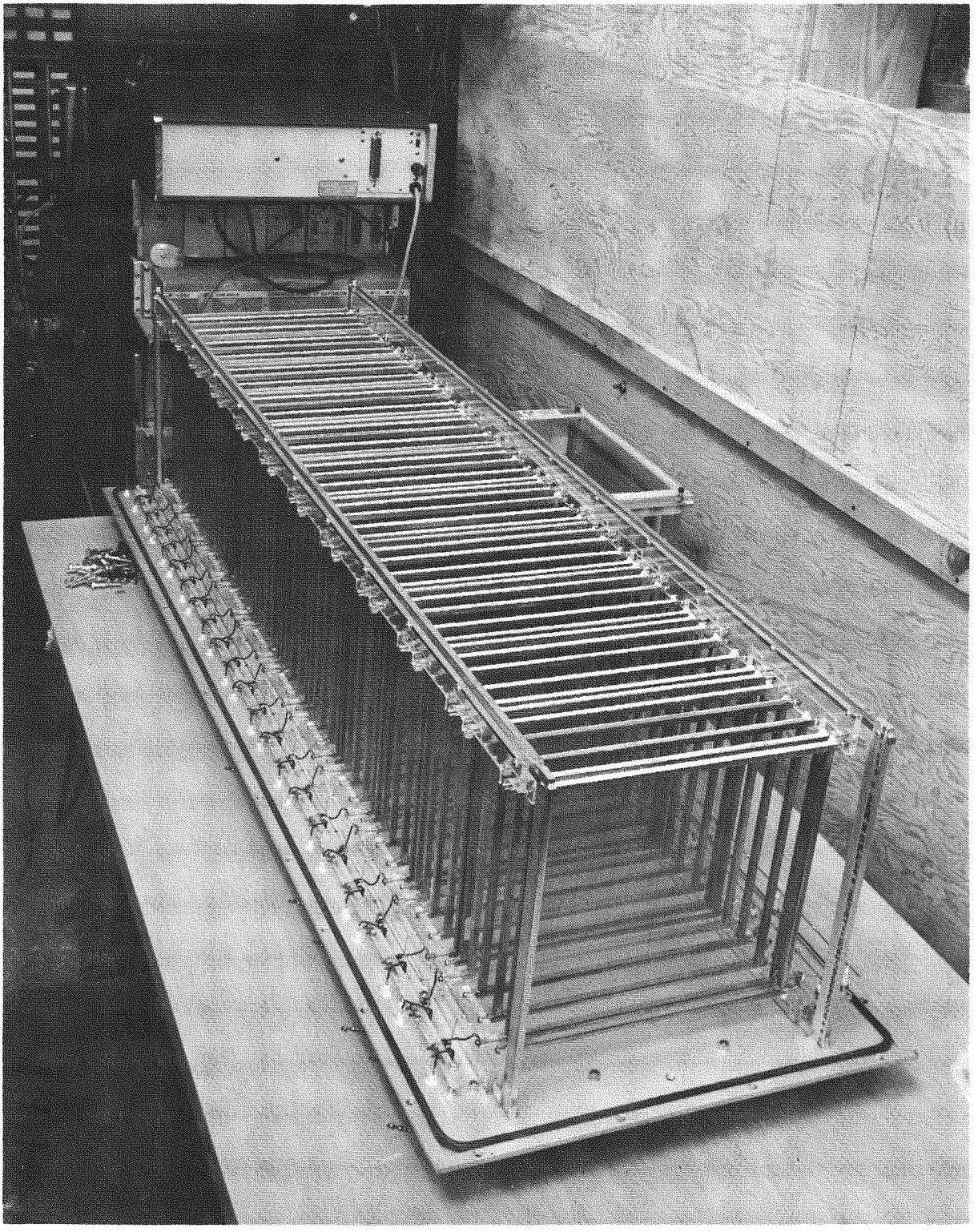

X-90154

Fig. 33. Photograph of ion chamber with cover removed.

A 90% argon and 10% CO_2 gas mixture was chosen for the chamber gas because of its high electron mobility and low cost (which allowed the chambers to be operated in the continuous flow mode). A flow rate of one liter per minute yielded a steady-state pulse height after a $\approx$3 hour stabilization period.

For ^{36}Ar, with a natural abundance of 0.34%, the (n,α) and (n,p) channels are open, but the background chamber measurements verify that these cross sections produce only a very small background below 1 MeV.

Since the chambers were to be operated in the electron collection mode, Frisch grids were used to eliminate the dependence of the pulse amplitude on the charged particle track orientation. Since the maximum range of the alpha reaction product at 1000 keV incident neutron energy is <2 cm in argon at atmospheric pressure, this dimension was chosen for the distance between the film and the Frisch grid. This dimension was also used between the Frisch grid and the collecting element. A grid was also used for the collecting element because of the very low average density which could be achieved.

A spacing of 0.047 in. was chosen between the No. 37 (0.0035 in. diameter) aluminum wire elements. This configuration has a 1% grid shielding defect at 2 cm spacing, and hence a suppressor grid was installed between adjacent collector grids to prevent cross talk between the upstream and downstream data channels. These suppressor grids were maintained at a small negative potential to repel electrons passing through the collector grid, and they were capacitively bypassed to ground.

The grid structure was formed by attaching plastic foam strips to the outer surfaces of the 10 in. x 10 in. brass frames. The wire was wound over the foam plastic strips, which served to maintain tension on the wire. After being cemented to the brass frame on one side, the wire was cut out on the cemented side to leave wire on only one side of the frame.

The foreground and background ion chambers were designed to hold a maximum of 11 films each. One film in each chamber was coated with a small quantity of ^{236}Pu in order to serve as an alpha calibration source. The remaining spaces in the foreground chamber were filled with five thin and five thick boron-containing films, and the background chamber contained

Table 8

RESULTS OF ACTIVATION ANALYSIS OF ION CHAMBER FILM IMPURITIES

Element	Parts/Million	
	Film Containing 30% Boron	Boron Only
Aℓ	262	16
V	34	4
Mn	118	8
Cℓ	677	23
W	29	1
Cu	4300	290
As	43	13
Na	528	10
K	1390	51

eight pure plastic films. The impurities in the film constituents were measured by activation analysis and are listed in Table 8.

Each chamber element is supported at each of the four corners by Plexiglas strips. All of the film frames, Frisch grids, and suppressor grids were supported on a set of four of these strips, and all the collector grids were supported on the other four. This precaution was taken to eliminate noise due to insulator surface leakage currents to the collector.

5.2 ION-CHAMBER OPERATION

The ion-chamber film frames were operated at -2700 V, and the Frisch grids were supplied with two-thirds of this potential through a 15-MΩ voltage divider capacitively bypassed to ground. This provides a field ratio of 2:1 and ensures a minimum loss of electrons to the grid. The suppressor grids were operated at 1/15 the supply voltage. The collector grids were at ground potential, and each one could be switched from an individual BNC connector to a common signal bus via a microswitch operated by a nylon screw from outside the chamber. All of the collectors on the upstream side of the films shared one of the two signal buses, and all of the downstream collectors shared the other. Each bus was connected to an ORTEC 125 preamplifier. Since each collector exhibits approximately 80 pf of capacitance, the noise

slope of the preamplifier is an extremely important parameter in the ion chamber performance, especially when several collectors are operated in parallel. The preamplifier chosen has a nominal noise slope of 17 eV/pf, which represents the present state of the art.

The shaping time constant of the main amplifier is also important in noise performance, the longer time constants usually resulting in a lower noise level. The time constant is limited by the need for resonably fast recovery from the accelerator bremsstrahlung burst and by timing uncertainties due to the effect of noise on the zero-cross-over point. A shaping time constant of 2 μsec was chosen for these measurements which allowed bremsstrahlung burst recovery within 12 μsec which, when combined with the 5-μsec dead time of the discriminator, resulted in an upper limit of approximately 800 keV at the 226.74-meter flight path.

To further improve the timing resolution the signals were paralleled into a third shaping amplifier with a 0.5-μsec time constant. The discriminator for this amplifier could not be biased as low as those for the 2-μsec amplifiers, but the timing uncertainties due to amplifier noise were appreciably smaller. The electronic logic was arranged to allow the timing to be determined by the 0.5-μsec amplifier for all pulses above its discriminator threshold.

The timing uncertainty due to electronic noise was measured under operating conditions by imposing a variable amplitude test pulse at the input to the preamplifier which occured at a fixed time after the accelerator burst. In this way the timing uncertainty could be determined as a function of pulse amplitude. An additional timing uncertainty of $\approx$0.2 μsec results from the electron collection time in the chamber.

Due to an electronic difficiency, some of the ion-chamber data were accumulated under conditions which produced a small flight time-dependent gain shift in the amplifiers. This effect was eliminated by using the centroid of the sum pulse-height distribution to correct the data for the change in the biasing efficiency. The sum pulse-height distribution from the ion chamber corresponding to the 1-10 keV neutron energy interval, is shown in Fig. 34.

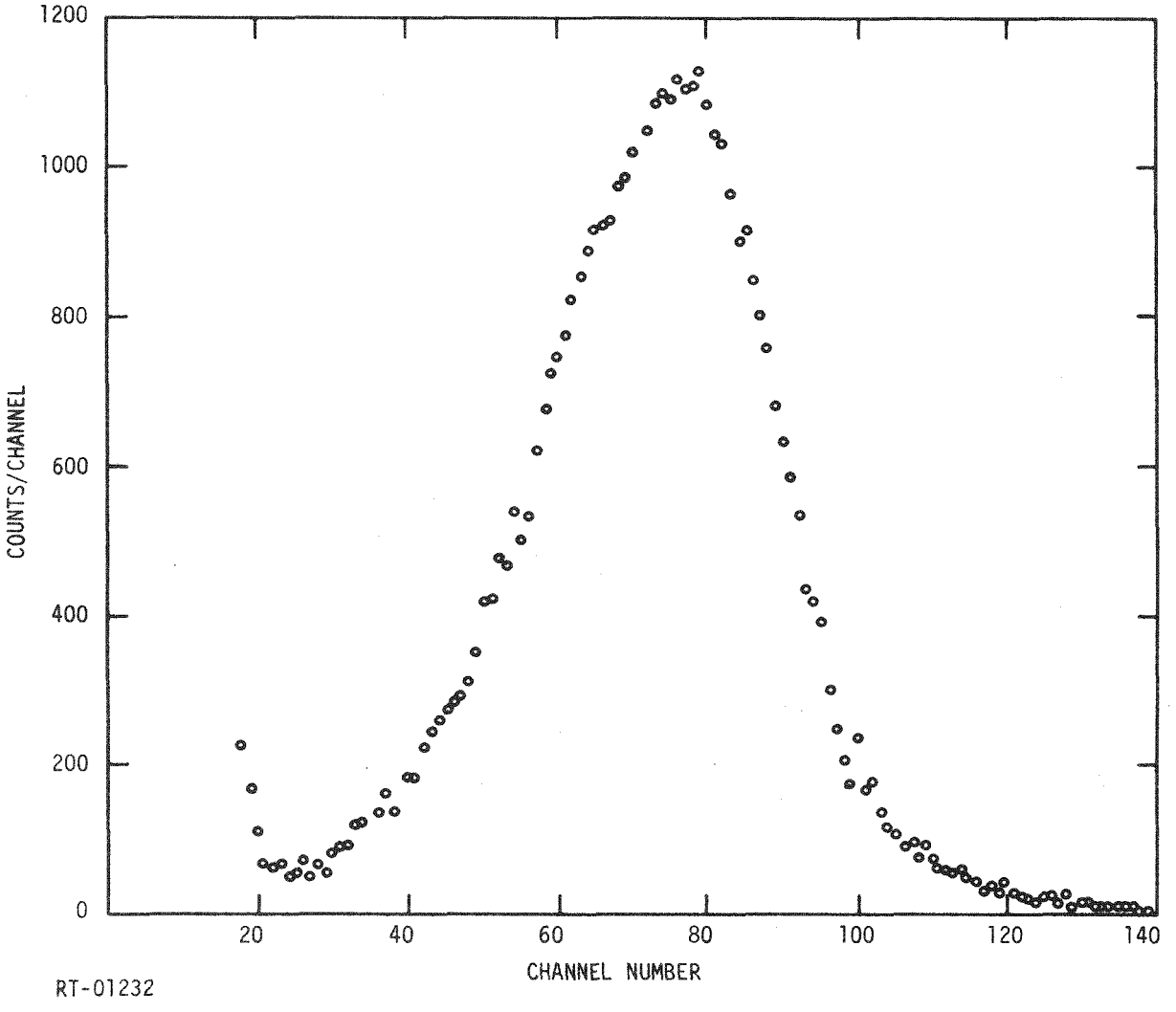

Fig. 34. Ion chamber sum pulse-height distribution (neutron energy = 1 to 10 keV).

The analysis of the ion-chamber data was performed by sorting the multiparameter data with a pulse-height bias dependent on the neutron energy in order to exclude recoil events. In addition, a lower bound was imposed on this bias in order to exclude amplifier noise at low neutron energies.

To calculate the ion-chamber pulse-height distributions, a Monte Carlo computer code ION was written. This code calculates the pulse-height distribution including such effects as the neutron kinetic energy, branching ratio, asymmetric structure of the films and the anisotropy of the reaction products in the center-of-mass system.

The uncertainty in the calculated energy loss of the reaction products in the film materials is the largest uncertainty in the calculation. The computer routine DEDX[19] was used in the energy loss calculations with adjustments to the results at low ion energies to achieve better agreement with published results.

The calculated distributions were in reasonable agreement with measurements, but in view of the uncertainty in the calculation it appeared that more reliable results could be obtained by empirical extrapolations of the measured pulse-height distributions to zero pulse height. The biasing corrections obtained in this fashion reached a maximum of 15% at 700 keV.

This page left blank intentionally.

6. BF_3 PROPORTIONAL COUNTER MEASUREMENTS

Four BF_3-filled proportional counters were used in the present work to measure the relative $^{10}B(n,\alpha)$ cross section below 100-keV neutron energy and to determine an absolute value of the cross section near 500 keV. The BF_3 counter is a very useful device for observation of the sum of the $^{10}B(n,\alpha_o)$ + $^{10}B(n,\alpha_1)$ events at neutron energies $\lesssim$100 keV, since a biasing efficiency near unity can be obtained. At higher energies the biasing efficiency is reduced somewhat by the need for a neutron-energy-dependent bias to exclude ^{10}B and fluorine recoil events. An additional difficulty at higher energies is the rather poor timing characteristics of this device. To reduce the time necessary to recover from the intense bremsstrahlung burst, the "bucking" configuration shown in Fig. 35 was used. This configuration permits an approximate cancellation of simultaneous pulses from different counters.

In the present work it is necessary to normalize the cross-section results at low neutron energy to the cross section derived from the total cross section. However, since the present measurements span a very large energy interval, it is of interest to confirm the results of this normalization by an absolute determination of the cross section at a high energy. This was achieved by including a small admixture of methane gas in the four BF_3 proportional counters. This allowed the proton recoils to be observed in the same environment as the ^{10}B events, which yields a measurement of the $^{10}B(n,\alpha)$ cross section relative to the H(n,n) cross section and eliminates the majority of the corrections necessary when these two reactions are observed in separate detectors. The gas composition of these $^{10}BF_3$ counters was determined by mass spectrometry.

Unfortunately, the relatively poor pulse-height resolution characteristic of the BF_3-filled counter produced proton recoil distributions much inferior to those obtained with the methane filled proportional counter. For this reason the uncertainty in the resolution effect on the proton-recoil detection efficiency is the major uncertainty in this absolute cross-section determination.

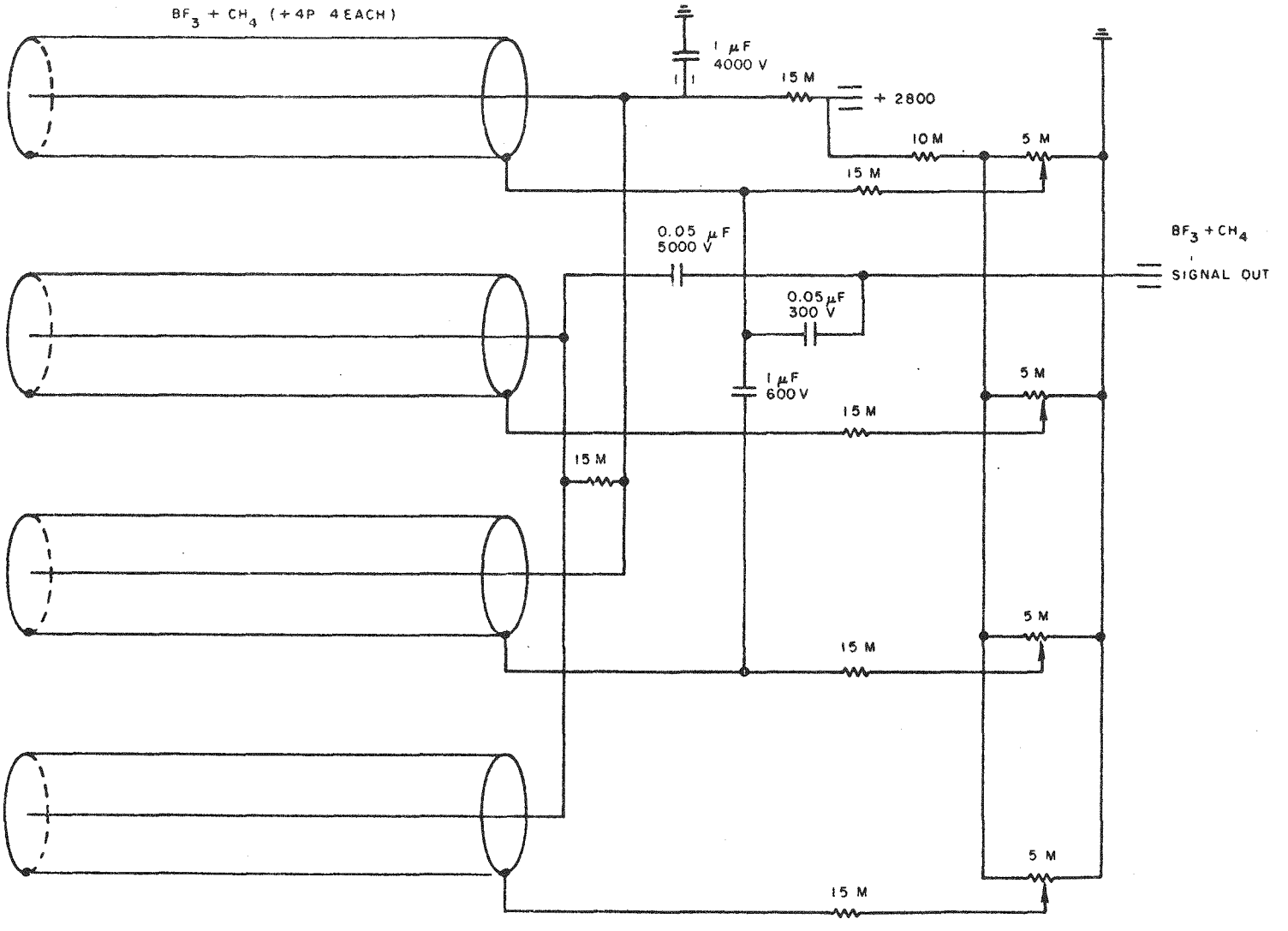

Fig. 35. BF_3 proportional counters in bucking configuration.

The value of the detection efficiency was obtained by using a resolution function derived from the $^{10}B(n,\alpha)$ peak shape. The observed pulse-height distribution for neutrons in the 0.8-3 keV neutron energy region was multiplied by the ground state branching ratio. This distribution was mapped onto a new energy scale which was expanded by the ratio of the ground state to excited state reaction energies and then subtracted from the original distribution. In this way a first-order approximation to the pulse-height distribution for the excited state events was determined. The resolution function was obtained from this difference distribution by using the portion of the distribution on the high-energy side of the peak to form a symmetric distribution. This latter step avoids the effects of wall interactions which distort the low-energy side of the peak. This resolution function was folded into the sum of the fluorine, carbon, boron and proton recoil distributions calculated from the gas composition and scattering cross sections by a computer code, BF3.

The results of this calculation are shown in Fig. 36. The calculation is observed to be in good agreement with the data in the pulse-height region above the F, C, and ^{10}B recoils. The integral bias efficiency, as calculated by the code BF3, was used to determine the fraction of events observed under the biasing conditions imposed during the data sorting. This fraction was 49% at 500 keV neutron energy.

The pulse-height distribution observed from the four counters operated in parallel is shown in Fig. 37 for the 0.8-3 keV neutron energy interval and in Fig. 38 for the 450-550 keV energy interval. The appearance of the recoil events in the low pulse-height regions and the upward shift in the $^{10}B(n,\alpha)$ peak due to the higher energy contribution of the incident neutron are the characteristic differences between the high-energy and low-energy distributions.

The loss of the $^{10}B(n,\alpha)$ events below the energy-dependent bias was calculated from extrapolation of the integral bias curve of the pulse-height distribution after the distribution was adjusted for the kinetic energy contribution of the neutron to the total reaction energy. The integral bias curve for very low-energy neutrons was used as a guide in performing the extrapolation.

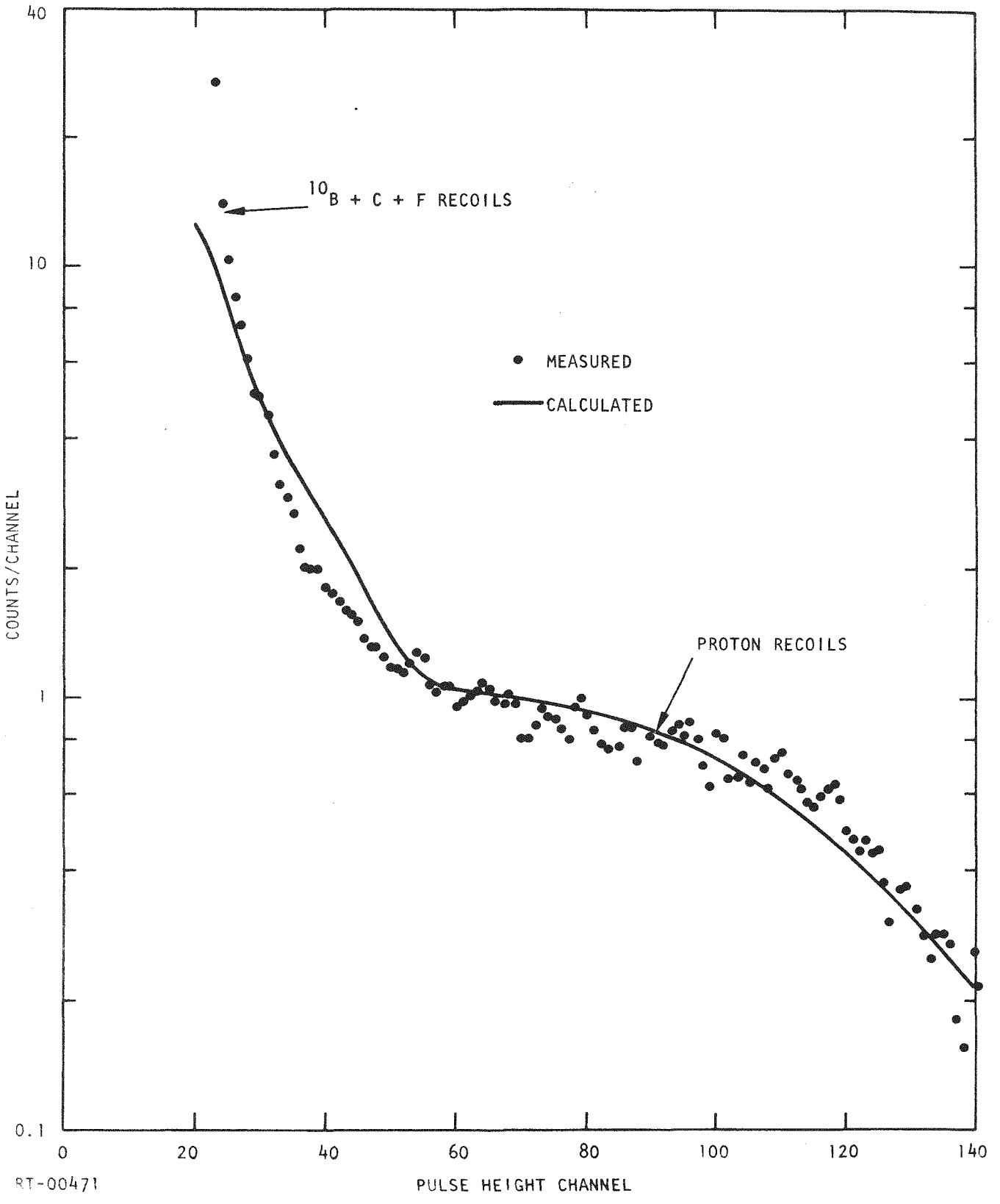

Fig. 36. Calculated vs observed recoil distribution at 500 keV neutron energy in BF_3 proportional counter containing CH_4.

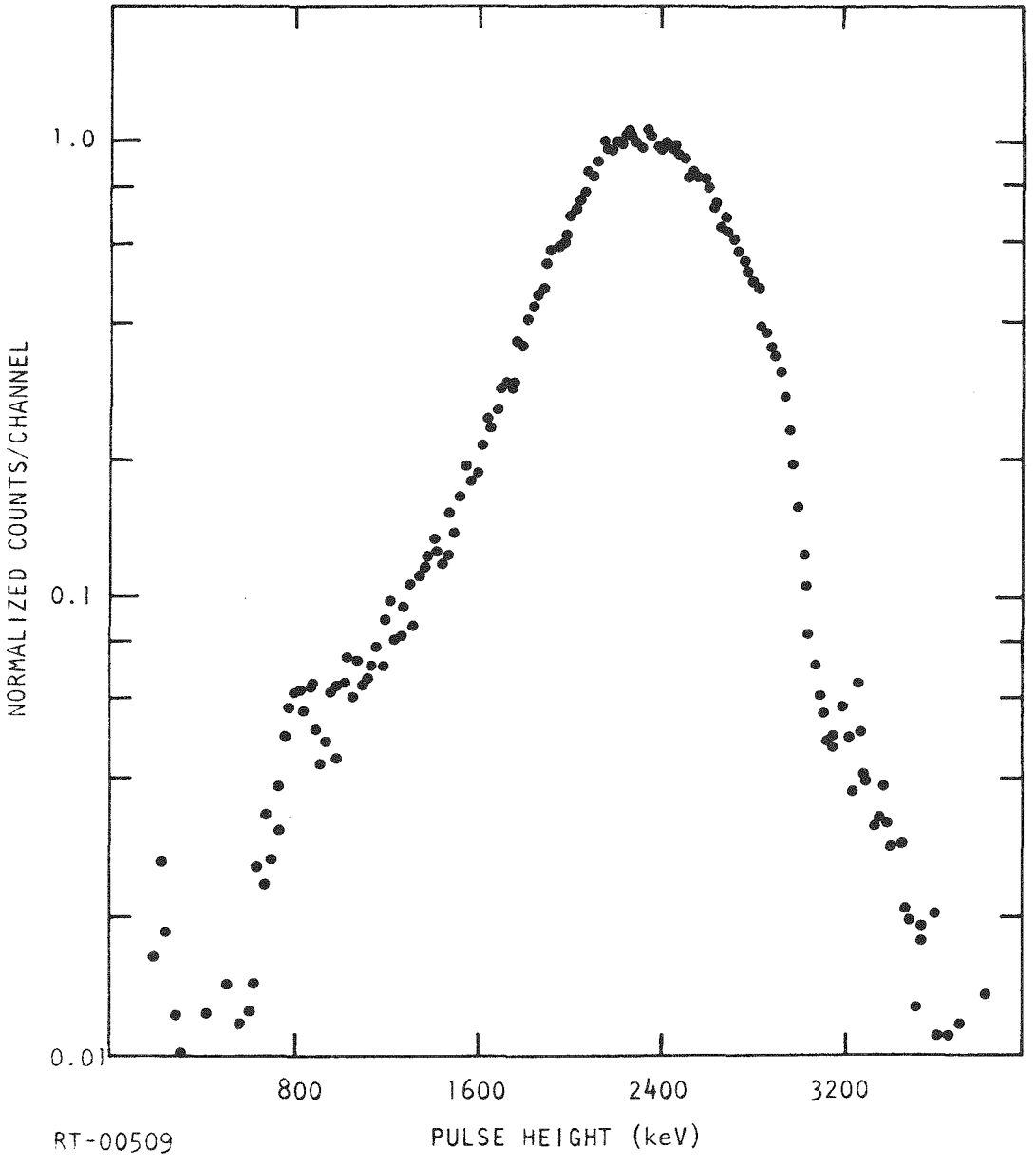

Fig. 37. BF_3 proportional counter pulse height distribution (neutron energy = 0.8 to 3 keV).

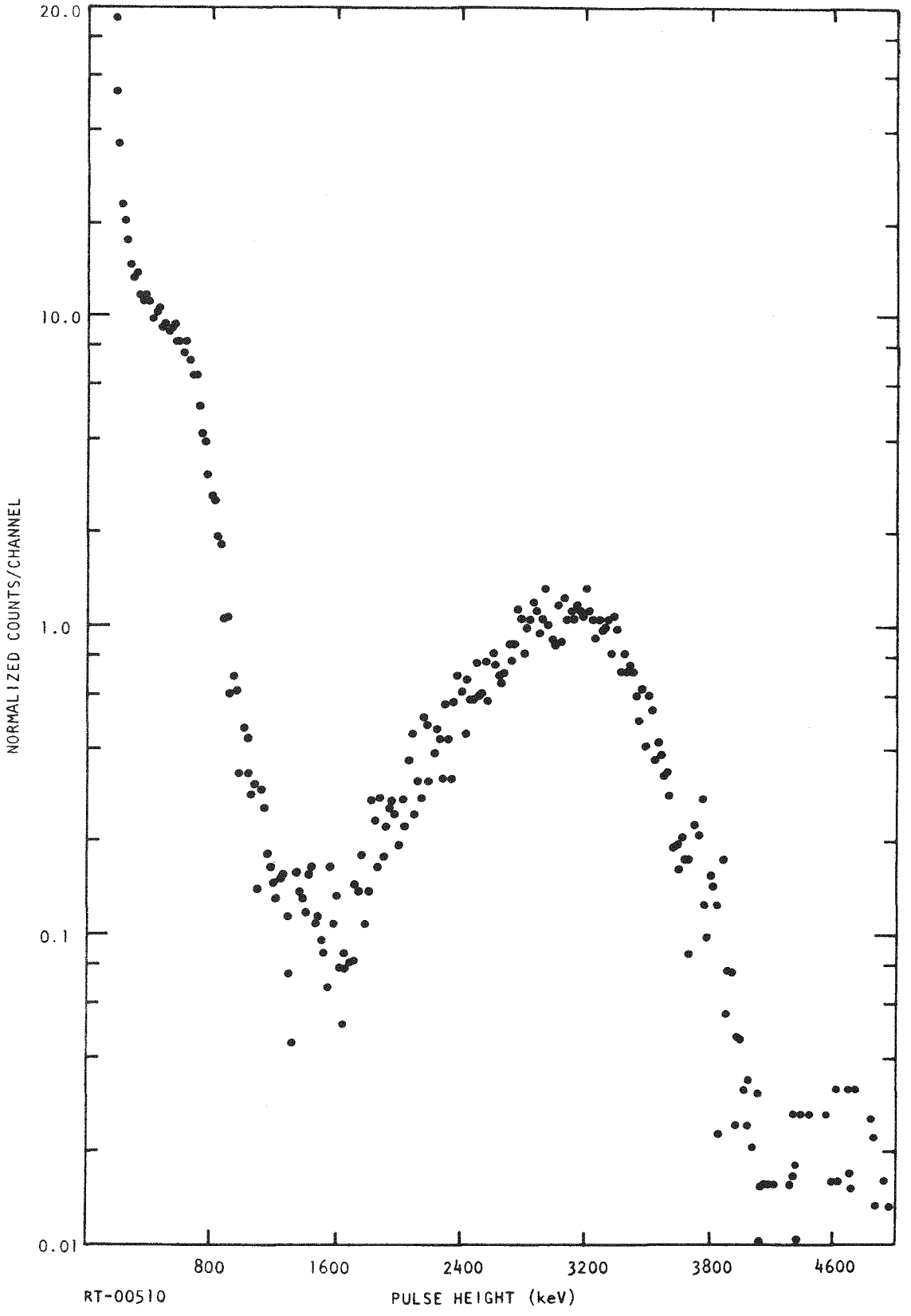

Fig. 38. BF_3 proportional counter pulse height distribution (neutron energy = 450 to 550 keV).

Since the neutron beam traversed an appreciable air path in the vicinity of the detectors, some background contribution from air scattered neutrons can be expected. The neutron energy dependence of this background was measured by moving the BF_3 detectors slightly out of the neutron beam in order to detect scattered neutrons only. This background was normalized to the counting rate in the neutron beam by observing the on-resonance to off-resonance counts at 35 keV with the aluminum filter in place. The background was most important in the 10-50 keV neutron energy region, where it was $\approx$12% of the foreground. A similar procedure was applied to the ion-chamber data. The large self-protection effect in the ^{10}B slab made this background negligible for the $^{10}B(n,\alpha_1\gamma)$ data.

This page left blank intentionally.

7. GAMMA-RAY MEASUREMENTS

7.1 EXPERIMENTAL APPARATUS

The cross section for the $^{10}B(n,\alpha_1\gamma)^7Li$ reaction was determined by measuring the 478-keV gamma ray from the first excited state in ^7Li as a function of neutron energy. The experimental apparatus used was very similar to that developed previously at this laboratory for photon-production cross-section measurements.[20]

An 80-cm^3 Ge(Li) gamma-ray spectrometer was positioned on the centerline of the neutron flight path and was shadow-shielded from source neutrons and gamma rays. The shadow shield consisted of two parts: a 10-cm-thick lead shield positioned ∿1.2 m upstream from the detector and a 30-cm thickness of lithium carbonate in epoxy, followed by 10-cm of lead positioned just upstream of the detector cryostat. The Ge(Li) detector viewed a ring-shaped sample of ^{10}B placed 229.21 m from the neutron source at an average angle of ∿125° with respect to the incident neutron beam. The isotropy[9] of the 478-keV gamma ray allows the angle-integrated cross section to be accurately determined from this measurement at a single angle with rather broad angular resolution.

The ^{10}B sample was constructed using the same technique used for the ^{10}B neutron beam filter and described in Section 2. The ^{10}B powder was held in a uniform layer between thin (∿3 mils) Mylar films glued to an aluminum frame. The dimensions of the aluminum frame which determined the inner and outer diameters (4.25 in. and 9.25 in., respectively) of the ^{10}B ring, were chosen so that the frame was just outside the area intercepted by the neutron beam. This was confirmed by using a gas laser at the neutron source position to cast a shadow image of the collimation system on the ^{10}B ring. The total amount of ^{10}B contained in the sample was determined by difference weighing during assembly. The thickness obtained using

the area of the ring sample was 0.01982 nuclei/barn. The chemical analysis of the ^{10}B sample material obtained from the supplier is listed in Table 9. Small uncertainties in the composition of the sample material have a negligible effect on the cross-section accuracy since the composition enters into the cross-section determination only to second order (in the calculation of finite-sample corrections).

A carbon sample, having a geometry similar to that of the ^{10}B sample, was constructed using graphite powder. This sample was used to measure the small background from neutrons scattering in the sample and interacting with the Ge(Li) detector and surrounding materials.

Figure 3 illustrates the principal components of the experimental apparatus described above. The Ge(Li) detector cryostat is a right-angle, dip-stick type with the detector mounted at the end of the horizontal arm, which minimizes the material around the detector which could contribute to the scattered neutron background. Also shown in the figure are the ^{10}B and C samples and their positioning device and the collimation and shadow shield positioned just upstream from the Ge(Li) detector. The ^{10}B and C samples were mounted at opposite ends of an aluminum bar which could be rotated to accurately position either sample in the neutron beam.

The electronics associated with the Ge(Li) spectrometer were similar to those described previously for photon-production cross-section measurements.[20] A linear gate was used to block the amplified linear signal from the Ge(Li) detector for about a 10-μsec interval during the bremsstrahlung burst, thus successfully eliminating unwanted bremsstrahlung-induced events from the Ge(Li) gamma-ray spectrum. This arrangement allowed the detection of 478-keV gamma rays up to a neutron energy of ∿2 MeV, which corresponds to a flight time of 12.2 μsec.

Two slightly different configurations of the electronics were employed, depending on whether data were accumulated using a one-parameter (fixed-wired time and pulse-height analyzers) or a two-parameter (on-line computer) data acquisition system. In the two-parameter mode, pulse height (gamma-ray energy) and time information (neutron energy) were generated for each gamma ray event in the Ge(Li) detector. These two-parameter data were digitized

Table 9

CHEMICAL ANALYSIS OF BORON USED IN ^{10}B SLAB

Material	Wt %
B (92.28% ^{10}B)	93.6
C	0.52
O	3.30
H_2O	1.3
	Parts/Million
Aℓ	100
Ca	1000
Co	60
Cr	70
Cu	5000
K	1000
Mg	3000
Mn	200
Na	300
S	300
P	40
Rb	3
Sb	10
Si	1000
Sn	40
Sr	3
Ta	60
Ti	40
V	7
W	20
Zn	300

and stored sequentially using a CDC-1700 on-line computer and were sorted off-line at the conclusion of the experiment. For one-parameter operation, the time information was generated for two ranges of pulse heights by routing the Ge(Li) linear signal to two timing single-channel analyzers. During the course of the single-parameter data accumulation, a time-gated pulse-height analyzer was used to record the gamma-ray energy spectrum corresponding to various neutron flight-time intervals. In this way one could monitor any changes in the shape or position of the 478-keV gamma-ray peak with neutron energy, which might require corrections to the single-parameter flight time for events falling outside of the fixed pulse-height window. These spectra indicated that small corrections would be required for neutron energies $\gtrsim$400 keV. However, in practice the corrections were more accurately determined from a sorting of the two-parameter data, as is explained in Section 7.3.

The performance characteristics of the Ge(Li) spectrometer were measured using a ^{7}Be source which decays by electron capture to produce the same 478-keV excited state of ^{7}Li as is produced in the $^{10}B(n,\alpha_1\gamma)$ reaction. The spectrometer exhibited a gamma-ray energy resolution of 3.5 keV (fwhm) for the 478-keV gamma ray from ^{7}Be. The 478-keV gamma-ray peak from the $^{10}B(n,\alpha_1\gamma)$ reaction had a line width of $\sim$11 keV (fwhm), which is in excellent agreement with the calculated line width resulting from Doppler broadening due to the motion of the ^{7}Li* nucleus. The primary effect of the incident neutron kinetic energy for our geometry was calculated and experimentally verified to be a downward shift in the peak centroid by $\approx$1 keV for 1-MeV neutrons. Such small peak shifts should introduce negligible errors into the single-parameter time-of-flight data determined for a fixed pulse-height window encompassing the 478-keV peak. The one-parameter data corrections required for neutron energies above 400 keV were a result of a small, but significant, broadening of the wings of the 478-keV peak at short times after the Linac burst caused by small gain transients induced in the amplifier by the bremsstrahlung burst.

The excellent gamma-ray energy resolution of the Ge(Li) detector used in the present measurement eliminated many of the background uncertainties

inherent in all previous measurements using NaI detectors which have about an order of magnitude poorer energy resolution. For instance, Nellis[9] describes rather elaborate background subtraction techniques required to determine the contribution of 511-keV annihilation photons to the 478-keV gamma-ray peak in a NaI measurement of the $^{10}B(n,\alpha_1)^7Li^*$ cross section. In our Ge(Li) measurements the 478-keV line is completely resolved from the 511-keV line and all other background lines, and the 478-keV peak area may be determined directly with high accuracy.

7.2 MEASUREMENTS PERFORMED

The Ge(Li) spectrometer data were accumulated in two configurations using the one- and two-parameter data acquisition systems. The one-parameter mode was used to accumulate Ge(Li) data simultaneously with ion-chamber data, thus making more efficient use of available Linac running time. Since the ion-chamber measurements required the use of an on-line computer, it was not possible to accumulate the Ge(Li) data in a two-parameter mode. However, supplementary Ge(Li) data were accumulated in a two-parameter mode using the on-line computer in a separate Linac run made to check the reproducibility of the data, and to provide more detailed correction factors for the one-parameter data.

In the one-parameter measurement, the foreground ion chamber, which has a high transmission for neutrons above 1 keV, was in the neutron beam just upstream of the Ge(Li) detector setup. Two TMC time analyzers with 1-μsec channel widths were used to accumulate time-of-flight (TOF) data from two window discriminators of the same width; one set on and the other set just above the 478-keV gamma-ray peak. The off-peak window TOF data were used as a measure of the background (from the Compton distributions of higher energy gamma rays) which lies under the 478-keV peak. Similar measurements were made with the carbon sample to determine the time-dependent background for the 478-keV peak due to neutrons scattered into the detector and surrounding materials. This background was less than 2% of the foreground. The counting statistics in the background-corrected Ge(Li) data ranged from 0.09% at 5 keV to ∿1.6% at 1000 keV for a ΔE/E grouping of 10%.

$^{10}B(n,\alpha_1\gamma)$ data were also accumulated with a 3-in.-thick aluminum filter in the neutron beam. The number of counts in the TOF spectra at neutron energies corresponding to strong aluminum resonances were quite small and entirely accounted for by the ambient background and the very small time-dependent background. The stability of the pulse-height windows was verified periodically throughout the measurements.

The two-parameter data were accumulated in about one-half the running time used for the one-parameter data. For this measurement, the ion-chamber was removed from the neutron beam since the entire run was devoted to only Ge(Li) data accumulation. The two-parameter data (gamma-ray energy versus neutron TOF) were stored sequentially on five magnetic tapes. The pulse-height data were digitized into 2048 channels, and the TOF data were accumulated with an 80-nsec channel width.

A short run was carried out using the carbon sample; however, as is explained in the next subsection, the method chosen to subtract the background from the two-parameter data obviated the need for these carbon data.

Typical Linac operating parameters for both the one- and two-parameter measurements were as follows:

Electron Energy = 80 MeV
Peak Current = 5 amps
Repetition Rate = 180 pps
Burst Width = 100 nsec .

7.3 DATA REDUCTION

The one-parameter TOF data for the 478-keV peak (obtained from the difference between the foreground "on-peak" and "off-peak" spectra) were corrected for the small time-dependent background (<2%) by subtracting the normalized carbon TOF data (obtained as the difference of the carbon "on-peak" and "off-peak" spectra) from these data. The one-parameter data were corrected for 478-keV gamma-ray events which fell outside of the fixed peak window using an energy-dependent factor obtained from the two-parameter data. (The method of obtaining these correction factors is discussed below,

along with the two-parameter data reduction.) The correction factor is quite small except at the highest neutron energies (e.g. <2% for E_n < 500 keV and <10% for E_n < 1000 keV). Corrections were also made to the one-parameter data for the neutron flux attenuation produced by the ion chamber and the additional air path (133 cm) present between the flux detector and the ^{10}B sample. Typical corrections were ~8% at 5 keV and ~4% at 1 MeV.

The two-parameter data were sorted off-line into pulse-height and TOF spectra using the CDC-1700 computer. Two typical pulse-height spectra obtained from sorting a portion of the two-parameter data are given in Figs. 39 and 40, which show results for $5 \leq E_n \leq 15$ keV and $800 \leq E_n < 1001$ keV, respectively. These spectra illustrate the excellent peak-to-background ratio obtained for the 478-keV peak with the Ge(Li) detector. The two principal background gamma-ray lines at 595 keV and 695 keV, from inelastic scattering in ^{74}Ge and ^{72}Ge, respectively, are evident in Fig. 40. TOF spectra were generated for the following pulse-height intervals: (1) an interval completely encompasing the 478-keV peak (wide window), (2) an interval encompassing the 478-keV peak with a window width equal to that used in the one-parameter data acquisition (narrow window), (3) an interval covering the range of pulse heights just below the 478-keV peak, and (4) an interval covering a range of pulse heights just above the peak. Since the carbon background data indicated only a smoothly varying time-dependent background in the vicinity of the 478-keV peak, the foreground TOF spectra (intervals 1 and 2) were corrected by subtracting a TOF spectrum constructed from the mean of the interval 3 and 4 results normalized to correspond to the pulse-height interval of the on-peak TOF spectrum. This procedure is equivalent to subtracting the gamma-ray peak background by assuming a linear function for the background under the peak. Use of a different procedure for subtracting background under the 478-keV peak from the two-parameter data facilitates the detection of possible systematic errors due to background subtraction by a comparison of the one- and two-parameter data sets. The energy-dependent factor used to correct the one-parameter data for events falling outside the fixed peak window was obtained as the ratio of the wide-window data to the narrow-window data (both sets of data corrected for the background under the peak).

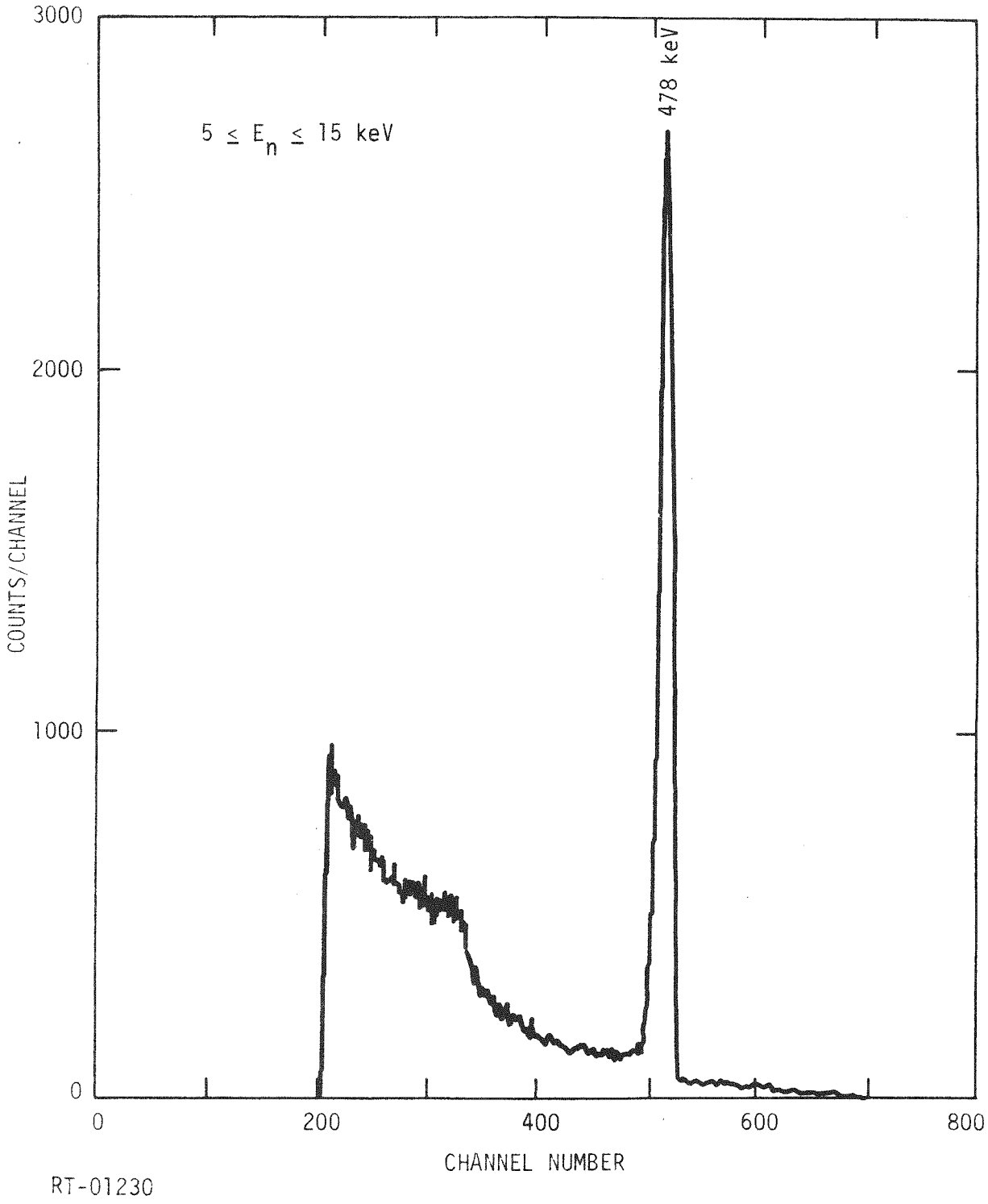

Fig. 39. Ge(Li) pulse-height distribution uncorrected for background (neutron energy = 5 to 15 keV)

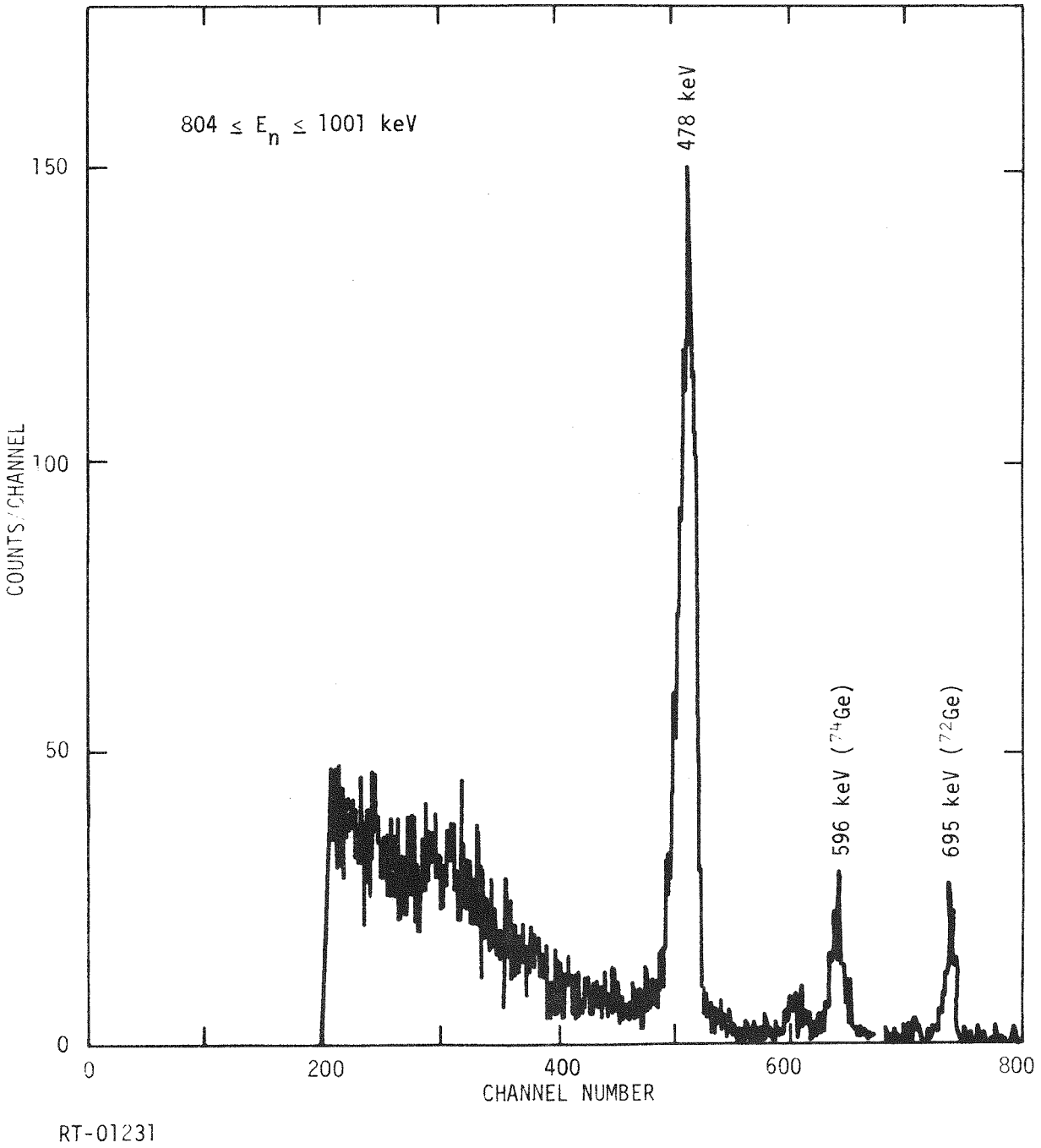

Fig. 40. Ge(Li) pulse-height distribution uncorrected for background (neutron energy = 804 to 1001 keV)

The two-parameter data were corrected for the 278-cm path of air that was present between the flux-detector position and the ^{10}B sample. Typical corrections were 11% at 5 keV and 4% at 1 MeV.

Neutron multiple scattering and attenuation (self shielding) were calculated for the ^{10}B sample using a modified version of the Monte Carlo computer code TACASI.[20] The product of these two corrections has a relatively small effect at the higher neutron energies, increasing to ∿2% at 100 keV and ∿12% at 5 keV.

An estimate was made of the maximum contribution of low-energy neutrons from the preceding burst transmitted through the ^{10}B filter (overlap neutrons) to the counting rate from 1-MeV incident neutrons. This correction, due to overlap neutrons, was calculated to be less than 0.1% and therefore was neglected.

Figure 41 shows the ratio of the one- and two-parameter data and illustrates the good agreement between these two sets of data. Since this comparison was made after all corrections were made to each data set, it not only serves as a check on reproducibility, but helps to identify any systematic errors introduced by the background-subtraction process or by the other corrections applied. Over 65% of the data points shown in Fig. 41 agree within ±2% with the mean of the ratio of the two data sets. Furthermore, there is no evidence of any systematic difference, and the maximum difference for one data point is 8%. Taking into account the counting statistics of the two sets of data and the uncertainties associated with corrections applied, this agreement indicates good reproducibility.

Since the one-parameter data have superior counting statistics and show good agreement with the two-parameter data, the one-parameter data were used along with the composite neutron flux spectrum to determine the $^{10}B(n,\alpha_1)^7Li^*$ cross section.

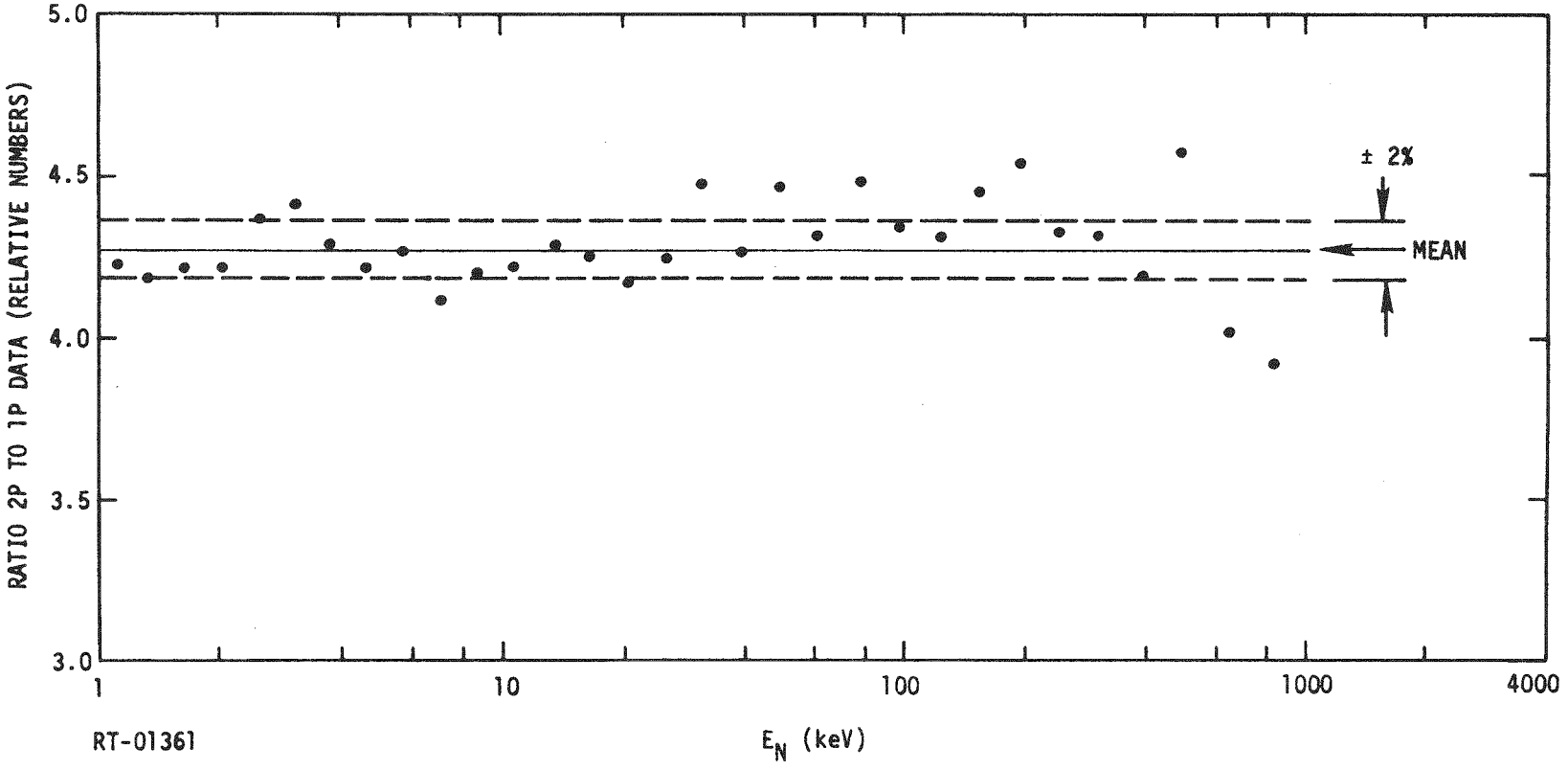

Fig. 41. Ratio of background corrected two-parameter to single-parameter data taken with the Ge(Li) detector.

This page left blank intentionally.

8. DATA ANALYSIS

In this section we mention briefly those aspects of the data analysis common to the various types of detectors.

The majority of the analysis was performed with the multiparameter sorting code "TP". This code uses the channel number from the time digitizer and the flight-path length to calculate the neutron energy corresponding to each event. If the event falls within the neutron energy interval to be analyzed, the polynomial fit parameters are used to calculate the nonlinearity corrected pulse-height channel for each of the three ADCs. If the energy-dependent bias option is being used, the code checks to see if the ADC No. 1 (low gain) channel is below an input minimum chosen to be in the overlap region between the two ADCs. If it is, the decision as to whether the event is to be included in the time-of-flight distribution is made on the basis of the ADC No. 2 channel rather than ADC No. 1, thus preserving good pulse-height channel resolution at low pulse heights.

The time-of-flight data are grouped during the sorting by an integral multiple of the 0.08-μsec channel width of the time analyzer. Usually, the grouping was chosen to result in a channel width equal to about 1/3 of the detector time resolution.

If the dV/dt gamma discrimination is being used, the ratio of ADC No. 3 to ADC No. 1 or No. 2 channel is formed, taking into account the gain ratio of ADC No. 2 vs. ADC No. 1. The event is stored in either a neutron or gamma ray time-of-flight distribution based on an input gamma/neutron discrimination level for this ratio.

The code forms as many as five pulse-height distributions corresponding to arbitrary neutron-energy or time-of-flight channel numbers. Usually, the first pulse-height distribution is devoted to ambient events occurring before the accelerator burst, and the other four are used for pulse-height distributions corresponding to events at various neutron energies. These pulse-height distributions can also be identified as neutron or gamma-ray events.

After the analysis of a file of magnetic tape corresponding to one disk of CDC-1700 data is completed, the code checks to see if the next file is to be added to the current data. If not, the dead-time corrections are calculated using a special time history containing all of the events. These corrections are then applied to both the time-of-flight and pulse-height distributions, after which the output is printed and written on magnetic tape.

Since it is not feasible to correct the pulse-height distribution for the ADC nonlinearity in the sorting code, this operation is performed with the computer code "CH4NM", which also normalizes the data and groups them into an arbitrary energy mesh. The code also subtracts the ambient background pulse-height distribution.

The ambient background and correction to the time-of-flight distribution is performed by a special version of the computer code "COR" which uses the ambient pulse-height distribution from ADC No. 1 and ADC No. 2 to form the integral over the pulse-height region accepted at each neutron energy in the time-of-flight distribution. This integral (scaled by the ratio of the two time intervals) is then subtracted from the time-of-flight channel.

The detector time resolution and the effective mean time at which the accelerator was pulsed are obtained by sorting a preliminary test run taken with each detector in which the time distribution of bremsstrahlung events from the accelerator are observed with a very narrow accelerator burst width. The accelerator current is reduced to the level at which the detector responds to individual gamma rays from the target, and hence an accurate measure of the timing characteristics of the detector is obtained. A correction was applied to the mean time determined to account for the fact that the gamma-ray events produce a time signal delayed on the average by about 1/4 the charge collection time in the detector. The mean time is also corrected for the gamma-ray flight time to arrive at an effective zero time point for the neutron energy scale.

The neutron energy scales of the various data sets were intercompared using plots of the time-of-flight data accumulated with the 3-in. aluminum filter in the neutron beam. All of the data sets indicated excellent agreement with the exception of the BF_3 data, which exhibited a 1.3-μsec time

shift. This error was corrected by adjusting the time scale to force agreement with the other detectors. The 5.906 ± 0.006 keV resonance listed in BNL 325[22] appears at 5.91 ± 0.02 keV in our data.

The contents of the various multiparameter tapes and full records of the experimental conditions are being preserved to enable further analysis of the data should this be warrented at some future date.

This page left blank intentionally.

9. RESULTS AND CONCLUSIONS

The incident neutron flux measurements obtained in the present work are of much higher accuracy than those used in earlier determinations of the $^{10}B(n,\alpha)$ and $^{10}B(n,\alpha_1\gamma)$ cross sections. The total systematic uncertainty is ∿1% from 10 keV to 1 MeV.

The neutron energy dependence of the number of ion pairs (W) produced in hydrogen and methane as a function of the initial proton energy obtained as an adjunct to these measurements are probably the most comprehensive and accurate values thus far obtained. The energy dependence of W is extremely important in proton-recoil neutron spectrometry; however, it seems unlikely that satisfactorily accurate values can be obtained at low energies using neutron techniques alone. This is due to the statistical fluctuation in the number of ion pairs produced and the uncertainty in the Fano factor. A much more fruitful approach would be the injection of intense bursts of monoenergetic protons into the counter gas to obtain a measure of the energy dependence of W which is essentially free of statistical uncertainties.

The high quality of the pulse-height distributions for the hydrogen counter indicate that precision flux measurements to 1-keV neutron energy are feasible. The preamplifier overloading effects which diminished the reliability of the hydrogen proportional counter flux measurements at low energies is in principle easily solved, and since the neutron spectrum of the target assembly can be reproduced, it is anticipated that the cross sections reported here will be improved below 10 keV, and extended below 4 keV, when additional neutron spectrum measurements are made.

The present ionization chamber, BF_3 and Ge(Li) data have been divided by the neutron flux and normalized in the interval from 10-20 keV to the $^{10}B(n,\alpha)$ and $^{10}B(n,\alpha_1\gamma)$ cross sections obtained from ENDF/B Version III and the branching ratio of Irving.[21] With further improvements in the quality of the flux data below 10 keV, these normalizations can be performed at lower energies where the cross section is even closer to 1/V.

The $^{10}B(n,\alpha_1\gamma)$ measurements obtained with the Ge(Li) spectrometer yield a significant improvement in the precision of this cross section. This is largely a result of the excellent signal-to-background ratio provided by the high-resolution Ge(Li) detector combined with the high-efficiency ring-geometry configuration. These advantages also minimized the statistical uncertainties. Although they are small, the backgrounds, such as those due to scattered neutrons, have been carefully assessed.

Our final $^{10}B(n,\alpha_1\gamma)$ cross section is shown in Fig. 42, together with previous data. The error bars shown on the present measurements are a result of a detailed error analysis combining both systematic and statistical uncertainties. The present results introduce direct measurements below 100 keV and high-accuracy data in the 100- to 1000-keV energy range. The present data are seen to disagree significantly with the earlier measurements shown in Fig. 42; however, they are in very good agreement with preliminary measurements of Coates[10] which extend up to ∿250-keV neutron energy. A comparison of the present data with those of Coates is shown in Fig. 43, and the agreement between 10 and 250 keV is seen to be within ∿1-2%. Our $^{10}B(n,\alpha_1\gamma)$ cross sections are listed in Table 10 along with their total statistical uncertainties. The systematic uncertainties for these data are given in Table 11.

The cross sections determined from the ion chamber and the BF_3 detectors are shown in Fig. 44 and disagree systematically above 80 keV by amounts greater than their estimated uncertainties. Although there is no evidence in the pulse-height distributions from either detector to indicate the source of this discrepancy, a possible explanation is that the bremsstrahlung burst effectively deactivates the BF_3 proportional counter in regions outside the rather slowly moving positive ion sheath. Anamolous behavior of BF_3 proportional counters at early flight times has been observed in previous measurements at this laboratory, and it is an effect which deserves further investigation in view of the wide-spread application of this type of detector. The $^{10}B(n,\alpha)$ cross section presently adopted is a composite of the BF_3 data below 60 keV (which have superior counting statistics) and the ion-chamber data at higher energies. These data and their statistical

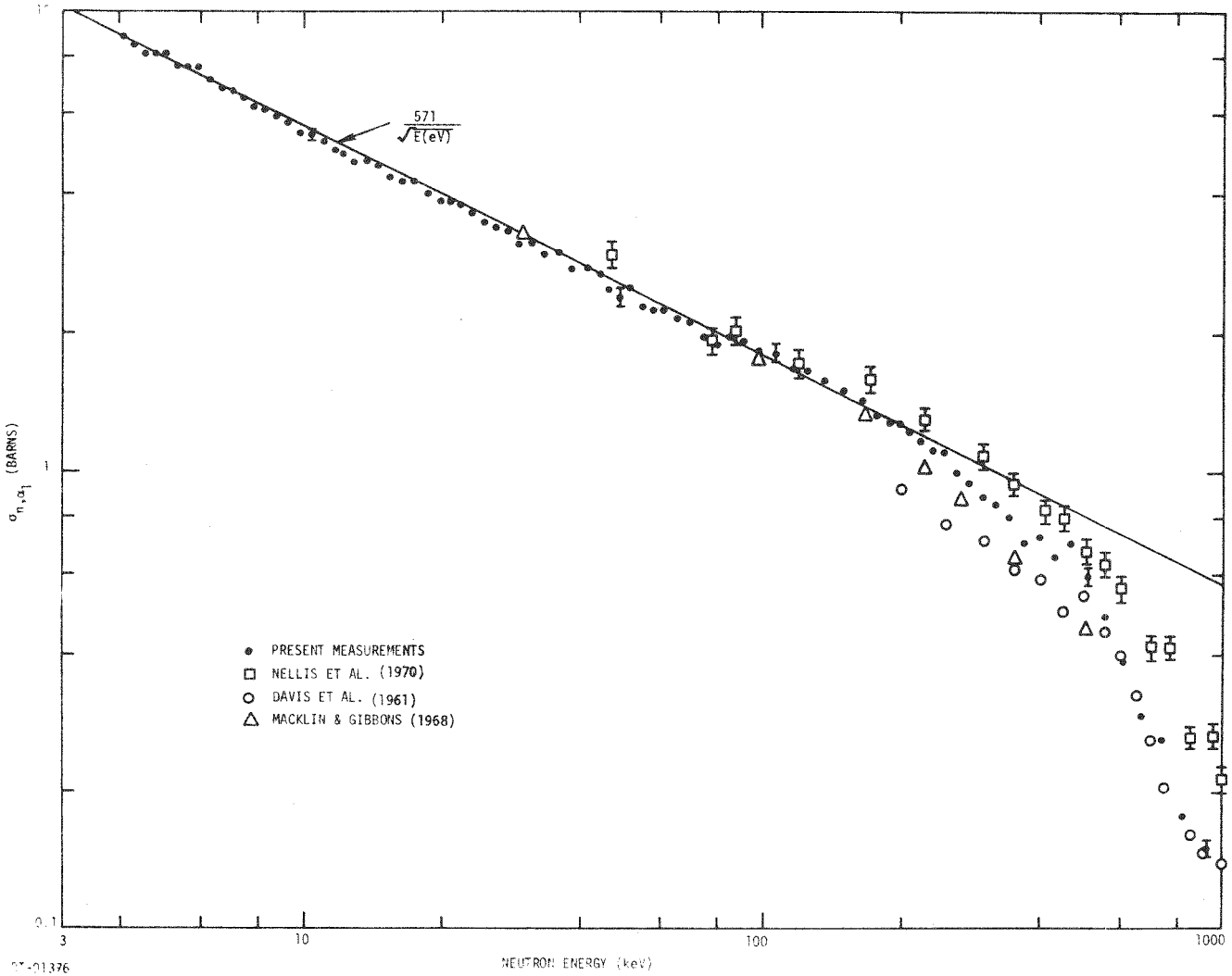

Fig. 42. $^{10}B(n,\alpha_1\gamma)$ cross sections. The present measurements are normalized between 10 and 20 keV using ENDF/B, Version III, values and the branching ratio as evaluated by Irving.[22]

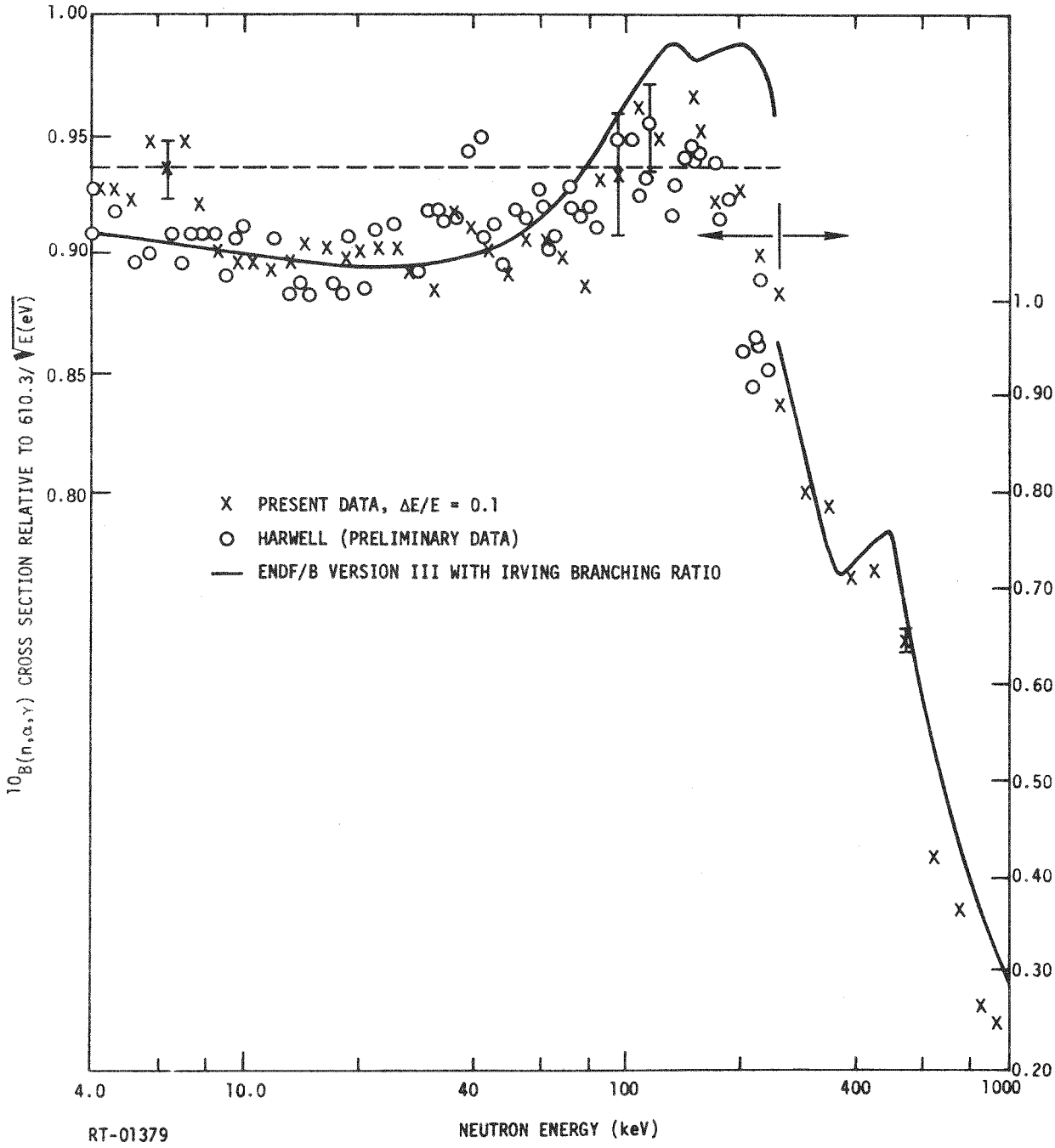

Fig. 43. Comparison of the present $^{10}B(n,\alpha_1\gamma)$ ^{7}Li cross section with preliminary Harwell data and the ENDF/B Version III evaluation using the branching ratio as evaluated by Irving.

Table 10

PRESENT MEASUREMENTS OF THE $^{10}B(n,\alpha_1\gamma)$ CROSS SECTION

E (eV)	σ (barns)	Δσ (barns)	E (eV)	σ (barns)	Δσ (barns)
9.2416+05	1.5129-01	4.8302-03	4.1613+04	2.7691+00	1.2464-01
8.2549+05	1.7707-01	5.0566-03	3.8701+04	2.7400+00	1.1679-01
7.4182+05	2.6049-01	6.9975-03	3.6084+04	2.9806+00	1.3447-01
6.7027+05	2.9362-01	7.2992-03	3.3725+04	2.9433+00	1.3992-01
6.0860+05	3.8509-01	9.6002-03	3.1588+04	3.1168+00	1.3867-01
5.5506+05	4.8647-01	1.2419-02	2.9649+04	3.0959+00	1.4059-01
5.0830+05	5.9322-01	1.5278-02	2.7884+04	3.3072+00	1.5054-01
4.6721+05	7.0003-01	1.8901-02	2.6271+04	3.3949+00	1.5449-01
4.3090+05	6.5174-01	2.0020-02	2.4794+04	3.4662+00	1.5762-01
3.9867+05	7.2271-01	1.9956-02	2.3439+04	3.6118+00	1.6520-01
3.6993+05	7.0310-01	1.9322-02	2.2192+04	3.7828+00	1.8517-01
3.4419+05	8.0202-01	2.2428-02	2.1041+04	3.8194+00	1.7967-01
3.2105+05	8.5641-01	2.5300-02	1.9978+04	3.8331+00	1.8037-01
3.0016+05	8.8152-01	2.6029-02	1.8841+04	3.9823+00	6.8081-02
2.8124+05	9.4804-01	2.9194-02	1.7652+04	4.2706+00	7.4587-02
2.6407+05	1.0015+00	3.0267-02	1.6572+04	4.2543+00	7.4098-02
2.4842+05	1.1124+00	3.0146-02	1.5588+04	4.3452+00	7.2393-02
2.3412+05	1.1173+00	3.0750-02	1.4689+04	4.6120+00	7.7310-02
2.2102+05	1.1715+00	3.2250-02	1.3866+04	4.7113+00	8.1209-02
2.0899+05	1.2238+00	3.4970-02	1.3110+04	4.6661+00	8.2319-02
1.9792+05	1.2806+00	3.7482-02	1.2414+04	4.8739+00	8.6582-02
1.8770+05	1.2841+00	3.8605-02	1.1772+04	4.9822+00	9.0126-02
1.7826+05	1.3350+00	4.0940-02	1.1179+04	5.2115+00	9.6822-02
1.6545+05	1.4310+00	4.4591-02	1.0566+04	5.3773+00	9.7144-02
1.5032+05	1.4992+00	5.0111-02	9.9394+03	5.4030+00	9.2001-02
1.3717+05	1.5788+00	5.4273-02	9.3673+03	5.7197+00	9.8564-02
1.2568+05	1.6516+00	5.7428-02	8.8431+03	5.9245+00	1.0445-01
1.1558+05	1.6574+00	6.0581-02	8.3618+03	6.1008+00	1.0944-01
1.0664+05	1.7959+00	6.0678-02	7.9187+03	6.1536+00	1.1220-01
9.8711+04	1.8296+00	6.5831-02	7.5100+03	6.5019+00	1.2006-01
9.1628+04	1.9327+00	6.9153-02	7.1321+03	6.8645+00	1.3153-01
8.5281+04	1.9615+00	7.4082-02	6.7495+03	6.8271+00	1.2090-01
7.9572+04	1.8836+00	7.2283-02	6.3651+03	7.0630+00	1.2633-01
7.4418+04	1.9527+00	7.8051-02	6.0127+03	7.5743+00	1.3766-01
6.9748+04	2.1212+00	8.5647-02	5.6887+03	7.5913+00	1.4378-01
6.5505+04	2.1628+00	8.8607-02	5.3902+03	7.6149+00	1.4511-01
6.1638+04	2.2406+00	8.3516-02	5.1147+03	8.1237+00	1.4910-01
5.8103+04	2.2447+00	8.7624-02	4.8597+03	8.1034+00	1.5365-01
5.4864+04	2.2812+00	8.9613-02	4.6050+03	8.1277+00	1.5165-01
5.1889+04	2.5090+00	1.0261-01	4.3519+03	8.4671+00	1.5826-01
4.9149+04	2.3912+00	1.0286-01	4.1191+03	8.8650+00	1.7315-01
4.6621+04	2.4836+00	1.0591-01			
4.4282+04	2.6726+00	1.1228-01			

Table 11

Ge(Li) SYSTEMATIC UNCERTAINTIES (%)

E (keV)	Self Shielding and Multiple Scattering[a]	Background[b]	Energy Scale[c]	Flux Attenuation in Air and Ion Chamber[d]	Flux	Total
1000	0.3	0.6	3.3	0.2	1.4	3.7
500	0.4	0.1	1.6	0.3	1.5	2.3
100	0.3	0.1	0.7	0.3	1.7	1.9
50	0.2	0.1	0.3	0.3	1.3	1.4
10	0.1	0.1	0.2	0.4	1.0	1.1
5	0.3	0.1	0.1	0.4	5.2	5.2

[a] Assumes 5% error in multiple scattering and self-shielding correction factors.

[b] Assumes 10% uncertainty in background correction.

[c] Assumes 0.25 channel (0.25 μsec) uncertainty in time analyzer.

[d] Assumes 5% uncertainty in correction applied.

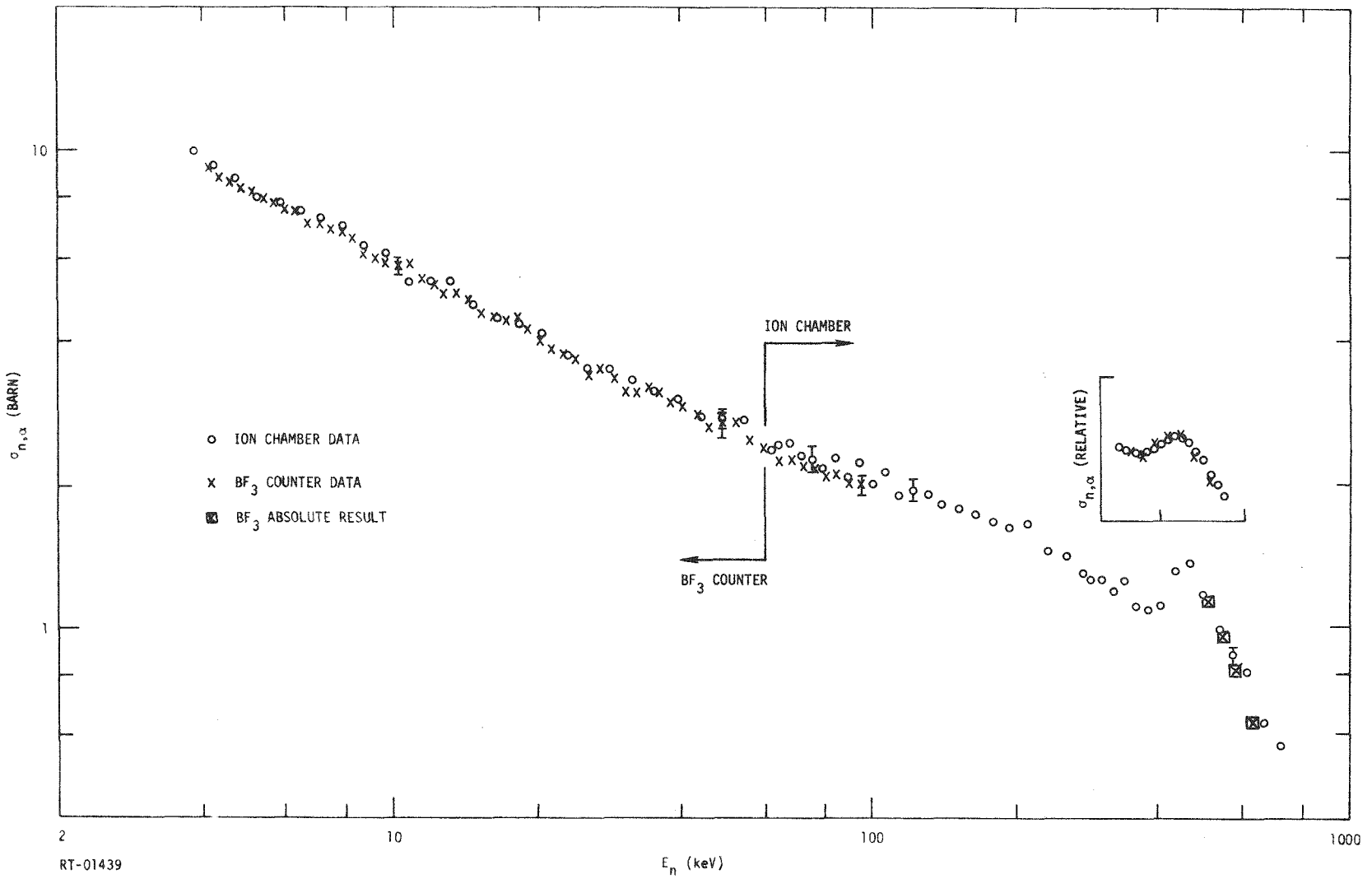

Fig. 44. BF_3 plus ion-chamber data. The absolute results above 500 keV are described in the text. The insert illustrates the result of broadening the ion-chamber cross section data with the BF_3 time resolution function. The broadened results are compared with the BF_3 data in the region near 450-keV neutron energy.

uncertainties are given in Table 12, and Tables 13 and 14 contain the systematic uncertainties.

A comparison is shown in Fig. 44 between the BF_3 results and the ion-chamber data for the structure near 450-keV neutron energy. The time-response function of the BF_3 data was folded into the ion-chamber data so a more meaningful comparison could be made between the two sets of measurements. The agreement between the two data sets is excellent, thus confirming that the structure observed in the higher-resolution ion-chamber data is consistent with that seen in the BF_3 results.

Also shown in Fig. 44 are the absolute cross-section results, which were obtained from the mass spectrographic analysis of the $BF_3 + CH_4$ gas together with the direct comparison of the proton and alpha-particle pulse-height distributions from the proportional counter. Agreement of this determination with the ion-chamber measurements above 500 keV is excellent. The useful energy range of the absolute determination is limited at the high-energy end to ∿650 keV by gamma-flash and time-resolution effects. At the lower neutron energies, the amplifier noise level makes an accurate determination of the proton-recoil energy distribution quite difficult. Principal systematic uncertainties in the absolute values shown in Fig. 44 are an ∿2% uncertainty in the counter gas composition and an ∿3% uncertainty in the detection efficiency. Some additional absolute BF_3 values were obtained for the energy range 200 to 500 keV and show disagreements with the ion-chamber results as large as 10%; however, in this energy range, the effects of amplifier noise and gain shifts make a realistic error estimate very difficult to carry out.

The composite $^{10}B(n,\alpha)$ cross section is shown in Fig. 45, along with earlier measurements and the ENDF/B Version III data. Again, the error bars shown for the present results are the total uncertainties. The present $^{10}B(n,\alpha)$ data which are now considered completely final are those below 100 keV, where, in general, they agree well with earlier results and provide an improvement in the uncertainties in this energy region.

The present $^{10}B(n,\alpha)$ cross-section results above 100 keV, which were obtained with the ion chamber, are substantially higher than the ENDF/B-III data. Our data are in best agreement with the direct measurements of Bogart

Table 12

PRESENT MEASUREMENTS OF THE $^{10}B(n,\alpha)$ CROSS SECTION

E (eV)	σ (barns)	Δσ (barns)	E (eV)	σ (barns)	Δσ (barns)
7.8493+05	5.9024-01	2.1957-02	4.3176+04	2.8329+00	1.3139-01
7.2125+05	5.7116-01	2.0978-02	4.0664+04	2.9419+00	1.2941-01
6.6503+05	6.3833-01	2.4117-02	3.8365+04	3.0041+00	1.3255-01
6.1513+05	8.1891-01	3.0910-02	3.6255+04	3.1562+00	1.4768-01
5.7064+05	8.8858-01	2.9902-02	3.4315+04	3.2054+00	1.5744-01
5.3081+05	1.0028+00	3.2521-02	3.2527+04	3.1231+00	1.4359-01
4.9501+05	1.1971+00	4.0543-02	3.0875+04	3.1654+00	1.4883-01
4.6271+05	1.3938+00	4.7803-02	2.9109+04	3.3541+00	1.5468-01
4.3348+05	1.3403+00	4.9782-02	2.7262+04	3.5171+00	1.6298-01
4.0693+05	1.2301+00	4.5324-02	2.5586+04	3.4076+00	1.5778-01
3.8274+05	1.1114+00	4.0486-02	2.4060+04	3.7095+00	1.7103-01
3.6065+05	1.1299+00	4.1053-02	2.2666+04	3.7883+00	1.7676-01
3.4042+05	1.2827+00	4.7143-02	2.1390+04	3.8754+00	1.8525-01
3.2184+05	1.2215+00	4.7286-02	2.0219+04	4.0253+00	1.9238-01
3.0475+05	1.2810+00	4.9516-02	1.9141+04	4.2739+00	8.2754-02
2.8898+05	1.2817+00	5.1375-02	1.8148+04	4.5082+00	8.9241-02
2.7440+05	1.3111+00	5.2743-02	1.7230+04	4.4655+00	9.0545-02
2.5464+05	1.4418+00	5.0968-02	1.6281+04	4.4999+00	8.6568-02
2.3131+05	1.4760+00	4.9601-02	1.5312+04	4.6233+00	8.5203-02
2.1104+05	1.6724+00	5.6751-02	1.4428+04	4.9134+00	9.1206-02
1.9332+05	1.6497+00	5.9839-02	1.3618+04	5.0908+00	9.6775-02
1.7775+05	1.6941+00	6.4023-02	1.2874+04	5.0294+00	9.7419-02
1.6398+05	1.7703+00	6.9879-02	1.2189+04	5.2763+00	1.0248-01
1.5176+05	1.8139+00	7.4124-02	1.1558+04	5.4240+00	1.0676-01
1.4085+05	1.8584+00	7.9428-02	1.0975+04	5.8597+00	1.1678-01
1.3108+05	1.9499+00	8.2577-02	1.0384+04	5.7373+00	1.1242-01
1.2229+05	1.9974+00	8.9321-02	9.7915+03	5.8514+00	1.0865-01
1.1435+05	1.9389+00	8.2269-02	9.2476+03	6.0233+00	1.1322-01
1.0716+05	2.1628+00	9.3766-02	8.7479+03	6.1312+00	1.1789-01
1.0064+05	2.0289+00	9.7197-02	8.2877+03	6.5935+00	1.2772-01
9.4685+04	2.2572+00	1.0445-01	7.8629+03	6.7696+00	1.3308-01
8.9247+04	2.0924+00	1.0529-01	7.4699+03	6.8792+00	1.3815-01
8.4265+04	2.3306+00	1.1822-01	7.0775+03	7.0764+00	1.4043-01
7.9688+04	2.2062+00	1.1453-01	6.6875+03	7.0858+00	1.3642-01
7.5474+04	2.3020+00	1.2433-01	6.3288+03	7.5143+00	1.4474-01
7.1586+04	2.3415+00	1.2623-01	5.9983+03	7.6006+00	1.5142-01
6.7991+04	2.4990+00	1.3158-01	5.6930+03	7.8692+00	1.5958-01
6.3888+04	2.4720+00	1.1642-01	5.4105+03	8.0874+00	1.6497-01
6.0060+04	2.4067+00	9.5200-02	5.1311+03	8.3305+00	1.6080-01
5.5971+04	2.5004+00	9.9327-02	4.8556+03	8.4728+00	1.6744-01
5.2285+04	2.7289+00	1.1334-01	4.6018+03	8.6764+00	1.7151-01
4.8952+04	2.7074+00	1.1837-01	4.3674+03	8.8979+00	1.7724-01
4.5928+04	2.6670+00	1.1554-01	4.1504+03	9.3036+00	1.9156-01

Table 13

BF_3 SYSTEMATIC UNCERTAINTIES (%)

E (keV)	Room-Return Neutron Background[a]	Spectrum Fraction	Dead Time[b]	Scattering Correction	Flux	Total
500	0.7	2.0	0	2.3	1.5	3.5
100	1.9	0	0.3	2.0	1.7	3.3
50	2.5	0	0.4	1.4	1.3	3.2
10	3.0	0	0.5	1.2	1.0	3.4
5	3.6	0	0.1	1.2	5.2	6.4
2	3.0	0	0.1	1.2	17.1	17.4
1	2.5	0	0.1	1.2	----	----

[a] Assumes a 25% uncertainty in the room-return neutron background.

[b] Assumes a dead-time error of 1% of the correction applied.

Table 14

ION CHAMBER SYSTEMATIC UNCERTAINTIES (%)

E (keV)	Room-Return Neutron Background	Spectrum Fraction	Dead Time	Flux Uncertainty	Total
800	0	2.5	0	1.4	2.9
500	0.3	2.0	0.1	1.5	2.5
100	1.6	1.0	0.6	1.7	2.6
50	1.8	1.0	0.7	1.3	2.5
10	2.9	0	0.7	1.0	3.1
5	2.9	0	0	5.2	6.0
1	2.2	0	0	---	---

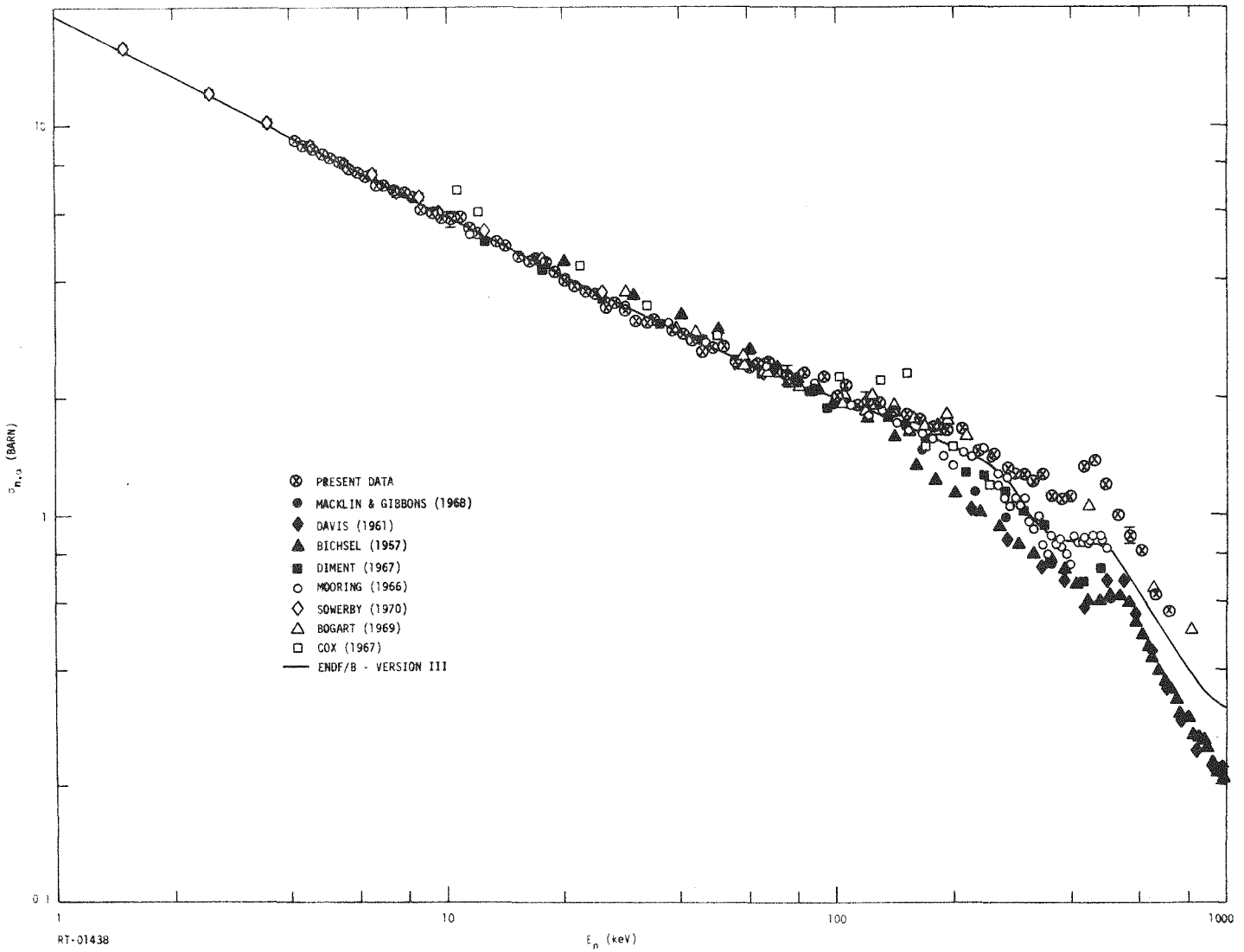

Fig. 45. Comparison of the present measurement of the $^{10}B(n,\alpha)$ cross section with previous measurements

and Nichols.[8] Also, structure in the cross section near 450 keV, which is not well resolved in previous measurements, is clearly defined in the ion-chamber data. This structure is qualitatively similar to that predicted in the (n,α_0) channel by Lane et al.[23] from an R-matrix analysis of elastic scattering, polarization and other reactions proceeding through the compound nucleus ^{11}B.

The ratio of the cross sections $\sigma(n,\alpha_1\gamma)/\sigma(n,\alpha)$ found in the present work is compared in Fig. 46 to that determined from the branching ratio measurements of Macklin and Gibbons[4] and Sowerby[25] and the evaluation of Irving.[22] The present cross-section ratio is substantially lower than the previous results at energies above 100 keV. In their paper, Macklin and Gibbons state: "The $^{10}B(n,\alpha_o)/^{10}B(n,\alpha_1\gamma)$ ratio measurements in the 100-300-keV range are the most difficult part of the present approach. Neutron source strength is low; thermalized neutron effects are important and difficult to measure." We note that, due to the large difference in the $^{10}B(n,\alpha)$ cross section between thermal and a few-hundred-keV neutron energy, a thermal neutron contamination of only $\sim$0.1% in the data of Macklin and Gibbons would be sufficient to account for their discrepancies with the present results [a thermal contamination increases the ratio $\sigma(n,\alpha_1\gamma)/\sigma(n,\alpha)$]. While Sowerby believes that any serious thermal contamination in his experiment could be detected via kinematics, he feels his proportional counter data above 100 keV may not be reliable due to wall effects that have not been treated in detail.[26] Corrections for this should tend to reduce the discrepancies between Sowerby's data and the present results, although one cannot presently say to what extent.

As work progresses in the continuing standard cross-section program at this laboratory, it is expected that the present $^{10}B(n,\alpha)$ results above 100 keV will rapidly be finalized and thereby establish this cross section to an overall uncertainty of $\sim$3% up to 750 keV. In this continuing program, ion-chamber measurements of the $^{6}Li(n,\alpha)T$ reaction will be made, and a number of measurements are planned for this work which should also help to reduce some of the systematic uncertainties in the present $^{10}B(n,\alpha)$ data. For example, determinations of the room-return neutron background are planned

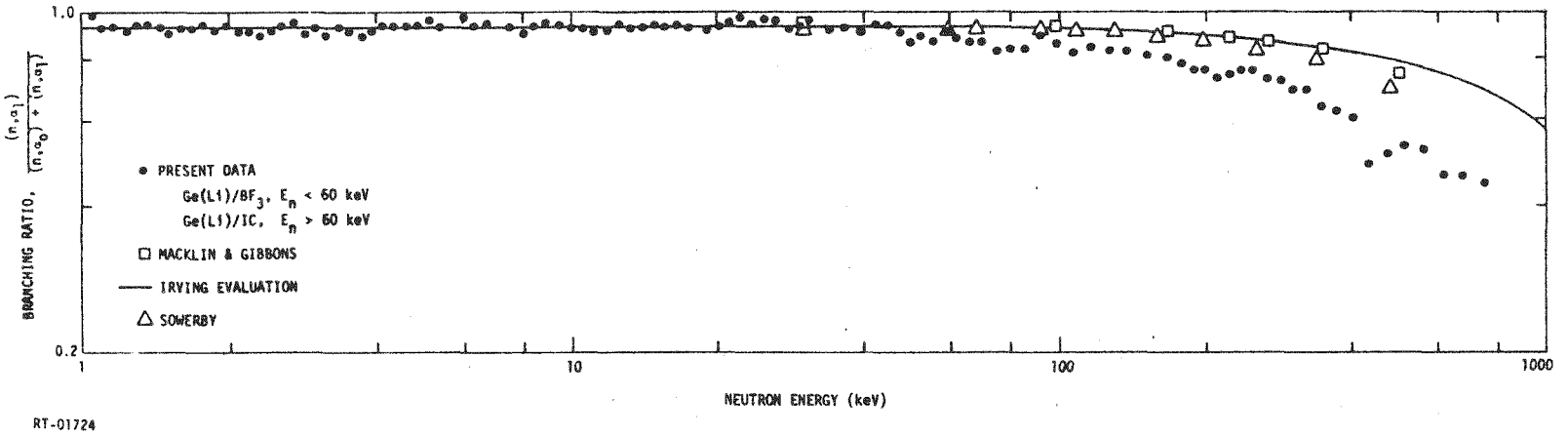

Fig. 46. Branching ratio calculated from present data compared to other determinations.

at various positions in the 230-m building, so that the background at the position of the ionization chamber can be re-evaluated. These measurements can be made more efficiently with a BF_3 counter as a result of the higher counting rate. Since one of these measurements must be made with the counter in the beam, new $^{10}B(n,\alpha)$ cross sections obtained with a BF_3 counter will also be available for comparison with the present data.

In addition to providing verifications of the present $^{10}B(n,\alpha)$ results early in the $^{6}Li(n,\alpha)$ measurement program, this program will eventually provide additional $^{10}B(n,\alpha)$ data over a larger energy region. During the ^{6}Li data runs, films of ^{10}B will be used in the ionization chamber so that direct ^{6}Li-to-^{10}B cross-section ratios can be formed which may be compared with other measurements of this ratio, e.g. with the Harwell data.[5] These ion-chamber measurements will be made with smaller amplifier time constants than were employed for the present data, so that the new $^{10}B(n,\alpha)$ data will be reliable to higher neutron energies.

The neutron flux will be remeasured to lower neutron energies for the ^{6}Li program as a result of slight improvements in the electronics employed. Thus, in addition to the ^{6}Li data, new $^{10}B(n,\alpha)$ cross sections will be obtained which extend to both lower and higher neutron energies than those presently reported.

REFERENCES

1. F. P. Mooring, J. E. Monahan and C. M. Huddleston, Nucl. Phys. 82 (1966) 16.

2. K. M. Diment, "The Average Neutron Total Cross Section of ^{10}B from 100 eV to 10 MeV and Absorption Cross Section up to 500 keV," AERE-R 5224 (1967) and private communication from M. G. Sowerby (1972).

3. S. A. Cox and F. R. Pontet, J. Nucl. Energy 21, (1967) 271.

4. R. L. Macklin and J. H. Gibbons, Phys. Rev. 165 (1968) 1147.

5. M. G. Sowerby, B. H. Patrick, C. A. Uttley and K. M. Diment, J. Nucl. Energy 24 (1970) 323, and private communication from M. G. Sowerby (1972).

6. E. A. Davis, F. Gabbard, T. W. Bonner and R. Bass, Nucl. Phys. 27 (1961) 448.

7. H. Bichsel and T. W. Bonner, Phys. Rev. 108 (1957) 1025.

8. Donald Bogart and Lowell L. Nichols, Nucl. Phys. A125 (1969) 463.

9. Donald O. Nellis, W. E. Tucker and Ira L. Morgan, Phys. Rev. C1 (1970) 847.

10. M. Coates, private communication (1971).

11. J. K. Millard, ORNL-TM-3252, unpublished.

12. U. Fano, Phys. Rev. 72, #1 (1947) 26-29.

13. H. Werle, G. Fieg, H. Senfert and D. Stegemann, Nucl. Instr. & Meth. 72 (1969) 111-119.

14. E. F. Bennet, Nucl. Sci. & Eng. 27 (1967) 16-27.

15. E. F. Bennet, ANS Transactions 13, #1, p. 269.

16. J. W. Rogers, Nucl. Instr. & Meth. 80 (1970) 313-319.

17. A. D. Algarno and G. W. Griffing, Proc. Royal Soc. 248 (1958) 415-427.

18. R. L. Macklin and J. H. Gibbons, Phys. Rev. 165 (1968) 1147-1153.

19. C. F. Williamson, University of Washington Annual Progress Report (1963) pg. 33.

20. V. J. Orphan et al., Nucl. Instr. & Meth. 73 (1969) 1.

21. F. H. Fröhner, "TACASI - A Fortran IV Code for Least Squares Analysis of Neutron Resonance Data," USAEC Report GA-6906, General Atomic Division, General Dynamics Corporation (1966).

22. D. C. Irving, "Evaluation of Neutron Cross Sections for Boron 10," ORNL-TM-1872 (1967).

23. J. R. Stehn et al., "Neutron Cross Sections Z = 1 to 20," ORNL 325, Supplement No. 2.

24. R. O. Lane, S. L. Hausladen, J. E. Monahan, A. J. Elwyn, F. P. Mooring and A. Langsdorf, Jr., Phys. Rev. C4 (1971) 380.

25. M. G. Sowerby, J. Nucl. Energy A/B 20, 135 (1966).

26. M. G. Sowerby, private communication (1972).

APPENDIX

NEUTRON SCATTERING EFFECTS FOR THE GAS PROPORTIONAL COUNTERS

This page left blank intentionally.

1. INTRODUCTION

There are three significant corrections that must be made to the observed count rates from the CH_4, H_2, and BF_3 gas proportional counters due to neutrons scattered into the active volume of the counter gas. These corrections are for neutrons scattered from (1) the entrance and exit end-windows of the counter, (2) the walls of the counter (for the BF_3 counters), and (3) from sources outside the counters. While these corrections are "significant" in a measurement aimed at exceptionally high accuracy, they are all sufficiently small, due to the design of the experiment, to permit a treatment which is mostly analytical, as opposed to an elaborate (and expensive) numerical treatment with transport codes.

The following sections describe the analytical treatment of these corrections and the uncertainties they introduce in the final results. For all three scattering sources, these corrections are formulated in terms of an "effective transmission" of the counter's entrance window. Such a formulation is desirable simply on the grounds of convenience in our procedures for processing the data.

This page left blank intentionally.

2. END-WINDOW SCATTERING

The transmission of the entrance window of each gas proportional counter was corrected for anisotropic scattering of neutrons into the active volume from the entrance and exit ends of the counter. Without this correction, the count rate is

$$\frac{dC}{dt} = \varepsilon S \frac{d\phi}{dt} T_1 P_g \quad ,$$

where $d\phi/dt$ is the incident flux (neutrons/cm^2-sec), S the area of the beam incident on the counter, and ε is an electronic detection efficiency. The transmission of the entrance window (labeled "1") is T_1, and P_g is the probability of producing an observable event in the counter gas. When end-window scattering is present, the count rate becomes

$$\frac{dC'}{dt} \equiv \varepsilon S \frac{d\phi}{dt} T_1' P_g = \frac{dC}{dt} + \varepsilon S \frac{d\phi}{dt} (1 - T_1) \frac{\sigma_S^{(1)}}{\sigma_T^{(1)}} P_1$$

$$+ \varepsilon S \frac{d\phi}{dt} T_1 T_g (1 - T_2) \frac{\sigma_S^{(2)}}{\sigma_T^{(2)}} P_2 \quad ,$$

where T_g is the transmission of the gas, T_2 the transmission of the exit window (labeled "2"), and P_1 and P_2 are the gas-interaction probabilities of neutrons scattered from the entrance and exit windows, respectively.

Neglecting multiple scattering in the gas, which amounts to a very small correction to $(T_1' - T_1)$, and the relatively small nonelastic cross sections of the window components for $E_n \leqslant 1$ MeV, the effective transmission T_1' can therefore be calculated very accurately from

$$T_1' = T_1(1 + \eta_1 + \eta_2) \quad ,$$

where η_1 accounts for neutrons scattered from the entrance window,

$$\eta_1 = \frac{\bar{r}_1}{L} \frac{(1-T_1)}{T_1} Y(\bar{r}_1) \quad ,$$

and η_2 accounts for neutrons from the exit window,

$$\eta_2 = \frac{\bar{r}_2}{L} T_g(1-T_2)Y(\bar{r}_2) \quad .$$

Here, L is the active length of the counter, $\bar{r}_1$ and $\bar{r}_2$ are the average path lengths in the counter of neutrons from the entrance (1) and exit (2) windows, and Y is given by

$$Y(x) = \frac{L}{x} \frac{1 - \exp(-x\Sigma_g)}{1 - T_g} \quad ,$$

where Σ_g is the macroscopic total cross section of the gas mixture. The exit windows of the proportional counters are actually composed of two regions having illuminated areas S_A and S_B and transmissions T_2^A and T_2^B, so that

$$(1-T_2) = \frac{S_A}{S} (1-T_2^A) + \frac{S_B}{S} (1-T_2^B) \quad .$$

The average path length $\bar{r}_k$ (k = 1 or 2) is determined from the normalized scattering probability $p_k(\Omega)$,

$$\bar{r}_k = \int_{4\pi} r_k(\Omega) p_k(\Omega) d\Omega \quad ,$$

where $r_k(\Omega)$ is the distance from the scattering source on the end window to the wall of the counter. For multielement windows, the scattering probability

is averaged over the individual probabilities p_i for each element,

$$p_k(\Omega) = \frac{\Sigma_i n_i \sigma_i p_i(\Omega)}{\Sigma_i n_i \sigma_i} \quad ,$$

where n_i and σ_i are the thickness and total cross section of element i.

For our counter geometries of length L and radius a, with L >> a, the average path length $\bar{r}_k$ for an isotropic scattering source located at the counter's axis is $\pi a/4$. When the source is located at the rim of the end window, i.e., at the wall of the counter, it is shown in the following section that $\bar{r}_k = a/2$. We thus proceed to the case of anisotropic scattering assuming a source on the counter's axis, but applying a correction factor to $\bar{r}_k$ of

$$c \simeq \frac{1}{\pi a^2} \int_0^a 2\pi r \left[\frac{\pi a}{4} - \frac{r}{a}\left(\frac{\pi a}{4} - \frac{a}{2}\right)\right] dr \Big/ \frac{\pi a}{4} \quad .$$

Expressing the scattering probabilities in terms of the first four laboratory Legendre coefficients for elastic scattering, $f_\ell^i(E_n)$, with $f_0^i \equiv 1$, i.e.,

$$p_i = \sum_{\ell=0}^{3} \frac{2\ell + 1}{2} f_\ell^i P_\ell(\mu) \quad ,$$

we have

$$\bar{r}_k = c \frac{\Sigma n_i \sigma_i \bar{r}_k^i}{\Sigma n_i \sigma_i} \quad ,$$

where, for each window element i,

$$\bar{r}_1^{\,i} = \frac{1}{2}\int_0^1 r_1(\mu)d\mu + \int_0^1 r_1(\mu)\sum_1^3 \frac{2\ell+1}{2} f_\ell^i P_\ell(\mu)d\mu$$

$$\bar{r}_2^{\,i} = \frac{1}{2}\int_{-1}^0 r_2(\mu)d\mu + \int_{-1}^0 r_2(\mu)\sum_1^3 \frac{2\ell+1}{2} f_\ell^i P_\ell(\mu)d\mu \quad .$$

For a cylinder of length L and radius a, one then finds

$$\bar{r}_1^{\,i} = r_0 + \tilde{r}_1^{\,i}$$

$$\bar{r}_2^{\,i} = r_0 + \tilde{r}_2^{\,i} \quad ,$$

with

$$r_0 = \frac{a}{2}\sin^{-1}\xi - \frac{L}{2}\ell n\xi \quad ,$$

$$\tilde{r}_1^{\,i} = a\sum_1^3 \frac{2\ell+1}{2} f_\ell^i I_1^\ell(\xi) + L\sum_1^3 \frac{2\ell+1}{2} f_\ell^i I_2^\ell(\xi) \quad ,$$

$$\tilde{r}_2^{\,i} = a\sum_1^3 (-)^\ell \frac{2\ell+1}{2} f_\ell^i I_1^\ell(\xi) + L\sum_1^3 (-)^\ell \frac{2\ell+1}{2} f_\ell^i I_2^\ell(\xi) \quad ,$$

where

$$\xi = \frac{L}{\sqrt{a^2 + L^2}}$$

and the I-functions are readily found from

$$I_1^{\ell}(\xi) = \int_0^{\xi} \frac{1}{\sqrt{1 - \mu^2}} P_{\ell}(\mu) d\mu$$

$$I_2^{\ell}(\xi) = \int_{\xi}^{1} \frac{1}{\mu} P_{\ell}(\mu) d\mu \quad .$$

This page left blank intentionally.

3. WALL SCATTERING

An additional correction was applied to the count rate from the uncollimated BF_3 counters due to neutrons scattered from the counter walls (composed mainly of Fe). Without resorting to three-dimensional Monte Carlo calculations, an estimate of this correction was obtained by considering only incident-neutron trajectories in a plane containing the axis of the counter and by assuming an isotropic Fe scattering cross section below 1 MeV.

Using the same notation and approximations discussed above for the end-window-scattering corrections η_1 and η_2, the effective transmission of each BF_3 counter is

$$T_1' = (1 + \eta_1 + \eta_2 + \zeta_1 + \zeta_2)T_1 \quad ,$$

where ζ_1 accounts for the partial shielding of the incident beam when the counter is misaligned by a small angle θ from the beam direction ($\zeta_1 < 0$) and ζ_2 accounts for the neutrons scattered from the walls of the counter into its active volume. To a reasonable approximation, and for $t/\sin\theta < L$, these quantities for a counter of length L, radius $\underline{a}$ and wall thickness t are found to be

$$\zeta_1 \simeq \frac{t}{a}\frac{\tilde{T}}{T_1} - \frac{L\sin\theta}{\pi a}\left[2 - Y\left(\frac{L}{2}\right)\right] + \frac{(L\sin\theta - t)^2}{\pi a L \sin\theta}\frac{T}{T_1}Y\left(\frac{L\sin\theta - t}{2\sin\theta}\right)$$

$$\zeta_2 \simeq \frac{1}{\pi a T_1}\frac{\bar{r}_w}{L}Y(\bar{r}_w)\left[2\pi t(1 - \tilde{T}) + (4L\sin\theta - 4t)(1 - T) + 4t(1 - \tilde{T})\right] \quad ,$$

where, for an iron macroscopic total cross section Σ,

$$T = \exp(-\Sigma t/\sin\theta)$$

$$\bar{T} = \frac{2\sin^2\theta}{\Sigma^2(t^2 + 2at)}\left[\frac{\Sigma(a+t)}{\sin\theta} - 1 - e^{-\Sigma t/\sin\theta}\left(\frac{\Sigma a}{\sin\theta} - 1\right)\right] \quad .$$

Here, T_1 and Y are the same quantities defined previously, and $\bar{r}_w$ is the average path length in the counter of neutrons scattered from the wall (which will be shown to be insensitive to the location of the scattering event).

For $\bar{r}_w$ we consider a closed right circular cylinder of length x and radius a and compute the average

$$\bar{\rho}(a,x) = \frac{1}{4\pi}\int_0^{2\pi} d\phi \int_0^{\pi} d\theta \sin\theta \rho(\theta,\phi,a,x) \quad ,$$

where ρ is the distance at a direction (θ,ϕ) from a point just inside the cylinder at its corner (i.e., on an end face at a distance a from the axis) to the surface of the cylinder. It is tedious but straightforward to show

$$\bar{\rho}(a,x) = \frac{a}{2}\left[1 - \frac{1 + \frac{x}{a}\left(\frac{x}{2a} - \sqrt{1 + \left(\frac{x}{2a}\right)^2}\right)}{\sqrt{1 + \left(\frac{x}{2a}\right)^2} - \frac{x}{2a}}\right]$$

$$+ \frac{x}{4}\ln\left[\frac{\sqrt{x^2(x^2 + 4a^2)} + x^2}{2x^2}\right] \quad ,$$

which attains the limit $\bar{\rho} = a/2$ for $x >> a$. For a scattering source on the wall of a counter of length L at a distance ℓ from one end, we have

$$\bar{r}_w(\ell,a,L) = \bar{\rho}(a,\ell) + \bar{\rho}(a,L-\ell) \quad .$$

For our counter geometries, $\bar{r}_w$ varies less than 10% for $0.05L \lesssim \ell \lesssim 0.95L$; and it is therefore entirely adequate to assume a constant value of $\bar{r}_w$ in the evaluation of ζ_2.

This page left blank intentionally.

4. SCATTERING FROM OTHER SOURCES

The principal source of scattering from materials outside the proportional counters is the air surrounding the counters. The data from the CH_4, H_2, and BF_3 counters were corrected for air scattering using a final effective transmission of

$$T_1'' = T_1' + \psi T_1 \quad ,$$

where T_1' is the effective transmission discussed in Sections 2 and 3 and ψ is given approximately by

$$\psi \simeq \frac{T_w}{T_1} \frac{\bar{r}_w}{L} Y(\bar{r}_w) \frac{2\pi aL}{\pi a^2} \frac{\phi_c}{\phi_u} \quad ,$$

where T_w is the transmission of the counter walls and (ϕ_c/ϕ_u) is the ratio of the collided and uncollided scalar fluxes in the vicinity of the counter.

The ratio (ϕ_c/ϕ_u) was calculated with the two-dimensional DOT code using ENDF/B cross sections for N and O. Trial calculations for incident energies near 1 keV, 450 keV (at ^{14}N and ^{16}O resonances) and 900 keV showed that the ratio was closely proportional to the number of air collisions through two counter lengths,

$$\phi_c/\phi_u \simeq \text{constant} \cdot \left[1 - T_{air}(2L)\right] \quad .$$

This constant could then be used at all energies to estimate the correction ψ.

Additional corrections for the BF_3 counters due to scattering from support structures and from one counter to another can be estimated from the results of Sections 3 and 4 and were found to be completely negligible.

This page left blank intentionally.

5. ENERGY-AVERAGED CORRECTIONS

Before correcting for scattering effects, the count rates from the proportional counters are processed with an energy-averaged end-window transmission $\langle T_1 \rangle$ given by

$$\langle T_1 \rangle = \int_{E_n-4W}^{E_n+4W} dE' T_1(E') r(E_n,E') \quad ,$$

$$r(E_n,E') = \frac{1}{W\sqrt{\pi}} \exp\left[-(E_n-E')^2/W^2\right] \quad ,$$

$$W = 2E_n\left[2\left(\frac{\delta L_f}{L_f}\right)^2 + \frac{E_n}{3mL_f^2}\left(t_b^2 + t_c^2 + 12t_j^2\right)\right]^{\frac{1}{2}} \quad .$$

Here, E_n is the incident neutron energy, m the neutron mass, L_f the flight-path length, δL_f the effective flight-path length uncertainty, t_b the Linac burst width, t_c the channel width of the pulse-height analyzer, and t_j is the jitter time of the counter (expressed as a standard deviation). The correction to be applied to $\langle T_1 \rangle$ for scattering effects is then $\langle T_1" \rangle / \langle T_1 \rangle$, where

$$\langle T_1" \rangle = \int_{E_n-4W}^{E_n+4W} dE' T_1"(E') r(E_n,E') \quad .$$

This page left blank intentionally.

6. UNCERTAINTIES IN THE TRANSMISSION CORRECTIONS

Using the notation of the previous four sections, the overall uncertainty in the effective transmission T_1'' for the CH_4 and H_2 counters is

$$\left(\frac{\Delta T_1''}{T_1''}\right)^2 = \left(\frac{\Delta T_1}{T_1}\right)^2 + \left(\frac{\Delta\eta}{1+\eta+\psi}\right)^2 + \left(\frac{\Delta\psi}{1+\eta+\psi}\right)^2$$

$$\simeq \left(\frac{\Delta T_1}{T_1}\right)^2 + \Delta\eta^2 + \Delta\psi^2 \quad ,$$

where $\eta \equiv \eta_1 + \eta_2$. The uncertainty in the entrance-window transmission has two components,

$$\left(\frac{\Delta T_1}{T_1}\right)^2 = A^2 + B^2 \quad ,$$

where A is the component due to uncertainties in the total cross sections σ_1 and σ_2 of the two window elements (Aℓ and O),

$$A = \sqrt{n_1^2 \Delta\sigma_1^2 + n_2^2 \Delta\sigma_2^2} \quad ,$$

and B is the component due to an uncertainty in the thickness t_1 of the window,

$$B = (n_1\sigma_1 + n_2\sigma_2)\,\frac{\Delta t_1}{t_1} \quad .$$

The total uncertainty in the energy-averaged transmission for the CH_4 and H_2 counters is then given by

$$\left(\frac{\Delta\langle T_1''\rangle}{\langle T_1''\rangle}\right)^2 \simeq \langle Z\rangle^2 + C^2 \quad ,$$

with

$$\langle Z\rangle^2 = \int_{E_n-4W}^{E_n+4W} dE' Z^2(E') r^2(E_n, E', W)$$

and

$$Z^2 = A^2 + B^2 + \Delta\eta^2 + \Delta\psi^2 \quad .$$

Component C is the uncertainty in the energy-averaged transmission $\langle T_1\rangle$ due to timing uncertainties,

$$C = \frac{\Delta'\langle T_1''\rangle}{\langle T_1''\rangle} \quad ,$$

$$\Delta'\langle T_1''\rangle = \left|\frac{\partial\langle T_1''\rangle}{\partial W}\right| \Delta W \quad ,$$

$$\Delta W^2 = \left(\frac{\partial W}{\partial(\delta L_f)}\right)^2 \Delta(\delta L_f)^2 + \left(\frac{\partial W}{\partial t_b}\right)^2 \Delta t_b{}^2 + \left(\frac{\partial W}{\partial t_j}\right)^2 \Delta t_j{}^2 \quad ,$$

$$\langle T_1''(E_n)\rangle = \int_{E_n-4W}^{E_n+4W} dE' T_1''(E') r(E_n, E', W) \quad .$$

One finds

$$\left|\frac{\partial \langle T_1'' \rangle}{\partial W}\right| = \left|\frac{2}{W^3}\int_{E_n-4W}^{E_n+4W} dE' T_1''(E')(E_n-E')^2 r(E_n,E',W)\right.$$

$$\left. - \frac{\langle T_1'' \rangle}{W} + \frac{4e^{-16}}{W\sqrt{\pi}}\left[T_1''(E_n+4W) + T_1''(E_n-4W)\right]\right|$$

$$\simeq \left|\frac{2}{W^3}\int_{E_n-4W}^{E_n+4W} dE' T_1''(E')(E_n-E')^2 r(E_n,E',W) - \frac{\langle T_1'' \rangle}{W}\right|$$

and

$$\Delta W = \left\{\left(\frac{8\delta L_f E_n^2}{L_f^2 W}\right)^2 \Delta(\delta L_f)^2 + \left(\frac{4t_b E_n^3}{3mL_f^2 W}\right)^2 \Delta t_b^2 + \left(\frac{48t_j E_n^3}{3mL_f^2 W}\right)^2 \Delta t_j^2\right\}^{\frac{1}{2}} .$$

The overall uncertainty ($\Delta\langle T_1'' \rangle / \langle T_1'' \rangle$) is the fractional uncertainty in the count rates from the CH_4 or H_2 counter due to neutron scattering effects, and it is therefore the fractional uncertainty due to these effects in the flux measured with each of these counters. The $^{10}B(n,\alpha)$ cross section measured with the BF_3 counters is determined from the ratio of the count rates from the BF_3 and the flux counters. Since all the proportional counters have the same geometry and window composition, the overall uncertainty in this cross section due to scattering effects is

$$\left(\frac{\Delta\sigma(n,\alpha)_{BF_3}}{\sigma(n,\alpha)_{BF_3}}\right)^2 = \langle D \rangle^2 + C_{BF_3}^2 + C_\phi^2 \quad ,$$

where C_{BF_3} is timing-uncertainty component for the BF_3 counter, C_ϕ is the timing component for the flux counter (CH_4 or H_2), and

$$\langle D \rangle^2 = \int_{E_n-4W}^{E_n+4W} dE' D^2(E') r^2(E_n, E', W) \quad ,$$

$$D^2 \simeq \Delta \zeta^2 + 2B^2 \quad ,$$

$$\zeta \equiv \zeta_1 + \zeta_2 \quad .$$

7. RESULTS FOR THE SCATTERING CORRECTIONS AND THEIR UNCERTAINTIES

A computer program was written to calculate the individual corrections described in Sections 2 through 4 above, the final energy averaged correction $\langle T_1'' \rangle / \langle T_1 \rangle$ given in Section 5, and the various uncertainties described in Section 6 for the CH_4, H_2, and BF_3 counters using an incident-neutron energy mesh sufficiently fine to reflect the resonance structure of the cross sections involved. The cross sections for the gas, window, and wall materials and the elastic Legendre coefficients for the window elements were prepared from ENDF data (except for the F total cross section, which was obtained from BNL 325). The entrance windows for all the counters are composed of Aℓ (9.52×10^{-3} nuclei/barn) and O (1.428 nuclei/barn); and the exit window consists of two regions of Fe having thicknesses of 1.728×10^{-2} nuclei/barn and 2.964×10^{-1} nuclei/barn. The geometries of the counters and their gas densities are given in Section 4 of the text. Determination of the alignment angles θ for the BF_3 counters is described in Section 2 of the text, and determination of the timing parameters is disucssed in Section 4.

The overall uncertainties were calculated using the estimates $\Delta\eta = 0.1\eta$, $\Delta\zeta = 0.3|\zeta|$, and $\Delta\psi = 0.3\psi$. Uncertainties in the ENDF/B-III total cross sections for oxygen were taken(*) to be 4% from 1 keV to 0.5 MeV, to decrease linearly between 0.5 and 0.7 MeV, and to be 1% from 0.7 MeV to 1.0 MeV. For Aℓ the cross-section uncertainties were taken(*) to be 5% below 0.1 MeV, to decrease linearly between 0.1 MeV and 0.5 MeV, and to be 1.5% at and above 0.5 MeV. The uncertainty in the thickness of the entrance windows was estimated to be 10%. Uncertainties (Δt_j) in the jitter widths were estimated to be about 25%, and the burst width uncertainty (Δt_b) was 5 to 10 nsec. The error ($\Delta\delta L_f$) in the effective flight-path length uncertainty was 0.2 cm.

---

* P. G. Young, private communication (1972).

7.1 METHANE COUNTER

The total energy averaged correction $\langle T_1'' \rangle / \langle T_1 \rangle$ for the CH_4 counter is nearly constant except at the most prominent resonances of the counter materials and is approximately 1.02 below 50 keV and 1.01 from 50 keV to above 1 MeV. In other words, except for small energy intervals at the resonances, the total correction to the relative flux shape measured with the CH_4 counter is less than 1%. Maximum increases in the correction are about 0.5% near the $^{56}Fe+n$ resonance at 27.9 keV, 1% at the 35-keV $^{27}Al+n$ resonance, and 2% at the $^{16}O+n$ resonance near 450 keV.

The overall uncertainty $\Delta\langle T_1'' \rangle / \langle T_1 \rangle$ in the flux measured with the CH_4 counter is <1% except at the prominent resonances. Approximate values for $\Delta\langle T_1'' \rangle / \langle T_1 \rangle$ are 0.80% from 5 keV to 150 keV, 0.75% from 150 keV to 225 keV, and 0.70% from 225 keV to 300 keV. Increases in $\Delta\langle T_1'' \rangle / \langle T_1 \rangle$ are due almost entirely to the uncertainty in the end-window thickness and, to a lesser degree, the uncertainties in the total cross sections for the end-window materials; and the largest values occur at the oxygen and aluminum resonances where $\langle T_1 \rangle$ is smallest. Maximum values of $\Delta\langle T_1'' \rangle / \langle T_1 \rangle$ are about 4% at the 35-keV Aℓ resonance, 3% at the Aℓ resonances near 90 keV, 2% at the Aℓ resonances near 150 keV, and 3% near the O resonance at 442 keV. The timing resolution is such that $\Delta\langle T_1'' \rangle / \langle T_1 \rangle$ remains above 2% from 420 to 460 keV. Above the 442-keV oxygen resonance, maximum uncertainties of about 1% occur up to 1 MeV.

7.2 HYDROGEN COUNTER

Except at the resonances, the total energy averaged correction $\langle T_1'' \rangle / \langle T_1 \rangle$ for the H_2 counter is approximately 1.02 from 0.5 keV to 15 keV and 1.01 above 15 keV. Maximum increases in the correction are about 2% at 5.9 keV and 1% at 27.9 keV.

The overall uncertainty $\Delta\langle T_1'' \rangle / \langle T_1 \rangle$ in the flux measured with the H_2 counter is <1% except at the 5.9-keV Aℓ resonance, and approximate values are 0.85% from 0.5 keV to 2 keV, 0.80% from 2 keV to 15 keV, and $\leq$0.75% above 15 keV. An uncertainty of 5.6% occurs at the 5.9-keV resonance but

applies to only one channel (one energy point) of the flux data obtained with the H_2 counter.

7.3 BORON-TRIFLUORIDE COUNTERS

Except at the strongest resonances, the total correction $\langle T_1'' \rangle / \langle T_1 \rangle$ for the BF_3 counters is 0.990 ± 0.005 throughout the entire energy region 1 keV to 1 MeV. The total scattering correction to the relative $^{10}B(n,\alpha)$ cross section deduced from data obtained with the BF_3 counters is thus $\leq 0.5\%$ except at the resonances. Maximum values of the correction $\langle T_1'' \rangle / \langle T_1 \rangle$ are 1.017 at 5.9 keV, 0.9984 at 35 keV, and 0.9971 near 450 keV.

The overall uncertainty $\Delta\sigma(n,\alpha)_{BF_3}/\sigma(n,\alpha)_{BF_3}$ discussed in Section 6 is about 1% at all energies except near the resonances and is due principally to comparable contributions from the end-window thickness uncertainty (B) and the wall-scattering uncertainty (ζ). The largest uncertainties occur at the resonances of the entrance-window elements, and they extend over larger energy intervals at higher energies due to the poorer timing of the BF_3 counters. A 10% uncertainty occurs at 5.9 keV, and the uncertainty is >1% between 5.7 and 6.3 keV. This uncertainty is due to comparable contributions from the thickness uncertainty B and the BF_3 timing uncertainty (C_{BF_3}). A 5% uncertainty occurs at 35 keV, and the uncertainty is >2% between 32 and 38 keV. This uncertainty is due mainly to B and, to a lesser extend, C_{BF_3} and C_φ (the timing uncertainty for the flux data, using the H_2 counter below 20 keV and the CH_4 counter above 20 keV). An uncertainty of 3% due to the same sources occurs at 89 keV and is >2% between 85 and 94 keV. An uncertainty of ∿2% occurs between 130 and 180 keV and is due primarily to B and C_φ. An uncertainty of 3% occurs near 440 keV and is $\gtrsim$2% between 400 and 500 keV. This uncertainty is due primarily to B and C_{BF_3}.